

# Novel structured transition metal dichalcogenide nanosheets

Zhang, Xiao; Lai, Zhuangchai; Ma, Qinglang; Zhang, Hua

2018

Zhang, X., Lai, Z., Ma, Q., & Zhang, H. (2018). Novel structured transition metal dichalcogenide nanosheets. *Chemical Society Reviews*, 47(9), 3301-3338.  
doi:10.1039/c8cs00094h

<https://hdl.handle.net/10356/140993>

<https://doi.org/10.1039/c8cs00094h>

---

© 2018 Royal Society of Chemistry. All rights reserved. This paper was published in *Chemical Society Reviews* and is made available with permission of Royal Society of Chemistry.

Downloaded on 29 Aug 2024 23:58:11 SGT

# **Novel Structured Transition Metal Dichalcogenide Nanosheets**

By Xiao Zhang,<sup>a,†</sup> Zhuangchai Lai,<sup>a,†</sup> Qinglang Ma,<sup>a</sup> Hua Zhang<sup>a,\*</sup>

<sup>a</sup>Center for Programmable Materials, School of Materials Science and Engineering,

Nanyang Technological University, 50 Nanyang Avenue, Singapore 639798, Singapore

E-mail: [hzhang@ntu.edu.sg](mailto:hzhang@ntu.edu.sg), [hzhang166@gmail.com](mailto:hzhang166@gmail.com)

Phone: +65-6790-5175. Fax: +65-6790-9081

[†] These authors contributed equally to this work

**Abstract:** Ultrathin two-dimensional (2D) layered transition metal dichalcogenides (TMDs) have attracted considerable attention owing to their unique properties and great potential in a wide range of applications. Great efforts have been devoted to the preparation of novel-structured TMD nanosheets by engineering their intrinsic structures at the atomic scale. Until now, a lot of new structured TMD nanosheets, such as vacancy-containing TMDs, heteroatom doped-TMDs, TMD alloys, 1T'/1T phase and in-plane TMD crystal-phase heterostructures, TMD heterostructures, and Janus TMD nanosheets, have been prepared. These materials exhibit unique properties and hold great promise in various applications including electronics/optoelectronics, thermoelectrics, catalysis, energy storage and conversion, and biomedicine. This review focuses on the *most recent important discoveries* on the preparation, characterization and application of these new-structured ultrathin 2D layered TMDs.

## 1. Introduction

The layered transition metal dichalcogenides (TMDs) have attracted extensive interests due to their unique properties and promising applications.<sup>1-15</sup> Typically, the TMD materials are presented as  $\text{MX}_2$ , where M is the central transition metal atom (group IV, V, VI, VII, IX or X) and X represents the chalcogen atom (S, Se, or Te). Depending on the chemical composition and structural combination, these materials exhibit diverse properties, from semiconducting (e.g.,  $\text{MoS}_2$ ,  $\text{WS}_2$ ) to semimetallic (e.g.,  $\text{WTe}_2$ ,  $\text{TiSe}_2$ ), metallic (e.g.,  $\text{NbS}_2$ ,  $\text{VSe}_2$ ) and even superconducting (e.g.,  $\text{NbSe}_2$ ,  $\text{TaS}_2$ ).<sup>16-20</sup> Moreover, due to the weak van der Waals (vdW) interaction between layers, the layered TMD crystals can be exfoliated to single- or few-layer nanosheets, showing unusual physical and electronic properties different from their bulk counterparts.<sup>6,9,14,16-22</sup> So far, a wide range of methods have been developed to prepare ultrathin 2D TMDs, such as mechanical cleavage exfoliation,<sup>23,24</sup> chemical intercalation and exfoliation,<sup>25,26</sup> electrochemical Li-intercalation and exfoliation,<sup>21,27</sup> sonication-assisted liquid exfoliation,<sup>8,28</sup> chemical vapour deposition (CVD),<sup>29-31</sup> physical vapour deposition (PVD),<sup>32</sup> chemical vapour transportation (CVT) method,<sup>33,34</sup> and wet-chemical synthetic method.<sup>35,36</sup>

In order to extend their potential and widen their applications, enormous efforts have been made on preparation of novel structured TMD nanosheets. Initial efforts focused on creation of defects on TMD backbones by removing specific atoms. The controllable generation of defects on TMD nanosheets has enabled many fascinating optical/electronic properties, promising for optoelectronic devices.<sup>37,38</sup> Later on, generation of defects by the inclusion of heteroatoms into TMD lattices has also attracted interests. The dopant

atoms were shown to alter the properties of TMD nanosheets and their performance of specific applications.<sup>39</sup> More recently, considerable efforts have been devoted into the fabrication of TMD alloys and heterostructures. Because TMDs possess a broad range of properties, from semiconducting to superconducting, the preparation of alloyed TMDs and TMD heterostructures is able to tailor their bandgaps and the electronic properties in a wide range.<sup>15,40,41</sup> Furthermore, from the crystal phase point of view, the TMD monolayers have several possible polymorph structures, and each structure provides different optical/electronic properties.<sup>42,43</sup> For example, MoS<sub>2</sub> monolayer possesses three crystal phases, including semiconducting 2H (hexagonal), metallic 1T (trigonal) and semimetallic 1T' (monoclinic) phases.<sup>16,42,44</sup> Therefore, the localized phase transition in 2D TMD nanosheets enables a combination of different properties within a monolayer nanosheet, providing a highly promising way for tuning their functionality for electronic and optoelectronic applications.<sup>15,45,46</sup> Stimulated by the great achievement on the preparation of novel structured TMDs, plenty of novel devices have also been demonstrated using these new-structured TMD materials for energy storage, electronics, photonics, catalysis and biomedical applications.

In this Review, we highlight the *most recent* and *important progress* in this emerging and important research field of the new-structured ultrathin 2D TMD nanosheets. First, the new structures of TMD nanosheets, including the vacancy-containing TMD nanosheets, heteroatom-doped TMD nanosheets, alloyed TMD nanosheets, 1T/1T'-TMD nanosheets, TMD heterostructures, and Janus TMDs, will be introduced and discussed, with their synthetic methods and characterizations explained in detail. Then, the most recent applications of these new-structured TMD materials in electronics/optoelectronics,

thermoelectrics, catalysis, energy storage and conversion, and biomedical applications will be presented. Finally, we conclude the review paper with some personal insights in the challenges and future prospects in this rapidly emerging research field.

## 2. Novel structured TMD nanosheets

**Figure 1** provides a schematic overview of the recently emerged novel structured TMD nanosheets. In this review, four type of emerging TMD nanostructures (six subtypes) will be discussed. First, the structural backbone of  $\text{MX}_2$  can be tailored by engineering atoms at either M atomic sites, X atomic sites or both. The atomically engineered novel structures include three subtypes: creation of vacancies (subtype 1),<sup>37,38</sup> doping heteroatoms (subtype 2),<sup>39</sup> and alloying (subtype 3).<sup>40</sup> Second, depending on the coordination between the M and X atoms, most of the TMD materials crystallize in different polymorph structures (e.g., 2H, 1T, and 1T') with different properties (subtype 4).<sup>42,43,47</sup> Thus, engineering the local phase enables the combination of different phases within its isoelectronic monolayer, i.e., in-plane TMD crystal-phase heterostructures (subtype 4), tuning the properties of the 2D nanosheets.<sup>48-51</sup> Third, 2D lateral/vertical heterostructures can be achieved by growing different TMD nanosheets together (subtype 5).<sup>15,45,46</sup> Forth, other interesting structures such as Janus TMD nanosheets (subtype 6) with asymmetric structure have also been explored.<sup>52,53</sup> In this section, the aforementioned four type of emerging TMD nanostructures (six subtypes) will be discussed, with focus on their synthetic methods and characterizations.

## 2.1 Atomic engineering of TMD nanosheets

### 2.1.1 Vacancy-containing TMD nanosheets

TMDs contain a number of possible structural defects, such as chalcogen vacancies, transition metal vacancies, edges and even holes on the nanosheets. The controlled creation of the aforementioned defects in TMDs is particularly attractive in monolayer semiconducting nanosheets, in which the charge carrier transport and generation/recombination are confined to a 2D plane,<sup>37</sup> and the created vacancies on TMD nanosheets are prone to chemical functionalization.<sup>54,55</sup> Generally, the methods developed to generate vacancies in/on TMD nanosheets can be classified into two groups, i.e., *in-situ* creation of vacancies during chemical synthetic processes (e.g., CVT and CVD) and post-treatment of pristine TMD nanosheets. The *in-situ* creation method, relying on the chemical reaction of volatile precursors, is able to produce vacancies by adjusting the reaction conditions, such as the flow of metal/sulfur vapour and the amount/ratio of precursors. In 2013, Zhou and coworkers did a systematic study on the intrinsic atomic defects in the CVD-grown MoS<sub>2</sub>, such as point defects, dislocations, grain boundaries, and edges by using high-angle annular dark-field scanning transmission electron microscopy (ADF-STEM) characterization.<sup>56</sup> As shown in **Figure 2A**, six types of point defects were observed in the CVD-grown MoS<sub>2</sub> nanosheets, including single sulfur vacancy (V<sub>S</sub>), double sulfur vacancy (V<sub>S2</sub>), an antisite with a Mo occupying a V<sub>S2(MoS2)</sub>, vacancy of a missing Mo atom and a triad of its bonded S within one plane (V<sub>MoS3</sub>), vacancy of a missing Mo atom and all its six nearest S neighbors (V<sub>MoS6</sub>), and a pair of S atoms occupying a Mo position (S<sub>2Mo</sub>).<sup>56</sup> Later on, Hong and coworkers found that the dominant type of point defects in monolayer MoS<sub>2</sub> was highly related to the synthetic

methods.<sup>57</sup> Three types of monolayer MoS<sub>2</sub> obtained from mechanical exfoliation of bulk crystals, PVD and CVD were investigated by the ADF-STEM technique. It was observed that antisite defects were the dominant point defects in the PVD-grown MoS<sub>2</sub>, and S-vacancies were predominant in mechanically exfoliated MoS<sub>2</sub> and CVD-grown MoS<sub>2</sub>. These detailed characterizations gave valuable insights into the effects of synthetic conditions on the defect formation, promoting the possibility of engineering the TMD defects during the sample growth process. Recently, Tong and coworkers prepared the T-TiSe<sub>1.8</sub> (Ti-atom incorporation and Se-anion vacancy) nanosheets by mechanical exfoliation of the T-TiSe<sub>1.8</sub> single crystal prepared by CVT method.<sup>58</sup> The Se vacancies were derived by controlling the raw ratio of Ti/Se at 1:1.8, and the incorporation of Ti-atom was achieved by optimizing the reaction temperature.<sup>58</sup> Due to the Ti-atom incorporation and Se vacancies formation, the Ti-TiSe<sub>1.8</sub> nanosheets exhibited high spin polarization and local magnetic moment. Similarly, by controlling the molar ratio of reaction reagents of (NH<sub>4</sub>)<sub>6</sub>Mo<sub>7</sub>O<sub>24</sub>·4H<sub>2</sub>O and NH<sub>2</sub>CSNH<sub>2</sub>, Jaiswal and coworkers produced the vacancy-containing MoS<sub>2</sub> nanosheets through hydrothermal process.<sup>59</sup> The vacancy concentration was modulated by tuning the molar ratio of reagents during the hydrothermal process.

In contrast, the post-treatment of TMD nanosheets is more controllable and straightforward to create vacancies. Up to now, various techniques, such as ion/electron irradiation,<sup>60,61</sup> plasma treatment,<sup>62,63</sup> thermal annealing,<sup>64</sup> electrochemical etching,<sup>65</sup> α-particle bombardment,<sup>66</sup> Mn<sup>+</sup> ion bombardment,<sup>67</sup> proton beam irradiation,<sup>68</sup> ozone (O<sub>3</sub>) treatment,<sup>69</sup> and laser illumination,<sup>24</sup> have been demonstrated as effective ways for generating defects on TMD nanosheets. First-principle calculations suggest that the

threshold energy to remove chalcogen atoms from the TMD nanosheets is tens to hundreds of keV, which is achievable in the state-of-the-art electron microscopes.<sup>37, 70</sup> Therefore, the chalcogen vacancies can be created after TMD nanosheets are exposed to the electron beam. Interestingly, under the electron beam irradiation, the chalcogen vacancies are mobile, which can migrate and agglomerate into vacancy lines or nanoscale holes.<sup>60,61</sup> Recently, Wang and coworkers tracked the real-time formation process of sub-nanometer pores in monolayer MoS<sub>2</sub> by using the angstrom-sized probe in an aberration-corrected STEM at accelerating voltages of 60 kV and 80 kV.<sup>71</sup> The step-by-step creation of a sub-nanometer pore within MoS<sub>2</sub> is shown in **Figure 2B**. At first 10 s, the irradiated area showed agglomeration of S-vacancies. After 20 s drilling, the damage in the irradiated area increased and a single Mo atom was displaced from the lattice to the surface. Further irradiation (30 s) gave rise to the formation of small nanopores with diameter of ~ 0.9 nm. Moreover, the nanopore can be tuned from an ultra-small triangular hole, consisting of a vacancy produced by removing a single Mo atom and its coordinated six S atoms, to large hole (several nanometers in diameter) by adjusting the scanning rate.<sup>71</sup> Similarly, by using the focused electron beam, different pore sizes (e.g., pore size from 2-25 nm,<sup>60</sup> and 1-10 nm<sup>72</sup>) in TMD nanosheets were created by several groups. Moreover, three types of pore edges, i.e., Mo only, S only, and mixed Mo and S, were observed, providing flexibility in designing the nanopores with desired functionalities.<sup>73</sup>

Similar with the electron beam irradiation, plasma treatment is another effective way to remove specific atoms and generate defects in TMD nanosheets. A lot of plasma gases, including O<sub>2</sub>,<sup>74</sup> Ar,<sup>52,63</sup> CF<sub>4</sub>,<sup>75,76</sup> CHF<sub>3</sub>,<sup>76</sup> etc. have been employed to etch the surface atoms of TMD nanosheets. For example, Li and coworkers reported the oxygen plasma

etching method to fabricate atomic-scale pores in the basal plane of TaS<sub>2</sub> nanosheets.<sup>74</sup>

The TaS<sub>2</sub> nanosheets were first synthesized by a liquid exfoliation method. After the oxygen plasma treatment, the surface of TaS<sub>2</sub> nanosheets became very rough and showed a lot of ultra-small holes in ADF-STEM image. The density and morphology of the pores were well controlled by tuning the plasma treatment conditions including exposure time and exposure intensity. Nevertheless, the O<sub>2</sub> plasma treatment unavoidably induces the O-doping into the nanosheets during the treatment. As comparison, the Ar plasma treatment is more “clean” for creating defects on TMD nanosheets. For example, Li and coworkers created S-vacancies in 1H-MoS<sub>2</sub> monolayer by Ar plasma treatment, which activated the catalytically inert basal plane of 1H-MoS<sub>2</sub> for hydrogen evolution reaction (HER).<sup>63</sup> The atomically resolved ADF-STEM revealed the random distribution of S-vacancies, but no Mo sublattice was found to be damaged. Similar with the Ar plasma treatment, Lu and coworkers created S-vacancies on the basal plane of mechanical-exfoliated MoS<sub>2</sub> nanosheets using a H<sub>2</sub> plasma treatment process.<sup>52</sup> This process generated high density of S-vacancies without affecting the morphology and structure of MoS<sub>2</sub> monolayer.<sup>62</sup> Moreover, the H<sub>2</sub> plasma treatment could selectively remove the sulfur atoms in one side of MoS<sub>2</sub> nanosheets, enabling the subsequent synthesis of asymmetric Janus MoSSe nanosheets.<sup>52</sup> Note that the plasma power needs to be optimally controlled to break the surface Mo-S bonds but still preserve the underlying two-dimensional Mo-S structure. Therefore, the H<sub>2</sub> plasma is more suitable than the Ar plasma which may destroy the entire 2D structure.

In addition to the aforementioned beam/plasma treatment methods, other protocols, such as heat treatment and chemical treatment, have also been reported to produce the

vacancies on TMD nanosheets. For example, Liu and coworkers reported the controlled formation of S-vacancies and vacancy chains (with number of sulfur vacancies ranging from 2 to 4) on CVD-grown MoS<sub>2</sub>/graphene vertical heterostructures under an ultrahigh vacuum (UHV) condition by using heat treatment.<sup>64</sup> The monolayer MoS<sub>2</sub> nanosheets prepared by CVD method was nearly defect-free after annealing under UHV conditions at ~400 K, whereas single S-vacancies and vacancy chains were generated when annealed the monolayer MoS<sub>2</sub> at ~900 K. The concentration of the vacancies was controlled by varying the temperature. Importantly, these vacancies introduced an obvious *n*-doping effect and decreased the bandgap of the MoS<sub>2</sub> nanosheets. As another example, Tsai and coworkers demonstrated that the S-vacancies on MoS<sub>2</sub> nanosheets could be created by electrochemical treatment of MoS<sub>2</sub>.<sup>65</sup> During the electrochemical treatment, the S atoms in the basal plane of MoS<sub>2</sub> were reduced to hydrogen sulfide (H<sub>2</sub>S) gas via a desulfurizing ‘activation’ cycle, inducing the formation of S-vacancies on the basal plane of MoS<sub>2</sub>. The concentration of S-vacancies could be varied by changing the applied desulfurization voltage.

### 2.1.2 Heteroatom-doped TMD nanosheets

In addition to creating defects by removing atoms, heteroatom doping is another effective approach to alter the properties of TMD nanosheets, which have aroused considerable interest recently.<sup>77</sup> For heteroatom doping, the dopant atoms are incorporated into the crystal lattice of TMD nanosheets via either substitution of lattice atoms (if the dopant is well matched with the TMD nanosheets in size, valence, electronegativity and coordination) or squeezing into interstitial sites of the lattice. In principle, the doping

concentration should be lower than a certain percentage to ensure that the intrinsic crystal structure of the host materials is not altered by dopants.

The controlled synthesis of heteroatom-doped TMDs and quantification of dopant distribution are critical for understanding the doping behaviour and modulating their electronic properties. Over the last century, doping of metal atoms into MoS<sub>2</sub> and WS<sub>2</sub> films was mainly achieved by sputtering method and pulsed laser evaporation method.<sup>77</sup> In recent years, new methods have been developed, and a wide range of metal atoms, such as Re,<sup>78</sup> Au,<sup>78</sup> Co,<sup>79</sup> Mn,<sup>80, 81</sup> Nb,<sup>78</sup> Er,<sup>82</sup> Cr,<sup>83</sup> V,<sup>83</sup> and Pt,<sup>84</sup> have been successfully doped into TMD lattice. Mechanical exfoliation of heteroatom-doped TMD bulk crystals was first developed to prepare ultrathin heteroatom-doped TMD nanosheets. For example, the monolayer Nb-doped MoS<sub>2</sub> nanosheets were obtained by mechanical exfoliating the CVT-grown Nb-doped MoS<sub>2</sub> (0.5 atoms% Nb) bulk crystals.<sup>78</sup> Similarly, Lin and coworkers prepared the Re/Au-doped MoS<sub>2</sub> nanosheets (0.5~1 atoms%).<sup>85</sup> The ADF-STEM was used to distinguish the atomic number (Z) contrast of Mo and S atoms, in which the dopants, i.e., Re (Z = 75) and Au (Z = 79), showed brighter contrast than Mo (Z = 42) and S (Z = 16) atoms. Interestingly, different dopants (i.e., Re and Au) have different doping behaviours in MoS<sub>2</sub> nanosheets. The immobile Re atoms located at substitutional Mo sites, and the mobile Re atoms bonded with sulfur atoms. In contrast, the Au dopants bonding with S atoms as adatoms showed greater mobility under electron beam irradiation.

Compared with those prepared by the exfoliation process, the heteroatom-doped TMDs nanosheets prepared by CVD method usually have well-defined size and thickness, which are particularly important for investigating the doping effect towards their

optical/electronic properties. Generally, the heteroatom doped-TMD nanosheets are prepared by co-evaporating dopant sources with TMD sources in a CVD furnace. Since the doping concentration is normally low and impurities may also dope into TMDs during the CVD process, the purity of source materials is important. Robertson and coworkers demonstrated that trace amount of impurities (Cr and V) presented in the MoO<sub>3</sub> precursor could dope into MoS<sub>2</sub> nanosheets by substituting the Mo sites, forming Cr/V-doped MoS<sub>2</sub> nanosheets.<sup>83</sup> Later on, some organic metal complexes were developed as precursors for synthesis of doped-TMD nanosheets. Lewis and coworkers prepared Cr-doped MoS<sub>2</sub> nanosheets through aerosol-assisted chemical vapor deposition (AACVD) method by using a single metal-organic complex precursor, i.e., diethyldithiocarbamate complexes of Mo and Cr. The precursor was synthesized by mixing tetrakis(diethyldithiocarbamato)-molybdenum(IV) and tris(diethyldithiocarbamato)-chromium(III) in tetrahydrofuran solution.<sup>86</sup> The 5-10 mol % Cr doping dramatically increased the elastic modulus of MoS<sub>2</sub>. In addition to the source materials, the growth substrate could also affect the doping process.<sup>81</sup> The growth of Mn-doped MoS<sub>2</sub> nanosheet was investigated on various substrates. It was found that the inert substrates, such as graphene, could induce the incorporation of Mn atoms into MoS<sub>2</sub>, but the traditional substrates with reactive surface terminations (e.g., SiO<sub>2</sub> and Sapphire) could disrupt the Mn doping and introduce defects into MoS<sub>2</sub> nanosheets. Even using graphene substrate, the Mn doping concentration should be lower than 2 atom%. Otherwise, the high doping concentration (above 2 atom%) led to the destruction of the 2D structure of MoS<sub>2</sub> and the formation of MoS<sub>2</sub>-MnS coordination.

Heteroatom-doped TMD nanosheets can also be prepared in large scale by wet-chemical

methods. Recently, Liu and coworkers prepared the Co-doped single-layer MoS<sub>2</sub> nanosheets (denoted as Co-MoS<sub>2</sub>) by hydrothermal treatment of chemically exfoliated MoS<sub>2</sub> nanosheets with complex Co ion, i.e., Co(thiourea)<sub>4</sub><sup>2+</sup> which was obtained from the reaction of cobalt acetate tetrahydrate and thiourea.<sup>79</sup> The extended X-ray absorption fine structure (EXAFS) indicated that the Co existed as isolated Co atoms without formation of Co clusters or metallic particles (**Figure 3A**). The ADF-STEM image of Co-MoS<sub>2</sub> monolayers showed two bright contrast spots comparing with the surrounding Mo and S<sub>2</sub> sites (**Figure 3B**), indicating the presence of Co. Moreover, the EXAFS and density functional theory (DFT) calculation indicated that the Co atoms were located on the top of Mo site of MoS<sub>2</sub> monolayer (**Figure 3C, D**). The line-scans from both HAADF intensity (**Figure 3E**) and electron energy loss spectroscopy (EELS) (**Figure 3F**) further demonstrated that Co with the signature L<sub>3,2</sub> edge situated on atop site of Mo (**Figure 3G, H**). Similarly, Tan and coworkers reported the synthesis of Mn-doped MoS<sub>2</sub> nanosheets through a supercritical hydrothermal reaction in water phase (NH<sub>4</sub>)<sub>6</sub>Mo<sub>7</sub>O<sub>24</sub>·4H<sub>2</sub>O, Mn(CH<sub>3</sub>COO)<sub>2</sub>·4H<sub>2</sub>O, oil phase (CS<sub>2</sub>) and gas phase (Ar) at 400 °C.<sup>80</sup> The ADF-STEM and X-ray absorption fine structure (XAFS) characterizations indicated that the Mn atoms were incorporated into the MoS<sub>2</sub> nanosheets by substituting the Mo sites, and no Mn cluster or nanoparticle was formed. In the ADF-STEM image, the Mn atoms (Z = 25) were randomly distributed into MoS<sub>2</sub> nanosheets by substituting the Mo atoms (Z = 42). Interestingly, the Mn-doped MoS<sub>2</sub> nanosheets showed intrinsic ferromagnetic response with a saturation magnetic moment of 0.05 μ<sub>B</sub> Mn<sup>-1</sup> at room temperature. Apart from aforementioned examples, a series of few-layer metal-doped WS<sub>2</sub> nanosheets, including Fe-, Co-, Ni-, Mn-, and Gd-doped WS<sub>2</sub>, have also been prepared by the colloidal

synthesis method.<sup>87</sup>

### 2.1.3 Alloyed TMD nanosheets

Alloyed TMD nanosheets, also known as solid solutions of TMD nanosheets, have drawn considerable attention for tuning the physicochemical properties of TMD nanomaterials. In alloyed TMD nanosheets, one of the elements in TMDs is partially substituted by another element, with the crystal structures of nanosheets remaining homogeneous. Compared with that in heteroatom doping, the amount of substitution in alloyed TMDs can be at arbitrary percentages. In principle, the metal atoms for formation of isoelectronic 2D TMD alloys should simultaneously follow three rules: (1)  $|a_1-a_2|/\max(a_1,a_2) < 0.034$ , (2)  $\Delta d_{M-X} < 0.1 \text{ \AA}$ , and (3)  $(Eg_1 > 0) \vee (Eg_2 > 0)$ , where  $a_1$  and  $a_2$  are the lattice constants of the two TMD materials,  $\Delta d_{M-X}$  is the difference in the metal-chalcogen bond, and  $Eg_1$  and  $Eg_2$  are their bandgaps.<sup>12,40</sup> The rules (1) and (2) require good matching between the lattice constants and metal-chalcogen bond distances, and the rule (3) requires that at least one compound should be a semiconductor since the mixture of two metallic TMD materials is not expected to have a finite band gap. For example,  $\text{MoX}_2$  and  $\text{WX}_2$  have similar lattice/electronic structure, and the formation energy of  $\text{Mo}_{1-x}\text{W}_x\text{X}_2$  alloy is negative. Thus, the  $\text{Mo}_{1-x}\text{W}_x\text{X}_2$  alloy is energetically favorable to be formed. So far, three types of 2D TMD isoelectronic alloys, i.e.,  $\text{M}_x\text{M}'_{1-x}\text{X}_2$ ,  $\text{MX}_x\text{X}'_{2(1-x)}$ , and  $\text{M}_x\text{M}'_{1-x}\text{X}_y\text{X}'_{2(1-y)}$  have been prepared.

#### **$\text{M}_x\text{M}'_{1-x}\text{X}_2$ type**

In the  $M_xM'_{1-x}X_2$  type alloy, one of the transition metal elements in TMDs is partially substituted by another one. Since most TMDs have same structures and similar lattice parameters, it is easy to form relatively strain-free alloyed TMD alloys. The early works by the Xie group demonstrated single-layer  $Mo_xW_{1-x}S_2$  nanosheets with varying compositions mechanically exfoliated from their corresponding bulk crystals.<sup>88, 89</sup> The atomic-resolution STEM revealed the random arrangement of Mo and W atoms in the  $Mo_xW_{1-x}S_2$  monolayer alloy.<sup>88</sup> The bandgap of the as-prepared alloyed  $Mo_xW_{1-x}S_2$  nanosheets could be continuously tuned from 1.82 eV ( $x = 0.2$ ) to 1.99 eV ( $x = 1$ ) by changing the  $x$  value.<sup>88</sup> Moreover, the composition-dependent Raman modes of monolayer  $Mo_xW_{1-x}S_2$  nanosheets were demonstrated.<sup>89</sup> The disorder-related Raman peak could only be detected in the alloyed  $Mo_xW_{1-x}S_2$  nanosheets but not in the pure  $MoS_2$  or  $WS_2$  nanosheets. Similarly, the high-pressure Raman spectroscopy conducted by Kim and coworkers demonstrated that the alloyed  $Mo_{0.5}W_{0.5}S_2$  nanosheet showed several new peaks upon pressure.<sup>90</sup> A new peak at  $470\text{ cm}^{-1}$  was observed in the alloyed  $Mo_{0.5}W_{0.5}S_2$  nanosheet but not in the pure  $MoS_2$  or  $WS_2$  nanosheets. Later on, the CVD method was employed to prepare TMD alloyed nanosheets. The synthetic procedure was similar to that of growing  $MoS_2$  nanosheets, e.g., by co-vaporizing metal sources (metal, metal oxide or TMD powders) in the presence of chalcogen vapors. For example, the  $Mo_{1-x}W_xS_2$  nanosheets could be obtained through either the reaction of  $Mo_{1-x}W_x$  ( $x = 0$  to 0.19, 0.55, 0.85, and 1) and S vapor,<sup>91</sup> or the sulfuration of the mixture of  $MoO_3$  and  $WO_3$  in a CVD furnace.<sup>92</sup> Similarly, the  $Mo_xW_{1-x}Se_2$  ( $0 < x < 0.18$ ) nanosheets could be prepared by selenylation of the  $MoO_3$  and  $WO_3$  mixture at  $780\text{ }^{\circ}\text{C}$ . Compared with pure  $MoSe_2$  monolayers, the  $Mo_xW_{1-x}Se_2$  nanosheets had 50% reduced concentration of Se vacancy,

showing ~10 times more intense photoluminescence (PL) and ~3 times longer exciton lifetime.<sup>93</sup> As known, CVD method was usually operated at high vacuum and high temperature. Liu and coworkers recently reported the growth of large area  $W_xMo_{1-x}S_2$  monolayer with triangle shape using a CVD method under atmospheric pressure.<sup>94</sup> Wang and coworkers demonstrated the growth of  $Mo_{1-x}W_xS_2$  with a wide range of Mo/W ratios at relatively low temperature of 700 °C.<sup>95</sup>

All the aforementioned alloyed nanosheets have been obtained by CVD or CVT combined with exfoliation techniques. The alloyed TMD nanosheets can also be prepared by various solution-based methods. For example, our group prepared the aqueous solution-dispersed  $Mo_xW_{1-x}S_2$  and  $MoS_{2x}Se_{2(1-x)}$  nanosheets through the Li intercalation and exfoliation of CVT-grown  $Mo_xW_{1-x}S_2$  and  $MoS_{2x}Se_{2(1-x)}$  bulk crystals.<sup>96</sup> The obtained  $Mo_xW_{1-x}S_2$  nanosheets were several hundred nanometres in size (**Figure 4A-C**) and 0.9–1.2 nm in thickness, corresponding to the single layers (**Figure 4B**). The W and Mo atoms were randomly distributed in the monolayer nanosheet (**Figure 4D**). It is worth pointing out that the obtained monolayer  $Mo_xW_{1-x}S_2$  nanosheets had high-concentration metallic 1T phase, proved by the X-ray photoelectron spectroscopy (XPS) Mo 3d and W 4f spectra (**Figure 4E, F**). As another example, Yang and coworkers prepared the alloyed  $Mo_{1-x}W_xS_2$  nanosheets with tunable 1T/2H phase ratios by using hydrothermal method.<sup>97</sup> The 1T concentration in  $Mo_{1-x}W_xS_2$  alloys could be controlled by varying the reaction temperature.

### **$MX_xX'_{2(1-x)}$ type**

Besides the  $M_xM'_{1-x}X_2$  nanosheets, the  $MX_xX'_{2(1-x)}$  type nanosheets with varying  $x$  values have also been prepared by CVD method. Based on different reaction conditions, the

preparation of  $\text{MX}_x\text{X}'_{2(1-x)}$  nanosheets through CVD process can be typically classified as four processes. (1)  $\text{MoS}_{2x}\text{Se}_{2(1-x)}$  nanosheets are prepared by the reaction between  $\text{MoO}_3$  with mixed S/Se vapor. For example, the Ajayan group<sup>98</sup> and the Duan group<sup>99</sup> have prepared the alloyed  $\text{MoS}_{2x}\text{Se}_{2(1-x)}$  nanosheets with tunable compositions by sulfidation/selenylation of  $\text{MoO}_3$  in a CVD furnace. Later, Feng and coworkers further demonstrated that the shape of the obtained alloyed  $\text{MoS}_{2(1-x)}\text{Se}_{2x}$  nanosheets could be tuned by changing the growth temperature.<sup>32</sup> When the growth temperature varies at 630 °C, 670 °C and 750 °C, the alloyed  $\text{MoS}_{2x}\text{Se}_{2(1-x)}$  nanosheets showed triangles with straight edges, hexagons with straight edges, and triangles with inward-curving edges, respectively. Similar fabrication processes were also adopted to synthesize single-layer alloyed triangular  $\text{WS}_{2x}\text{Se}_{2(1-x)}$  nanosheets by reacting  $\text{WO}_3$  with S/Se vapor.<sup>100</sup> (2) TMD alloys with tunable compositions are prepared using  $\text{MoS}_2$  and  $\text{MoSe}_2$  as precursors. For example, Duan and coworkers reported the synthesis of alloyed  $\text{WS}_{2x}\text{Se}_{2(1-x)}$  nanosheets with fully tunable compositions in a home-made CVD system by using  $\text{WS}_2$  and  $\text{WSe}_2$  as precursors.<sup>101</sup> The S/Se ratios in resultant alloyed  $\text{WS}_{2x}\text{Se}_{2(1-x)}$  nanosheets could be easily tuned by controlling the heating temperature of the  $\text{WS}_2$  and  $\text{WSe}_2$  sources. (3) Selenization of CVD-grown  $\text{MoS}_2$  nanosheets is achieved by Se vapor in a CVD furnace.<sup>102</sup> (4) The alloy TMDs can also be prepared by using  $\text{MoO}_3$  as the Mo source and thiophenol/diphenyl-diselenide dissolved in tetrahydrofuran as the S/Se source.<sup>103</sup>

Similar with  $\text{M}_x\text{M}_{(1-x)}\text{X}_2$  alloys, the  $\text{MX}_x\text{X}'_{2(1-x)}$  alloyed nanosheets can also be obtained by reacting appropriate transition metal and chalcogen precursors through wet chemical reaction. For instance, Gong and coworkers reported the synthesis of few-layer  $\text{MoS}_{2(1-x)}\text{Se}_{2x}$  (with  $x = 0, 0.33, 0.5, 0.66$  and 1) nanosheets via a colloidal synthetic method by

reacting  $\text{MoCl}_5$  with S/Se powder dissolved in a mixed solvent of oleylamine and 1-octadecene at 300 °C.<sup>104</sup> Xu and coworkers demonstrated a liquid-liquid interface-mediated strategy to synthesize monolayer  $\text{MoS}_{2x}\text{Se}_{2(1-x)}$  alloy by hydrothermal treatment of  $(\text{NH}_4)_6\text{Mo}_7\text{O}_{24} \cdot 4\text{H}_2\text{O}$ , S and Se powder in the mixture of oleylamine and water.<sup>105</sup> The XAFS characterization indicated that the  $\text{MoS}_{2x}\text{Se}_{2(1-x)}$  alloy showed shorter Mo-S bonds and longer Mo-Se bonds compared with pure  $\text{MoS}_2$  and  $\text{MoSe}_2$  nanosheets. The variation in the bond lengths could tailor the *d*-band electronic structure of Mo atoms. As another example, Sun and coworkers reported the synthesis of few-layer  $\text{Mo}_x\text{W}_{1-x}\text{Se}_2$  and  $\text{WS}_{2y}\text{Se}_{2(1-y)}$  colloidal dispersion by injecting the metal reagents (i.e.,  $\text{MoCl}_5$ ,  $\text{WCl}_6$  in oleic acid) into mixture of diphenyl diselenide, oleylamine and hexamethyldisilazane.<sup>36</sup> The composition of obtained alloys was fully tunable, covering all possible solid solutions from  $\text{MoSe}_2$  to  $\text{WSe}_2$  and from  $\text{WS}_2$  to  $\text{WSe}_2$ , respectively.

In addition to the aforementioned Mo/W based alloys, other  $\text{MX}_x\text{X}'_{2(1-x)}$  type nanosheets have also been prepared. For example, Wen and coworkers demonstrated the preparation of alloyed  $\text{ReS}_{2(1-x)}\text{Se}_{2x}$  nanosheets by mechanical exfoliation of CVT-grown  $\text{ReS}_{2x}\text{Se}_{2(1-x)}$  crystals.<sup>106</sup> The as-prepared alloyed  $\text{ReS}_{2(1-x)}\text{Se}_{2x}$  nanosheets were in 1T' phase, and the nanosheets exhibited anisotropic spectroscopy, tunable bandgap and electrical properties. The photoluminescence emission energy of  $\text{ReS}_{2(1-x)}\text{Se}_{2x}$  monolayers ( $x = 0-1$ ) could be continuously tuned from 1.62 to 1.31 eV. As another example, the single-crystal  $\text{SnS}_{2-x}\text{Se}_x$  nanosheets with S/Se vacancies were exfoliated by sonication of  $\text{SnS}_{2-x}\text{Se}_x$  bulk crystals in ethanol without additive.<sup>107</sup>

### **$\text{M}_x\text{M}'_{(1-x)}\text{X}_{2y}\text{X}'_{2(1-y)}$ type**

Recently, Susarla and coworkers reported the synthesis of quaternary  $\text{Mo}_x\text{W}_{(1-x)}\text{S}_{2y}\text{Se}_{2(1-y)}$

nanosheets by evaporation of ammonium molybdate tetrahydrate (AT), ammonium metatungstate (AMT), selenium (Se) and sulfur (S) powder in a CVD furnace.<sup>108</sup> The composition of the alloys could be tuned by varying the temperature from 650 to 800 °C. The optimum temperature of growing uniform quaternary alloy was found to be 750 °C, at which the fraction of quaternary phase was maximum. Interestingly, the bandgaps of quaternary alloys could be tuned between 1.60 and 2.03 eV.

### **Composition-dependent phase transition in TMD alloys**

Most recently, it was reported that some TMD alloys exhibit composition-dependent crystal phase and properties. This phenomenon is particularly common in Te-based TMD nanosheets. For example, Yu and coworkers prepared the WSe<sub>2(1-x)</sub>Te<sub>2x</sub> ( $x = 0\text{-}1$ ) nanosheets with fully tunable compositions by mechanical exfoliation of CVT-grown WSe<sub>2(1-x)</sub>Te<sub>2x</sub> single crystals.<sup>109</sup> The ternary alloyed WSe<sub>2(1-x)</sub>Te<sub>2x</sub> compound showed pure 2H structure at  $x = 0\text{-}0.4$ , mixed 2H and 1T<sub>d</sub> (orthorhombic) structures at  $x = 0.5$  and 0.6, and pure 1T<sub>d</sub> structure at  $x = 0.7\text{-}1.0$ . The PL spectra showed that the optical band gaps of the WSe<sub>2(1-x)</sub>Te<sub>2x</sub> monolayer could be tuned from 1.67 to 1.44 eV (2H semiconductor) to 0 eV (1T<sub>d</sub> metal). Similar phenomenon was also observed in alloyed MoSe<sub>2x</sub>Te<sub>2(1-x)</sub><sup>110</sup> and Mo<sub>1-x</sub>W<sub>x</sub>Te<sub>2</sub> nanosheets.<sup>111,112</sup> Yu and coworkers prepared ternary alloyed WSe<sub>2(1-x)</sub>Te<sub>2x</sub> ( $x = 0\text{-}1$ ) crystals through one-step CVT method.<sup>109</sup> Besides Te-based compounds, the doping of 1T-TiSe<sub>2</sub> also showed composition-dependent properties. For example, Luo and coworkers reported that when Ta or Nb substituted the Ti in TiSe<sub>2</sub>, the as-doped 1T-TiSe<sub>2</sub> exhibited different properties, even though Nb and Ta were chemically equivalent electron donors.<sup>113</sup> The superconducting property emerged when Ta partially substituted Ti in 1T-TiSe<sub>2</sub>, yet no such property was observed when Nb partially substituted Ti.

**Table 1.** Summary of some representative alloyed TMD nanosheets.

Preparation method	TMD alloy	Component ratio ( $x$ )	Preparation details	Structure features	Unique properties	Reference
Exfoliation of bulk crystals	$\text{Mo}_x\text{W}_{1-x}\text{S}_2$	$x = 0\text{--}1$	Mechanical exfoliation of bulk $\text{Mo}_x\text{W}_{1-x}\text{S}_2$ crystals	Monolayer nanosheets	Continuously tunable bandgaps from 1.82 eV ( $x = 0.2$ ) to 1.99 eV ( $x = 1$ )	88
	$\text{Mo}_x\text{W}_{1-x}\text{S}_2$	$\text{Mo}_{0.65}\text{W}_{0.35}\text{S}_2$	Li-intercalation and exfoliation of CVT-grown $\text{Mo}_x\text{W}_{1-x}\text{S}_2$ and $\text{MoS}_2\text{Se}_{2(1-x)}$ crystals	Nanosheets with, several hundred nanometres in lateral size and 0.9–1.2 nm in thickness	High concentration of metallic 1T phase ( $\approx 66\%$ )	96
	$\text{ReS}_{2(1-x)}\text{Se}_{2x}$	$x = 0\text{--}1$	Mechanical exfoliation of CVT-grown $\text{ReS}_{2(1-x)}\text{Se}_{2x}$ crystals	Mono-/few-layer nanosheets	Tunable bandgaps in the range of 1.31–1.62 eV; anisotropic Raman scattering	106
	$\text{WSe}_{2(1-x)}\text{Te}_{2x}$	$x = 0\text{--}1$	Mechanical exfoliation of CVT-grown $\text{WSe}_{2(1-x)}\text{Te}_{2x}$ crystals	Monolayer nanosheets	Tunable optical bandgaps from 1.67 to 1.44 eV (2H semiconductor) and finally to 0 eV (1T <sub>d</sub> metal)	109
	$\text{SnS}_{2-x}\text{Se}_x$	$x = 0, 0.5, 1, 1.5, \text{ and } 2$	Sonication of $\text{SnS}_{2-x}\text{Se}_x$ crystals in ethanol	Nanosheets with micrometers to tens of micrometers in lateral size and $\sim 0.68\text{--}1.35$ nm in thickness	Tunable activation energy and bandgaps	107
CVD method	$\text{Mo}_{1-x}\text{W}_x\text{S}_2$	$x = 0, 0.19, 0.55, 0.85, \text{ and } 1$	Reaction of $\text{Mo}_x\text{W}_{1-x}$ with S vapor	Nanosheets with 50 nm in lateral size and 2–4 layers in thickness	Tunable direct bandgaps from 1.85 to 1.99 eV by increasing $x$ from 0 to 1	91
	$\text{Mo}_{1-x}\text{W}_x\text{S}_2$	$x = 0\text{--}1$	Sulfuration of the mixture of $\text{MoO}_3$ and $\text{WO}_3$ at 750 °C	Monolayer nanosheets	Tunable bandgaps of $\text{Mo}_{(1-x)}\text{W}_x\text{S}_2$ from 1.83 to 1.97 eV.	92
	$\text{MoS}_{2(1-y)}\text{Se}_{2y}$	$y = 0\text{--}1$	Reaction of the mixture of S and Se with $\text{MoO}_3$ at 680 °C		The bandgap of $\text{MoS}_{2(1-y)}\text{Se}_{2y}$ broadened from 1.55 to 1.97 eV	
	$\text{Mo}_x\text{W}_{1-x}\text{Se}_2$	$0 < x < 0.18$	Selenylation of the mixture of $\text{MoO}_3$ and $\text{WO}_3$ at 780 °C	Monolayer nanosheets with tens of microns in size	$\text{Mo}_{0.82}\text{W}_{0.18}\text{Se}_2$ with $\sim 10$ times stronger PL intensity and longer exciton lifetime compared to $\text{MoSe}_2$	93
	$\text{W}_x\text{Mo}_{1-x}\text{S}_2$	$x = 0.66$	Sulfidation of the mixture of $\text{MoO}_3$ and $\text{WO}_3$ at 850 °C under atmospheric pressure	Monolayer nanosheets with $\sim 20$ μm in size	Field effect mobility of $\sim 30 \text{ cm}^2 \text{ V}^{-1} \text{ s}^{-1}$ at 300 K	94
	$\text{Mo}_{1-x}\text{W}_x\text{S}_2$	$x = 0\text{--}1$	Low-pressure chemical vapor deposition: gas species ( $\text{MoO}_{3-x}$ and $\text{WCl}_6$ ) are transported and sulfurized to form $\text{Mo}_{1-x}\text{W}_x\text{S}_2$	Monolayer nanosheets	Tunable direct bandgaps by altering W proportions	95
	$\text{MoS}_{2(1-x)}\text{Se}_{2x}$	$x = 0.41\text{--}1.0$	Evaporation of $\text{MoSe}_2$ and $\text{MoS}_2$ powders with Se powder	Monolayer nanosheets with up to 20 μm in size	Continuously tunable bandgaps from 1.86 to 1.55 eV; Raman peak splitting	32
	$\text{WS}_{2(1-x)}\text{Se}_{2x}$	$x = 0.18, 0.3,$	Reaction of $\text{WO}_3$ with	Monolayer	Tunable bandgaps	100

		and 0.43	S/Se vapor	nanosheets with triangular shape	by varying the ratio of Se and S; excellent HER activity	
	$\text{WS}_{2x}\text{Se}_{2(1-x)}$	$x = 0\text{-}1$	Evaporation of $\text{WS}_2$ and $\text{WSe}_2$ at high temperature	Monolayer nanosheets	Tunable electric behaviour from highly p-type in selenium-rich alloy to highly n-type in sulfur-rich alloys	101
	$\text{MoS}_{2(1-x)}\text{Se}_{2x}$	$x = 0\text{-}1$	$\text{MoO}_3$ as the Mo source and thiophenol/di-phenyldiselenide dissolved in tetrahydrofuran as the S/Se source	Monolayer nanosheets	Tunable bandgaps in the range of 1.87 eV (pure single-layer $\text{MoS}_2$ ) to 1.55 eV (pure single-layer $\text{MoSe}_2$ )	103
	$\text{Mo}_x\text{W}_{(1-x)}\text{S}_{2y}\text{Se}_{2(1-y)}$	$x = y$	Evaporation of ammonium molybdate tetrahydrate, ammonium metatungstate, Se and S powder in a CVD furnace	Monolayer nanosheets	Tunable bandgaps between 1.60 and 2.03 eV	108
	$\text{W}_x\text{Nb}_{1-x}\text{Se}_2$	N.A.	First deposit the $\text{WO}_3$ thin film, followed by deposition of $\text{Nb}_2\text{O}_5$ using plasma-enhanced atomic layer deposition technique. Then the film was selenized to form the $\text{W}_x\text{Nb}_{1-x}\text{Se}_2$ .	Nanosheets with tuneable thickness (~4, 4.5, and 7 nm)	The presence of a $\text{W}_x\text{Nb}_{1-x}\text{Se}_2$ mixed-transition atomic layer reduces the Schottky barrier height, leading to a high ON current for the $\text{WSe}_2$ FET	114
Wet-chemical method	$\text{Mo}_{1-x}\text{W}_x\text{Se}_2$	$x = 0, 0.04, 0.08, 0.13, \text{ and } 1$	Hydrothermal reaction of $(\text{NH}_4)_{10}\text{W}_{12}\text{O}_{41} \cdot x\text{H}_2\text{O}$ , $(\text{NH}_4)_6\text{Mo}_7\text{O}_{24} \cdot 4\text{H}_2\text{O}$ , thiourea and deionized water at 200 °C	Few-layer nanosheets	Tunable 1T/2H phase ratios	97
	$\text{Mo}_x\text{W}_{1-x}\text{Se}_2$	$x = 0, 0.14, 0.35, 0.52, 0.77, \text{ and } 1$	Injecting the metal reagents (i.e., $\text{MoCl}_5$ , $\text{WCl}_6$ in oleic acid) into the mixture of diphenyl diselenide, oleylamine and hexamethyldisilazane	Mono-/few-layer nanosheets	Tunable optical properties, such as excitonic transitions ranging from 1.51 to 1.93 eV	36
	$\text{WS}_{2y}\text{Se}_{2(1-y)}$	$y = 1, 0.81, 0.70 \text{ and } 0.60$				
	$\text{MoS}_{2(1-x)}\text{Se}_{2x}$	$x = 0, 0.33, 0.5, 0.66, \text{ and } 1$	Reacting $\text{MoCl}_5$ with S/Se powder dissolved in mixed solvent of oleylamine and 1-octadecene at 300 °C	Mono-/few-layer nanosheets	High activity and durability for HER electrocatalysis	104
	$\text{MoSeS}$	N.A.	Hydrothermal treatment of $(\text{NH}_4)_6\text{Mo}_7\text{O}_{24} \cdot 4\text{H}_2\text{O}$ , S and Se powder in the mixture of oleylamine and water	Monolayer nanosheets	The highest 45.2% Faradaic efficiency for CO production	105

## 2.2 Phase-based TMD new structures

Phase-based TMD new structures are currently attracting increasing attention. Generally, two common types of crystal phases of single-layer TMDs exist, i.e., 2H and 1T (**Figure 5**).<sup>42, 115</sup> The 2H phase is in a hexagonal symmetry (D3h), in which the chalcogen atoms

are vertically aligned along the  $z$ -axis and the stacking sequence follows XMX in a single layer. The 1T phase has a tetragonal symmetry ( $D_{3d}$ ) with an octahedral coordination of the metal atoms. Compared with 2H phase, the 1T structure can be regarded as shifting one of the chalcogen layers into the XMX' stacking sequence. Furthermore, structure distortions could exist to compromise the periodicity of TMD materials, resulting in the formation of metal-metal bonds (e.g., 1T' and 1T<sub>d</sub> (orthorhombic) phase). These polymorph structures show different properties. For example, the 1T-MoS<sub>2</sub> exhibits metallic property which is  $10^7$  times more conductive than the semiconducting 2H phase.<sup>116,117</sup> Moreover, the metallic 1T-MoS<sub>2</sub> shows better performance than its semiconducting 2H counterpart in the applications of hydrogen evolution reaction (HER) and supercapacitors. Since the 2H phase has been well studied, this section mainly focuses on the newly emerging 1T/1T' phases and the in-plane TMD crystal-phase heterostructures.

### 2.2.1 Pure 1T/1T' phase

Recently, the 1T/1T'-phase TMD nanosheets are explored extensively due to their unique structures and outstanding properties. In the TMD family, some materials are naturally crystallized in 1T/1T' phase. For example, the TiS<sub>2</sub>, TiSe<sub>2</sub>, TaS<sub>2</sub>, HfS<sub>2</sub>, and WTe<sub>2</sub> have intrinsic 1T phase, and VTe<sub>2</sub> and ReS<sub>2</sub> are naturally in 1T' phase (**Figure 6A, B**). Due to the unique structure, these materials show distinct properties compared with the 2H phase TMDs. For example, the ultrathin TaS<sub>2</sub> and 1T-TiSe<sub>2</sub> nanosheets show charge density wave (CDW) and superconductivity properties,<sup>7</sup> and the 1T'-ReS<sub>2</sub> exhibit metallic property regardless of layer number.<sup>118</sup>

Direct exfoliation of bulk crystals is the most straightforward way to prepare ultra-thin 1T/1T' nanosheets. Up to now, a broad range of ultrathin 1T/1T' nanosheets, such as TaS<sub>2</sub>,<sup>119</sup> MoTe<sub>2</sub>,<sup>120, 121</sup> NbSe<sub>2</sub>,<sup>122</sup> WTe<sub>2</sub>,<sup>121</sup> TaS<sub>2</sub><sup>123</sup>, ReS<sub>2</sub><sup>124-126</sup> and NbSe<sub>2</sub>,<sup>122</sup> have been prepared by exfoliation of their corresponding bulk crystals. For example, the distorted 1T'-ReS<sub>2</sub><sup>124, 125</sup> and 1T'-MoTe<sub>2</sub><sup>120</sup> were prepared through mechanical exfoliation of their CVT-grown bulk counterpart. The semimetal 1T<sub>d</sub>-WTe<sub>2</sub> nanosheets (2-7 layers) were obtained by sonication of bulk WTe<sub>2</sub> crystals in solution.<sup>127</sup> The STEM image showed that the as-exfoliated 1T<sub>d</sub>-WTe<sub>2</sub> nanosheets had interconnected zigzag W-Te chains forming a quasi-1D structure.

Recently, CVD method was developed for synthesis of high-quality 1T/1T' TMD nanosheets.<sup>128</sup> Since some 1T/1T' TMDs have very similar ground-state energy with their 2H counterpart (e.g., the energy difference per formula unit between 2H-MoTe<sub>2</sub> and 1T'-MoTe<sub>2</sub> is ~35 meV), the CVD reaction conditions (e.g., precursors, substrate, and growth promoter agents) should be accurately controlled to prevent the formation of other phases.<sup>51,111,120,129-131</sup> In 2015, Zhou and coworkers produced high crystallinity few-layer 2H- and 1T'-MoTe<sub>2</sub> films using CVD method, and they found that the growth of 2H and 1T' phases were highly sensitive to the choice of Mo precursor (i.e., Mo or MoO<sub>3</sub>).<sup>130</sup> It was suggested that the MoO<sub>3</sub> precursor reacted more easily with Te to form 2H-MoTe<sub>2</sub>, while the Mo and MoO<sub>x</sub> ( $x < 3$ ) precursors tended to form homogeneous 1T'-MoTe<sub>2</sub> film. Later on, the same group employed the same synthetic process and obtained the high-quality few-layer 1T'-MoTe<sub>2</sub> nanosheets by controlled tellurization of MoO<sub>3</sub> film (**Figure 6C**).<sup>131</sup> The Te amount was important for the polymorph of MoTe<sub>2</sub>. The 2H-MoTe<sub>2</sub> was obtained with sufficient Te source, while 1T'-MoTe<sub>2</sub> was obtained with insufficient Te

supply. Moreover, the 1T'-MoTe<sub>2</sub> grown from MoO<sub>3</sub> had higher crystallinity and better uniformity than the 1T'-MoTe<sub>2</sub> from Mo source (**Figure 6C**). The investigation on the role of the Mo precursor and the amount of Te provided valuable insights into the controllable synthesis and phase engineering of MoTe<sub>2</sub>. In addition to the precursors, the solid substrate also affects the quality of 1T/1T' nanosheets. For example, Fu and coworkers reported the epitaxy growth of 1T-HfS<sub>2</sub> crystals on fluorophlogopite mica (KMg<sub>3</sub>AlSi<sub>3</sub>O<sub>10</sub>F<sub>2</sub>) substrate through an improved CVD method.<sup>132</sup> HfCl<sub>4</sub> and S powders were used as the precursors, and two magnets were placed both inside and outside the CVD quartz tube to reduce the nanoparticle deposition. It was found that the mica substrate with flat and inert surface favoured the vdW epitaxial growth of HfS<sub>2</sub> crystals, giving rise to a fast lateral growth of 2D HfS<sub>2</sub> crystals. Furthermore, some growth promoter agents were used to decrease the reaction energy barrier for synthesis of high-quality 1T/1T' TMD nanosheets.<sup>133</sup> For example, Zhang and coworkers prepared few-layered metastable 1T'-MoTe<sub>2</sub> flakes by introducing iodine as medium reagent.<sup>134</sup> The iodine could induce the change in the Mo-Te bond length. Moreover, the iodine could induce the formation of volatile intermediate (e.g., MoO<sub>2</sub>I<sub>2</sub>) at growth temperature, benefiting the controllable supply of Mo and Te for the subsequent nucleation of 1T'-MoTe<sub>2</sub> nanosheets. As another example, sodium cholate solution was used as growth promoter for synthesis of single-crystal 1T'-MoTe<sub>2</sub><sup>135</sup> and 1T'-WTe<sub>2</sub><sup>136</sup> nanosheets. The growth promoter and Mo/W-feedstock material were first deposited onto the growth substrate. Then the substrate was exposed to telluride at 700 °C to form the 1T'-MoTe<sub>2</sub><sup>135</sup> or 1T'-WTe<sub>2</sub><sup>136</sup> nanosheets. Also, the inorganic salts were adopted as the promoter to synthesize 1T'/1T TMDs. Recently, Chen and coworkers reported the synthesis of 1T'-

$\text{MoTe}_2$  and  $\text{WTe}_2$  by using  $\text{NaCl}/\text{KCl}$  as the growth promoter.<sup>137</sup> The obtained 1T'- $\text{MoTe}_2$  showed few-layer thickness with the length of ~1 mm, and the  $\text{WTe}_2$  had the length of ~350 um. The atomic force microscopy (AFM), XPS, Raman spectroscopy, and TEM confirm the morphology and the atomic structure of the as-grown 1T'- $\text{MoTe}_2$  and  $\text{WTe}_2$  flakes.

Besides the CVD process, the pure 1T/1T' phase TMD nanosheets could also be prepared through the wet-chemical method. For example, Sun and coworkers reported the preparation of 1T'- $\text{MoTe}_2$  by injecting an oleic acid solution of  $\text{MoCl}_5$  into a mixture of trioctylphosphine, trioctylphosphine telluride, oleylamine, and hexamethyldisilazane at 300 °C.<sup>138</sup> The as-prepared 1T'- $\text{MoTe}_2$  showed flower-like nanostructures comprising of few-layer nanosheets. Compared with the bulk crystal counterpart, the obtained 1T'- $\text{MoTe}_2$  showed polycrystalline nature and exhibited ~1% lattice compression. Importantly, the wet-chemical methods are also promising for synthesis of pure 1T/1T'-TMDs whose thermodynamically stable polymorph is 2H phase (e.g.,  $\text{MoS}_2$ ,  $\text{WS}_2$ ). For instance, Geng and coworkers reported the synthesis of pure 1T- $\text{MoS}_2$  nanosheets by employing octahedral  $\text{MoO}_3$  as the starting material through a pressurized hydrothermal process.<sup>25</sup> The synthesis was performed at 200 °C by mixing  $\text{MoO}_3$ , thioacetamide and urea in an autoclave at a low pH value (pH~4). The obtained  $\text{MoS}_2$  nanosheets were 100 nm in size and a few nanometres in thickness.<sup>25</sup> The structure of 1T- $\text{MoS}_2$  nanosheets was distinguished from 2H- $\text{MoS}_2$  through ultraviolet-visible (UV-Vis) spectroscopy, Raman, TEM, and XPS. Interestingly, a unique Raman peak located at 146  $\text{cm}^{-1}$ , corresponding to the metal-metal stretching mode, was observed. As another example, Mahler and coworkers reported the preparation of distorted octahedral 1T'- $\text{WS}_2$

nanosheet by using the  $\text{WCl}_6$  and carbon disulfide ( $\text{CS}_2$ ) as precursors in an oleylamine solution.<sup>35</sup> Interestingly, introducing a small amount of hexamethyldisilazane in the reaction led to the growth of 2H phase flower-like  $\text{WS}_2$  nanosheet.

### 2.2.2 Phase transformation

In addition to direct synthesis of 1T/1T' nanostructures, phase transformation is another widely used method to achieve 1T/1T' phase TMDs. It is well known that polymorph structures of TMDs strongly depend on the *d* orbital electron density of the transition metal. Thus, the phases of TMDs can be tailored by tuning the filling of *d* orbitals. To date, various strategies, such as alkali-metal treatment, electron/laser beam irradiation,<sup>139</sup>,<sup>140</sup> plasma treatment,<sup>141</sup> strain,<sup>142</sup> heat treatment,<sup>143</sup> high pressure,<sup>144</sup>,<sup>145</sup> and electrostatic doping,<sup>146</sup> have been employed to induce the structural transformation of TMDs.

The alkaline-metal (e.g., Li, Na, K) treatment is one of the most popular protocols to engineer the phase of TMDs, especially for group VI TMDs such as  $\text{MoS}_2$ ,  $\text{MoSe}_2$  and  $\text{WS}_2$ . As early as 1983, Py and coworkers demonstrated that the electron transfer from the Li atoms to the  $\text{MoS}_2$  could increase the electron density in the *d* orbital of Mo atoms, transforming the phase of  $\text{MoS}_2$  from 2H to 1T.<sup>147</sup> Inspired by it, many compounds containing alkaline metals have been utilized to engineer the phase of TMDs. The most commonly used compound is the hexane solution of n-butyllithium, which can chemically intercalate into the TMD layers and induce the phase transformation. For example, Eda and coworkers exfoliated  $\text{MoS}_2$  nanosheets via the intercalation of n-butyllithium, and three phases of  $\text{MoS}_2$  including 1H phase, 1T phase and distorted 1T' phase were observed.<sup>148</sup> Similarly, the 1T'- $\text{WS}_2$  nanosheets consisting of zig-zag chains

has also been observed in the chemically exfoliated WS<sub>2</sub> nanosheets.<sup>149</sup> As another example, Zheng and coworkers exfoliated a series of TMD nanosheets by intercalation of aphanthenide adducts (A<sup>+</sup>C<sub>10</sub>H<sub>8</sub><sup>-</sup>, A= Li, Na, K) into the hydrazine pre-exfoliated TMDs.<sup>150</sup> The exfoliated TMD nanosheets exhibited both 1H and 1T phase. All the aforementioned lithiation processes were realized in solution. Recently, lithiation has been achieved in solid state by mixing TMD with lithium compound powers or lithium metals. For example, the mixture of MoS<sub>2</sub> and lithium borohydride, obtained by annealing the mixture at 350 °C, have been directly used for preparation of single-layer MoS<sub>2</sub> nanosheets through liquid exfoliation.<sup>151</sup> The obtained MoS<sub>2</sub> nanosheets contained ~84% 1T phase. Yin and coworkers reported the preparation of porous metallic 1T phase (82%) MoS<sub>2</sub> nanosheets by using a liquid-ammonia-assisted lithiation route.<sup>152</sup> The MoS<sub>2</sub> power was first mixed with lithium pieces. Then, the ammonia gas was introduced and condensed into liquid, allowing the reaction of ammonia and lithium for subsequent phase engineering of MoS<sub>2</sub>. Furthermore, the Li metals can be directly used for inducing the phase changes of TMDs. For instance, Tan and coworkers reported the phase transition of MoS<sub>2</sub> from 2H to 1T' by controllable evaporation of Li in ultrahigh vacuum.<sup>153</sup> Interestingly, after annealing the intercalated Li to form LiH, the 1T'-MoS<sub>2</sub> could be stabilized for long time in air without transforming back to 2H phase (**Figure 6D, E**). It was suggested that intercalated LiH is a good electron donor which can stabilize the 1T' phase in air, and the TMDs layers protect the sandwiched LiH from the ambient environment.

Different from the aforementioned methods, recently, our group developed an electrochemical lithium intercalation and exfoliation method, for high-yield production of

2D layered nanosheets. Simultaneously, the obtained TMD nanosheets also showed phase transformation.<sup>10,21,27,154,155</sup> Our experiment was performed in a battery test system with a lithium foil anode and TMD-containing cathode. During the galvanic discharge process in the cell, the Li<sup>+</sup> ions were intercalated into the layered TMD and induced the phase transformation. The greatest advantage of this method is that the phase transformation process can be precisely tuned by controlling the discharge process.<sup>21,27,156</sup>

Compared with the alkaline-metal treatment, the beam irradiation (e.g., electron beam, laser, light) can precisely pattern TMDs with alternating 1T and 2H phases, creating well-defined in-plane crystal-phase heterostructures. Lin and coworkers characterized the phase transformation of MoS<sub>2</sub> using in-situ TEM technique, and found that the phase transformation in monolayer MoS<sub>2</sub> was attributed to the gliding of the atomic planes of sulphur and/or molybdenum.<sup>140</sup> The phase transformation required an intermediate phase ( $\alpha$ -phase) as precursor, and the migration of two kinds of boundaries ( $\beta$ - and  $\gamma$ -boundaries) was responsible for the growth of the second phase. As shown in **Figure 6F**, after 100 s drilling, a new phase (denoted as  $\alpha$ ) was formed on the MoS<sub>2</sub> basal plane, forming two stripes with an angle of 60°. Rapidly, the 2H phase between the two stripes converted into the 1T phase. As time increased, the 1T phase domains grew and two new types of boundaries, denoted as  $\beta$  and  $\gamma$ , appeared. Moreover, the area of 1T phase can be controllably enlarged under electron beam as function of time (**Figure 6F**).<sup>140</sup> Very recently, laser beam irradiation has also been reported to induce the phase transformation of MoTe<sub>2</sub> nanosheet from 2H to 1T' phase (**Figure 6G**).<sup>51</sup> It was suggested that the laser irradiation could generate Te vacancy on 2H-MoTe<sub>2</sub> nanosheet. When the concentration of Te vacancy exceeded 3%, the 2H phase MoTe<sub>2</sub> became less stable than 1T'-MoTe<sub>2</sub>.

After continuous laser irradiation, a phase transformation occurred from 2H to 1T' phase.

Introduction of tensile or compressive strain is another effective way to modulate the phases and modify the bandgap and optical properties of TMDs. For example, biaxial tensile strain led to a red-shift in the band gap of semiconducting TMDs.<sup>157, 158</sup> Interestingly, 1H-MoS<sub>2</sub> and WS<sub>2</sub> became metallic upon an isotropic tensile strain, whereas they remained as semiconducting at uniaxial strain.<sup>159</sup> Generally, the strain on ultrathin MoS<sub>2</sub> nanosheets is generated by folding the nanosheets or bending the substrate (**Figure 6H**).<sup>160</sup> The recent work by Zhao and coworkers demonstrated that the rough substrate surface could also affect the transition behaviour of ultrathin 1T-TaS<sub>2</sub> nanosheets.<sup>123</sup> The 1T-TaS<sub>2</sub> showed phase transition based on the formation of commensurate charge density waves (CCDW) at 180 K. Engineering the surface strain through patterning of SiO<sub>2</sub>/Si substrates could tune the CCDW behaviour. It was concluded that higher roughness led to smaller transition hysteresis and stabilized CCDW structures at higher temperature.

In addition to the aforementioned methods, Ar plasma treatment,<sup>161</sup> heat treatment,<sup>143</sup> high pressure,<sup>144, 145</sup> etc. are also capable for inducing the phase transitions. For instance, Zhu and coworkers reported that weak Ar plasma treatment induced local phase transition of MoS<sub>2</sub> from 2H to 1T, forming mosaic structured MoS<sub>2</sub>.<sup>161</sup> The STEM image showed that the phase transition was stabilized by point defects (single S-vacancies), and the size of the 1T domains was typically in a few nanometers. Similar with the beam irradiation, Kang and coworkers reported a reversible 2H-to-1T phase transformation in a MoS<sub>2</sub> monolayer by light irradiation of Au-MoS<sub>2</sub> hybrid.<sup>141</sup> The plasmonic hot electrons generated by Au nanoparticles induced the phase transformation of MoS<sub>2</sub>. This phase

transformation was controlled by the incident light wavelength, intensity, and sample areas, leading to the tuneable shift of photoluminescence.<sup>141</sup>

### 2.2.3 TMD crystal-phase heterostructures

The in-plane TMD crystal-phase heterostructures which combine different phases/properties within an isoelectronic monolayer are promising to tune the electronic and optoelectronic functionality of 2D TMD systems. For example, Kappera and coworkers reported the local phase pattern of MoS<sub>2</sub> nanosheets.<sup>48</sup> The MoS<sub>2</sub> nanosheets were first covered by Poly(methyl methacrylate) (PMMA). Then, the PMMA was selectively removed by e-beam lithography. After that, the unmasked areas were converted to 1T phase through the lithiation treatment, forming patterned 1T and 1H phase within one TMD nanosheet. However, the aforementioned process usually needs multiple steps and the PMMA residual may deteriorate their performance. Cho and coworkers fabricated a crystal-phase heterostructures between semiconducting 1H and metallic 1T'-MoTe<sub>2</sub> using laser irradiation.<sup>51</sup> One of the advantages is that the area of patterned 1T' phase on the MoTe<sub>2</sub> nanosheet could be easily controlled by tuning the location of laser irradiation.

Most recently, direct growth of TMD crystal-phase heterostructures through chemical reaction is emerging as an effective way to construct in-plane homojunction. Sung and coworkers reported the heteroepitaxy growth of metallic 1T'-MoTe<sub>2</sub> and semiconducting 2H MoTe<sub>2</sub> crystals within the same 2D atomic plane.<sup>50</sup> The growth temperature ( $T_G$ ) is critical for controlling the phase. The experiment at  $T_G = 710$  °C produced rectangular- and trapezoidal-facet 1T'-MoTe<sub>2</sub>, and the other one at  $T_G = 670$  °C produced the

hexagonal and triangular facets 2H-MoTe<sub>2</sub> (**Figure 7A**). The 1T' and 2H mixture was produced at an intermediate T<sub>G</sub> (i.e., 670-710 °C). The 2D polymorphic coplanar structure was prepared by the heteroepitaxy growth through vapour deposition at two different values of T<sub>G</sub>, resulting in two crystallographic variants at the 1T'-2H interfaces (**Figure 7B, C**). The first type had the [01-10]<sub>2H</sub>//[200]<sub>1T'</sub> interface, in which an edge of the hexagonal 2H facets connected with the long facet edges of the monoclinic 1T' phase. The second type had the [01-10]<sub>2H</sub>//[220]<sub>1T'</sub> interface, in which the 2H edge was connected with a short 1T' facet edge. The low-magnification ADF-STEM image of the first type (**Figure 7D**) showed atomically ordered (01-10)2H//(200)1T' heterointerface. Moreover, the selected area electron diffraction (SAED) patterns obtained from the 1T'/2H interface (**Figure 7E**) showed that the (2-1-10) and (01-10) spots of 2H phase were overlapped with the (020) and (200) of 1T' phase, indicating heterointerfaces had two polymorphic unit cells. The ADF-STEM and image simulations of the interface (**Figure 7F**) further demonstrated that the (200) plane of the 1T' was bonded to the (01-10) plane of 2H at the zigzag edge. As another example, Lin and coworkers demonstrated the growth of intrinsically patterned 1H/1T PtSe<sub>2</sub> and CuSe nanostructures with triangular pattern shape.<sup>49</sup> Two PtSe<sub>2</sub> phases, i.e., 1H and 1T, were on the monolayer PtSe<sub>2</sub> nanosheet (represented by the blue and yellow triangles, respectively). The scanning tunnelling microscope (STM) image clearly showed the honeycomb feature of the 1H phase and the hexagonal feature of the 1T phase. Typically, 1T-PtSe<sub>2</sub> was first synthesized on a Pt (111) substrate by direct selenization of Pt substrate. Then the homogeneous 1T-PtSe<sub>2</sub> nanosheet was transformed to triangular patterned 1T/1H structure by annealing it at 400 °C. The transformation process was monitored by XPS

and I ( $\chi$ ) spectra (to determine the local work-function). The high-temperature treatment led to the selenium vacancies, as marked by the yellow arrow, in the film. The size of the triangles could be tuned by varying the density of deposited Se atoms. Importantly, the transformation from pure 1T phase to patterned 1H/1T phase was reversible. By adding Se atoms and treating the sample at  $\sim 270$  °C, the triangular patterned 1T/1H structure reverted to a defect-free homogeneous 1T structure. Besides the 1H/1T patterned PtSe<sub>2</sub>, an intrinsically patterned monolayer CuSe with periodic arrays of triangular nanopores was also synthesized by direct selenization of Cu (111) substrate. The distinguished patterns of the two phases showed different preference for adsorption of molecular species.

### 2.3 TMD heterostructures

Due to unique 2D structure, the ultrathin TMD nanosheets can easily form vertical or lateral heterostructures. Previously, the vertically stacked vdW heterostructures comprising multi-layered nanosheets were prepared by manually stacking different exfoliated nanosheets, in which the interlayer vdW force held the heterostructure.<sup>15,45,162</sup> Using this procedure, a number of heterostructures such as graphene/MX<sub>2</sub>, BN/MX<sub>2</sub>, BP/MX<sub>2</sub>, MX<sub>2</sub>/M'X'<sub>2</sub> (e.g., MoS<sub>2</sub>/WS<sub>2</sub>, MoS<sub>2</sub>/WSe<sub>2</sub> and MoSe<sub>2</sub>/WSe<sub>2</sub>) have been fabricated. However, stacking of those nanosheets is commonly operated through dry-transfer process, during which the polymer contaminations are introduced. Moreover, the stacking procedure is neither scalable nor controllable, and the stacking area and orientation are difficult to be controlled. In contrast, the direct growth of two different TMD nanosheets together is promising to construct vertical or lateral 2D TMD

heterostructures with clean heterojunction interface. Up to now, a great number of 2D TMD heterostructures has been prepared by direct synthesis methods.

### 2.3.1 Vertical heterostructure

Recently, a special type of material with a natural vdW heterostructure of alternating sulphide layers is emerging. These materials include a number of rare minerals, such as franckeite (e.g.,  $Pb_5Sn_2FeSb_2S_{14}$ ), cylindrite (e.g.,  $Pb_3Sn_4FeSb_2S_{14}$ ), and meneghinite (e.g.,  $Pb_{13}CuSb_7S_{24}$ ). Due to their naturally layered structure, these materials can be exfoliated to ultrathin 2D heterostructured nanosheets.<sup>163-165</sup> Molina-Mendoza and coworkers<sup>164</sup> reported the exfoliation of  $PbS-SnS_2$ , one kind of franckeite, into few-layer nanosheets. The bulk  $PbS-SnS_2$  crystals had a single-crystalline layered structure formed by alternated stacking of  $SnS_2$  and  $PbS$  layers, with thickness of a unit cell 1.7 nm. The ultrathin  $PbS-SnS_2$  vertical heterostructures with thickness of ~7 nm were obtained by mechanical exfoliation of the bulk crystals. The SAED pattern was indexed to the tetragonal  $PbS$  and orthohexagonal  $SnS_2$  layer. Moreover, the solution dispersed  $PbS-SnS_2$  nanosheets could also be obtained by sonicating the bulk  $PbS-SnS_2$  crystal in N-methyl-2-pyrrolidone (NMP) or isopropyl alcohol (IPA)/water.<sup>164</sup> As another example, Velickyet and coworkers reported the mechanical exfoliation of  $Pb_{6.0}Sn_{2.0}Sb_{2.4}S_{13.8}O_{1.0}$  nanosheets with single unit cell thickness of ~1.85 nm.<sup>165</sup> Also, the solution-dispersions containing few-layer nanosheets were obtained by sonicating the bulk crystals in solvents, such as N-methyl-2-pyrrolidone (NMP), dimethylformamide (DMF), acetone, and IPA.<sup>165</sup>

In contrast to the exfoliation of natural vdW heterostructures, growth of different TMD

nanosheets together through CVD technique is more applicable for construction of 2D vertical heterostructures in a controllable manner. State-of-art CVD processes are capable of growing many vertical heterostructures such as GaSe/graphene,<sup>166</sup> MoS<sub>2</sub>/graphene,<sup>167-</sup><sup>169</sup> MoS<sub>2</sub>/*h*-BN,<sup>170,171</sup> WS<sub>2</sub>/*h*-BN,<sup>172</sup> ReS<sub>2</sub>-WS<sub>2</sub>,<sup>173</sup> MoTe<sub>2</sub>/MoS<sub>2</sub>,<sup>174</sup> WS<sub>2</sub>/MoS<sub>2</sub>,<sup>175</sup> MoSe<sub>2</sub>/HfSe<sub>2</sub>,<sup>176</sup> SnS<sub>2</sub>-MoS<sub>2</sub>,<sup>177</sup> GaSe-MoSe<sub>2</sub>,<sup>178</sup> CdI<sub>2</sub>-MoS<sub>2</sub>,<sup>179</sup> CdI<sub>2</sub>-WS<sub>2</sub>,<sup>179</sup> CdI<sub>2</sub>-WSe<sub>2</sub>,<sup>179</sup> BiI<sub>3</sub>/WSe<sub>2</sub>,<sup>180</sup> VSe<sub>2</sub>/GeSe<sub>2</sub>,<sup>181</sup> MoS<sub>2</sub>/WSe<sub>2</sub>/graphene<sup>182</sup> and WSe<sub>2</sub>/MoSe<sub>2</sub>/graphene.<sup>182</sup> The earlier works on 2D heterostructure started with *h*-BN and graphene due to their similar lattice constants. Recently, it was found that the vertical growth of 2D nanomaterials could tolerate the lattice difference of two compounds, and the as-formed 2D heterostructure utilized strains to accommodate the lattice mismatch. For example, Shi and coworkers prepared the vertically stacked MoS<sub>2</sub>/graphene heterostructure by thermal decomposition of ammonium thiomolybdate precursor on graphene surface.<sup>169</sup> Although the lattice constant of MoS<sub>2</sub> was ~28% greater than that of graphene, the MoS<sub>2</sub> and graphene layers still matched each other in the heterostructure. Furthermore, Lin and coworkers successfully achieved the growth of MoS<sub>2</sub>, WSe<sub>2</sub>, and *h*-BN on graphene through CVD method.<sup>168</sup> Besides the graphene/MX<sub>2</sub> heterostructure, other kinds of 2D heterostructures with large lattice mismatch, such as SnS<sub>2</sub>-MoS<sub>2</sub>,<sup>177</sup> GaSe-MoSe<sub>2</sub>,<sup>178</sup> CdI<sub>2</sub>-MoS<sub>2</sub>,<sup>179</sup> CdI<sub>2</sub>-WS<sub>2</sub>,<sup>179</sup> CdI<sub>2</sub>-WSe<sub>2</sub>,<sup>179</sup> and BiI<sub>3</sub>/WSe<sub>2</sub>,<sup>180</sup> have also been prepared by CVD method. For example, Li and coworkers reported the growth of GaSe-MoSe<sub>2</sub> (lattice mismatch of ~13% between GaSe and MoSe<sub>2</sub>) vertical and lateral heterostructures using a two-step CVD method.<sup>178</sup> Single-layer MoSe<sub>2</sub> nanosheets were first grown on a SiO<sub>2</sub>/Si substrate and then used as templates for the subsequent growth of GaSe nanosheets. By controlling the Ar flow during the GaSe growth process, the

GaSe could be grown vertically or laterally on MoSe<sub>2</sub> nanosheets. The low gas flow rate led to the vertical growth, and the high gas flow rate led to the lateral growth. The ADF-STEM and corresponding fast Fourier transform (FFT) image showed that the vertically stacked GaSe/MoSe<sub>2</sub> heterostructures exhibited vdW epitaxy growth with well-aligned lattice orientation between the two layers. However, no epitaxial alignment was observed at the interface between GaSe and MoSe<sub>2</sub> in lateral heterostructures. As another example, the Duan group reported the preparation of CdI<sub>2</sub>/MoS<sub>2</sub>, CdI<sub>2</sub>/WSe<sub>2</sub>, CdI<sub>2</sub>/WS<sub>2</sub>, and BiI<sub>3</sub>/WSe<sub>2</sub> vdW heterostructures by growing CdI<sub>2</sub><sup>179</sup> and BiI<sub>3</sub><sup>180</sup> nanoplates on the surfaces of TMD nanosheets through a two-step CVD process, respectively. Interestingly, using patterned WS<sub>2</sub> monolayer square arrays as the nucleation and growth templates, the regular arrays of CdI<sub>2</sub>/WS<sub>2</sub> vertical heterostructures were synthesized.

Besides the aforementioned vertical heterostructures with large lattice mismatch, the nearly lattice-matched TMD based vertical heterostructures are also receiving considerable attention. For example, the WS<sub>2</sub>/MoS<sub>2</sub> heterobilayer was grown on a Si/SiO<sub>2</sub> substrate at 850 °C through one-step CVD process<sup>175</sup> (**Figure 8A-D**). The growth behaviour, either vertical or lateral, was temperature-dependent. The lateral MoS<sub>2</sub>-WS<sub>2</sub> heterostructure was obtained below 650 °C, while the vertical stacked MoS<sub>2</sub>-WS<sub>2</sub> heterostructure was obtained above 850 °C. Such temperature-dependent growth was attributed to the difference in the nucleation rate and growth rate of MoS<sub>2</sub> and WS<sub>2</sub>. Later on, a temperature-mediated two-step CVD strategy was developed to synthesize MoS<sub>2</sub>/WS<sub>2</sub> and WS<sub>2</sub>/MoS<sub>2</sub> vertical heterostructures on Au foil.<sup>183</sup> Since the growth temperature of WS<sub>2</sub> (i.e., 880 °C) was much higher than that of MoS<sub>2</sub> (i.e., 660 °C), the heterostructures were achieved by sequentially growing the individual MX<sub>2</sub> monolayers

under different temperatures. The MoS<sub>2</sub>/WS<sub>2</sub> heterostructures were prepared by the growth of MoS<sub>2</sub> nanosheets on Au substrate at ~ 680 °C, followed by the growth of WS<sub>2</sub> nanosheets on MoS<sub>2</sub> surface at ~ 880 °C.

Controlling of the stacking manner of two TMDs (e.g., the overlap percentage, stacking angle) is highly desired because it can affect the optical/electronic properties of the heterostructures. Recently, Zhang and coworkers demonstrated the twinned growth of ReS<sub>2</sub>/WS<sub>2</sub> vertical heterostructure, with 100% overlap of ReS<sub>2</sub> and WS<sub>2</sub> (**Figure 8E-G**).<sup>173</sup> For the twinned growth of ReS<sub>2</sub>-WS<sub>2</sub> vertical heterostructures, a special Au foil containing Re and W atoms was used as the substrate. The Au substrate was sulfurized with H<sub>2</sub>S gas in a CVD furnace to form ReS<sub>2</sub>-WS<sub>2</sub> vertical heterostructures (**Figure 8E**). The ReS<sub>2</sub>-WS<sub>2</sub> vertical heterostructures were triangular with size of tens of micrometres (**Figure 8F, G**). Interestingly, the bottom WS<sub>2</sub> layer was fully covered by the top ReS<sub>2</sub> layer with the exact same lateral size and shape, evidenced by optical microscopy image, Raman mapping and Raman spectra (**Figure 8H-J**). This strategy is promising for the fabrication of other fully overlapped 2D vdW heterostructures.

### 2.3.2 Laterally growth of 2D heterojunctions

#### One-step synthesis method

The 2D lateral heterostructure offers the possibility to construct heterojunctions with desired patterns and compositions. Particularly, the small lattice mismatch of the TMD family ensures that the lateral heterostructures are nearly pristine, with few defects at the heterojunction. CVD method is the most controllable way to synthesize lateral

heterostructures, through either one-step or two-step synthetic processes. For instance, Gong and coworkers reported the growth of in-plane lateral heterojunctions of WS<sub>2</sub> and MoS<sub>2</sub> within single hexagonal monolayer lattice, based on the different nucleation and growth rate of MoS<sub>2</sub> and WS<sub>2</sub>.<sup>175,184</sup> Huang and coworkers achieved the growth of the MoSe<sub>2</sub>-WSe<sub>2</sub> lateral heterostructure by evaporating MoSe<sub>2</sub> and WSe<sub>2</sub> powders in a CVD furnace.<sup>185</sup> Due to the different volatilities of MoSe<sub>2</sub> and WSe<sub>2</sub>, the MoSe<sub>2</sub> nanosheets were first deposited on substrate, and the WSe<sub>2</sub> was then laterally grown on the existing MoSe<sub>2</sub> to form the lateral heterostructure. Recently, an intriguing in-plane monolayer heterostructure composing of 1H-MoS<sub>2</sub> and 1T'-MoTe<sub>2</sub> was prepared.<sup>186</sup> The single-crystal 1H-MoS<sub>2</sub> nanosheets were first grown, and the single-crystal 1T'-MoTe<sub>2</sub> was then nucleated at the 1H-MoS<sub>2</sub> edge to form the 1H-MoS<sub>2</sub>/1T'-MoTe<sub>2</sub> heterostructure. The optical image showed that the 1T'-MoTe<sub>2</sub>, which had needle shapes, grew at the edge of triangular 1H-MoS<sub>2</sub>. The XPS data confirmed the chemical composition, and the tip-enhanced Raman spectroscopy (TERS) distinguished the differences between the 1H and 1T'-regions. Other lateral heterostructures, including MoS<sub>2</sub>-WS<sub>2</sub> and MoSe<sub>2</sub>-WSe<sub>2</sub><sup>187</sup> have also been prepared. The aforementioned one-step processes share some similarities. First, two or more metal precursors are simultaneously presented in the reaction chamber. Second, the subsequent volatilization and deposition process happen on the same substrate. Usually, the material with higher vapour pressure and nucleation rate is formed at the core of the heterostructures. Third, the second material grows at the reactive edge of the existing nanosheet.

### Two-step synthesis method

In two-step growth process, the core material is first grown, and the second material is

grown along the edge of the core material after exchanging precursors, forming lateral heterostructures. The work reported by Duan and coworkers demonstrated the synthesis of MoS<sub>2</sub>-MoSe<sub>2</sub> and WS<sub>2</sub>-WSe<sub>2</sub> heterostructures.<sup>188</sup> The MoS<sub>2</sub> (or WS<sub>2</sub>) nanosheets were first grown on the substrate using their powder precursors. Then, the powder source was changed to MoSe<sub>2</sub> (or WSe<sub>2</sub>), and the MoSe<sub>2</sub> (or WSe<sub>2</sub>) was continuously epitaxially grown on the edge site of the MoS<sub>2</sub> (or WSe<sub>2</sub>) seeds to form lateral heterostructures. Until now, the typical synthetic protocols include: (1) partial sulfurization of CVD-grown diselenides, (2) partial selenization of CVD-grown disulfides and (3) formation of lateral junctions by *in-situ* switching precursors. The two-step growth showed great advantages in controlling the interface structures of heterostructure. For example, Li and coworkers reported the epitaxial growth of WSe<sub>2</sub>-MoS<sub>2</sub> lateral heterostructure by a two-step CVD method.<sup>189</sup> The monolayer WSe<sub>2</sub> was first prepared on substrate by using the vdW epitaxy technique. Followed by the edge epitaxy growth of MoS<sub>2</sub> along the W growth front of WSe<sub>2</sub>, the WSe<sub>2</sub>-MoS<sub>2</sub> lateral heterostructure was formed. Different with the lateral heterostructures prepared by one-step method with alloy-like structure at the interface regions, the obtained WSe<sub>2</sub>-MoS<sub>2</sub> lateral heterostructure had atomically sharp interface between WSe<sub>2</sub> and MoS<sub>2</sub> (**Figure 9A, B**). Similar procedure was adopted to prepare the lateral WSe<sub>2</sub>-WS<sub>2</sub> heterostructure, which also exhibited an atomically sharp interface.<sup>190</sup>

During the second step of growth of lateral heterostructures, it is critical to suppress the formation of vertically stacked heterostructures or alloys. Recently, Yoo and coworkers demonstrated that the introduction of hydrogen gas during CVD process led to the formation of in-plane MoS<sub>2</sub>/WS<sub>2</sub> heterostructures.<sup>191</sup> The hydrogen gas resulted in ultraclean MoS<sub>2</sub> monolayers, which suppressed the vertical growth of WS<sub>2</sub> layers but

promoted the lateral growth of heteroepitaxial WS<sub>2</sub> monolayer. Bogaert and coworkers demonstrated the importance of growth temperature, which could induce the in-plan composition diffusion when synthesis of WS<sub>2</sub>-MoS<sub>2</sub> heterostructure.<sup>192</sup> The WS<sub>2</sub> nanosheet was first grown as core material and MoS<sub>2</sub> was grown as the second materials. Interestingly, after growth of MoS<sub>2</sub> at 650 °C, MoS<sub>2</sub> was found in the core, opposite from the order where the precursors were introduced into the CVD chamber. It was suggested that the Mo atoms were absorbed at the edge of WS<sub>2</sub> crystals and diffused throughout the crystals. At low growth temperature ( $T_{G(2)} = 650$  °C), the resulting crystals consisted of MoS<sub>2</sub> core surrounded by Mo<sub>1-x</sub>W<sub>x</sub>S<sub>2</sub> ring, while at higher growth temperatures ( $T_{G(2)}=680\text{-}710$  °C) an evenly distributed Mo<sub>1-x</sub>W<sub>x</sub>S<sub>2</sub> alloy was formed. Besides the carrier gas and the growth temperature, the thickness of the first-grown core nanosheets is also important for the composition of the heterostructure. Li and coworkers reported the synthesis of MoS<sub>2</sub>-MoS<sub>2(1-x)</sub>Se<sub>2x</sub> (0<x<1) lateral heterostructures via the two-step CVD process.<sup>193</sup> It was found that the selenization temperature in the second growth step depended on the layer number of MoS<sub>2</sub>, i.e., the temperature for selenium substitution on the monolayer MoS<sub>2</sub> was lower than that on the bilayer and multilayer. A stacked MoS<sub>2</sub> nanosheet which had a smaller nanosheet located at the top center of another larger nanosheet was used for demonstration. By controlling the selenization time, the S at the monolayer core MoS<sub>2</sub> at the peripheral area can be selectively substituted by Se atoms at different levels, while the bilayer region at the centre retains the original composition, thus forming MoS<sub>2</sub>-MoS<sub>2(1-x)</sub>Se<sub>2x</sub> lateral heterostructures.

### Step-by-step synthesis method

The growth procedure can be further repeated for multiple steps to produce the multi-

material heterostructures and superlattices. Recently, Zhang and coworkers prepared a wide range of superlattices, such as  $\text{WS}_2\text{-WSe}_2\text{-MoS}_2$ ,  $\text{WS}_2\text{-MoSe}_2\text{-WSe}_2$  and  $\text{WS}_2\text{-WSe}_2\text{-WS}_2\text{-WSe}_2\text{-WS}_2$  with precisely controlled spatial-modulation (**Figure 9C, D**).<sup>46</sup> The fabrication process was a step-by-step thermal CVD process (**Figure 9C**), in which the core nanosheets were first grown, and the heterostructures were formed by the continued lateral epitaxial growth at the edge of the existing monolayer crystals (**Figure 9D**). For example, the  $\text{WS}_2$  nanosheets were first grown by vaporization of  $\text{WS}_2$  powders under a flow of argon carrier gas. Then, the second material (i.e.,  $\text{MoS}_2$ ) was formed by the continued lateral epitaxial growth at the edge of the  $\text{WS}_2$ , and the third compound was deposited at the edge of second-grown  $\text{MoS}_2$ .<sup>46</sup> In order to avoid the excessive thermal degradation or uncontrolled nucleation during the temperature swing among sequential growth steps, a reversed gas flow from the substrate to the source powders was used. The reversed flow could also eliminate the uncontrolled homogeneous nucleation. The TEM image showed atomically sharp interfaces between each layer. As another example, Tsai and coworkers demonstrated the preparation of monolayer  $\text{WS}_2/\text{WS}_{2(1-x)}\text{Se}_{2x}/\text{WS}_2$  multijunction lateral heterostructure through an *in-situ* three-step CVD growth process.<sup>194</sup> The monolayer  $\text{WS}_2$  nanosheets were first grown on sapphire substrate by reacting  $\text{WO}_3$  powder with sulfur vapor. Then the selenium vapor was introduced into the furnace. The  $\text{WS}_{2(1-x)}\text{Se}_{2x}$  alloy was formed at the activated  $\text{WS}_2$  edge, forming  $\text{WS}_2\text{-WS}_{2(1-x)}\text{Se}_{2x}$  heterostructure. After that, the sulfur vapor was introduced again to form the outermost  $\text{WS}_2$  ring, forming the core–ring–ring  $\text{WS}_2/\text{WS}_{2(1-x)}\text{Se}_{2x}/\text{WS}_2$  structure. The average Se content was estimated to be  $x\sim 13\%$  by ADF-STEM image. The lateral compositional profile of  $\text{WS}_2/\text{WS}_{1.75}\text{Se}_{0.25}/\text{WS}_2$  configuration was further confirmed by Raman, PL, and

ADF-STEM measurements.

### Patterning growth

Area-selective growth through patterning is promising to synthesize heterostructure with desirable shape and size, which is attractive for fabrication of large-scale TMD-based integrated circuit. For example, Mahjouri-Samani and coworkers reported the preparation of patterned MoSe<sub>2</sub>-MoS<sub>2</sub> lateral heterostructures.<sup>195</sup> Typically, the monolayer MoSe<sub>2</sub> nanosheets were prepared by CVD method and selectively masked by electron beam lithography. The unmarked areas of MoSe<sub>2</sub> were then sulfurized to MoS<sub>2</sub> by pulsed laser vaporization of sulfur, forming the patterned MoSe<sub>2</sub>-MoS<sub>2</sub> lateral heterostructures. The shape of patterned areas was easily tuned by controlling the mask shapes, including triangle, circle and ribbon. Later on, Li and coworkers reported the preparation of patterned WS<sub>2</sub>-WSe<sub>2</sub> lateral heterostructures by using the focused ion beam technique.<sup>196</sup> The CVD-grown WS<sub>2</sub> nanosheets were first selectively etched using focused ion beam, and the exposed WS<sub>2</sub> edges served as the seeds for subsequent growing of WSe<sub>2</sub> to form WS<sub>2</sub>-WSe<sub>2</sub> lateral heterostructures. The abovementioned patterned heterostructures were built based on two materials with similar lattice structures. Recently, Ling and coworkers prepared a series of in-plane “parallel stitched” heterostructures including metal-semiconductor (e.g., graphene-MoS<sub>2</sub>), semiconductor-semiconductor (e.g., WS<sub>2</sub>-MoS<sub>2</sub>) and insulator–semiconductor (e.g., *h*-BN-MoS<sub>2</sub>) heterostructures.<sup>197</sup> In a typical process, the first 2D nanosheets were deposited on the SiO<sub>2</sub> substrate, and perylene-3,4,9,10-tetracarboxylic acid tetrapotassium salt (PTAS) molecules were deposited as seeds to facilitate the growth of the second materials. Because the aromatic molecules were more likely to be deposited onto a hydrophilic surface (i.e., SiO<sub>2</sub>) than onto the surface of 2D

materials, the growth of second materials in the SiO<sub>2</sub> region (with PTAS molecules) was much easier, allowing the formation of parallel stitched heterostructures via growth of the second materials along the edges of the first 2D materials.

## 2.4 Janus structure

Recently, Lu and coworkers demonstrated the preparation of Janus monolayer MoSSe nanosheets, in which the Mo atoms were covalently bonded to the bottom S atoms and the top Se atoms, forming MoSSe asymmetric structure.<sup>52</sup> The typical synthetic process is schematically shown in **Figure 10A**. First, the MoS<sub>2</sub> nanosheets (~1.0 nm thickness) were grown on a sapphire substrate using CVD method. Then the top-layer of sulfur atoms were stripped off and replaced with hydrogen atoms to form MoSH using hydrogen plasma treatment. After that, the thermal selenization of MoSH allowed Se to replace the H, forming a structurally stable monolayer Janus MoSSe nanosheet. The materials obtained in each step were characterized by Raman (**Figure 10B**) and PL (**Figure 10C**). It is noteworthy that the synthetic condition should be carefully controlled to prevent the break of the integrity of nanosheets or the formation of alloyed nanosheets. The plasma power should be at an optimum value to break up the surface Mo-S bonds but maintain the underlying 2D Mo-S structure. Moreover, the subsequent selenization temperature should be higher than 350 °C for formation of Mo-Se bonding but not higher than 450 °C, because nanosheets became unstable and holes appeared in the nanosheets at temperature above 450 °C. If the selenization temperature was higher than 600 °C, the Se and S were mixed in a disordered arrangement, and randomized MoSSe alloy were formed. The STEM in **Figure 10D** and energy-dispersive X-ray spectroscopy (EDS) of

the cross-section of the Janus MoSSe nanosheets indicated that Se atoms were located at the top layer of the Janus MoSSe monolayer with an atomic percentage of 96.2%. The asymmetrical chemical bonding with vertical dipoles within MoSSe monolayers was also characterized by optical second harmonic generation and piezoresponse force microscopy. The Janus nanosheets showed out-of-plane piezoelectricity with enhanced Rashba spin-orbit interaction, promising for nanoelectromechanical devices and spintronics. In another work, Zhang and coworkers also prepared the Janus SMoSe nanosheets through a two-step CVD process.<sup>53</sup> The monolayer MoSe<sub>2</sub> nanosheets were first grown on Si/SiO<sub>2</sub> substrate at 800 °C, and the sulfur gas was carried to the site of MoSe<sub>2</sub> by ultra-high purity argon flow. The top-layer Se atoms were in direct contact with sulfur and replaced by S atoms more easily than the bottom Se atoms. They approved that the experimental temperature was critical. The temperature below 750 °C induced the formation of MoSe<sub>2</sub>, but that above 850 °C gave rise to the formation of MoS<sub>2</sub>. The obtained Janus SMoSe layer and its reverse configuration SeMoS exhibited lower overpotential than MoS<sub>2</sub> and MoSe<sub>2</sub> towards the hydrogen evolution.

### 3. Application

The recent decade has witnessed the explosive development on the research of layered TMD nanosheets. Due to their unique physiochemical properties originated from the versatile chemical compositions, tunable bandgaps and unique electronic structures, these ultrathin TMD nanosheets have been proved as fascinating candidate materials for many applications in electronics,<sup>48,51,198-200</sup> optoelectronics,<sup>132,184,198,199,201</sup> thermoelectrics,<sup>202-204</sup> catalysis,<sup>63,74,104,128,149,205-207</sup> energy conversion and storage,<sup>116, 128, 208-212</sup> biomedicine<sup>213, 214</sup> and so on. In

this part, we will mainly focus on the recent achievements on the applications of layered ultrathin TMDs.

### 3.1 Electronics/Optoelectronics

Ultrathin 2D TMD nanosheets have been widely considered as attractive semiconducting channel materials in the fabrication of high-quality electronic/optoelectronic devices because of their tunable bandgap and modulated mobility.<sup>15,16,18,19,198,199</sup> Moreover, the feasibility for preparing heterostructures and alloyed TMD nanosheets with tunable bandgaps enables the facile modulation of the electronic properties of these TMD nanosheets.<sup>15,45</sup> Therefore, many new TMD nanosheets are emerging as excellent candidates for fabrication of various electronic/optoelectronic devices with great performance and high efficiency, including field-effect transistors (FETs),<sup>48,51,130</sup> photodetectors,<sup>215-220</sup> and photodiodes.<sup>184,199,201</sup> For instance, Kappera and coworkers reported that the MoS<sub>2</sub> nanosheet could be highly effective channel material for fabrication of FETs.<sup>48</sup> Different from the conventional process of depositing the metal as contact electrodes, an organic *n*-butyllithium solution was used to partially convert the mechanically exfoliated 1H-MoS<sub>2</sub> nanosheets to metallic 1T phase, which was used as the direct contact electrodes to connect with the semiconducting channel. The semiconducting channel material was covered by PMMA to avoid the phase change. Because the work function of 1T phase and the conduction band energy (relative to vacuum level) of 1H phase is quite close, and the interface between the two phases is atomically sharp, the contact resistance of the FET was greatly reduced to 200-300 Ω μm at zero gate bias from the conventionally high resistance of 0.7-10 kΩ μm (**Figure 11A**).

Specifically, by reducing the contact resistance of the device via the phase engineering strategy, the performance of the back-gated 1T-MoS<sub>2</sub> based FETs exhibited enhanced properties with a highest on/off ratio larger than 10<sup>6</sup> (**Figure 11B**), high drive current of 85  $\mu\text{A } \mu\text{m}^{-1}$  and high mobility of  $\sim 50 \text{ cm}^2 \text{ V}^{-1} \text{ s}^{-1}$ . While for the back-gated 1H-MoS<sub>2</sub> based FETs with Au electrodes, a drive current of only 30  $\mu\text{A } \mu\text{m}^{-1}$  and low mobility of  $\sim 15\text{-}20 \text{ cm}^2 \text{ V}^{-1} \text{ s}^{-1}$  were achieved. Similar enhanced performance could also be observed in the top-gated devices based on 1T-MoS<sub>2</sub> with a highest on/off ratio larger than 10<sup>7</sup> (**Figure 11C**). Compared with the high subthreshold values of 150 mV decade<sup>-1</sup> in the top-gated 1H-MoS<sub>2</sub> based device, an excellent saturation current and low subthreshold swing values of 90 mV decade<sup>-1</sup> were achieved in the top-gated devices based on 1T-MoS<sub>2</sub> (**Figure 11C**). More importantly, the performance of these phase engineered FETs was highly reproducible and independent on the type of metal source. It is worth pointing out that the modulation of the device performance through phase engineering may be universal for most of the TMD nanosheet-based device, promoting the further development in this field.

As another example, Cho and coworkers found that the homojunction between 2H and 1T' MoTe<sub>2</sub> could be used for the fabrication of high-performance FETs.<sup>51</sup> Unlike Kappera et al.'s work using organic lithium solution,<sup>48</sup> Cho and coworkers adopted a laser irradiation technique to drive a local phase transition from 2H to 1T' in MoTe<sub>2</sub> nanosheets to form an ohmic contact (**Figure 11D**).<sup>51</sup> Interestingly, this homojunction based FETs not only showed an *n*-type transport characteristic with high on/off current ratio of 10<sup>6</sup>, but also kept the crystal-phase heterostructure in high temperature of 300 °C with stable output, allowing the device to be operated at high-temperature environment

(**Figure 11E**). This crystal-phase heterostructure based device showed great enhancement on field-effect mobility with 50 times that of the conventional counterpart device with 2H-MoTe<sub>2</sub>/metal contact (**Figure 11F**). Compared with the common Schottky contact between 2H-MoTe<sub>2</sub> and metal electrode, the very small energy difference between the electron affinity of 2H-MoTe<sub>2</sub> and the work function of 1T'-MoTe<sub>2</sub> was concluded to be responsible for the fast interlayer charge transfer between the 2H-MoTe<sub>2</sub>/1T'-MoTe<sub>2</sub> contact, similar with the observation by Kappera et al.<sup>48</sup>

Moreover, Zhou and coworkers demonstrated that the CVD-grown large-area 2H-MoTe<sub>2</sub> nanosheets could be applied in the fabrication of FET device with the channel length from 300 nm to 6.5 μm (**Figure 11G**).<sup>130</sup> It is noteworthy that this 2H-MoTe<sub>2</sub> based device exhibited *p*-type characteristic with an on/off current ratio of ~10<sup>3</sup> and an estimated carrier concentration over  $4.8 \times 10^{12} \text{ cm}^{-2}$ , which was different with other group VI TMDs (e.g., MoS<sub>2</sub>, MoSe<sub>2</sub>, WS<sub>2</sub>) acting as *n*-type semiconductors (**Figure 11H, I**). The observed hole mobility of the 2H-MoTe<sub>2</sub> based device was comparable to that of the back-gated device based on mechanically exfoliated MoTe<sub>2</sub> nanoflakes, reaching a value of  $1 \text{ cm}^2 \text{ V}^{-1} \text{ s}^{-1}$ .

Beside MoS<sub>2</sub> and MoTe<sub>2</sub>, a uniform and large-area WSe<sub>2</sub> with limited layer numbers was also used for fabrication of FET devices, showing excellent *p*-type transport characteristic with an on/off current ratio of ~10<sup>6</sup> and a hole mobility of around  $2.2 \text{ cm}^2 \text{ V}^{-1} \text{ s}^{-1}$ .<sup>221</sup> Furthermore, Liu and coworkers demonstrated that, when heated in air, the performances of CVD-grown monolayer and few-layer WSe<sub>2</sub> based FETs were greatly improved due to the formation of WSe<sub>2</sub>-WO<sub>3-x</sub> heterostructure during the heating process.<sup>222</sup> Specifically, by finely controlling the heating condition, the monolayer WSe<sub>2</sub> based FETs showed

greatly enhanced performance with an average FET mobility of  $31 \text{ cm}^2 \text{ V}^{-1} \text{ s}^{-1}$  and an on/off current ratio as high as  $5 \times 10^8$ , while for the few-layer WSe<sub>2</sub> based FETs, a high mobility of  $92 \text{ cm}^2 \text{ V}^{-1} \text{ s}^{-1}$  was achieved. It was confirmed that the formation of the in-plane heterojunctions between WSe<sub>2</sub> and WO<sub>3-x</sub> played an important role on the improvement of device performance. The highly conductive nature of WO<sub>3-x</sub> could introduce the *p*-type doping into the device, resulting in the increase of hole concentration and on-state current. More impressively, the fabrication of WSe<sub>2</sub> FET on BN substrate exhibited a high room temperature mobility of  $83 \text{ cm}^2 \text{ V}^{-1} \text{ s}^{-1}$  after heated in air at  $250^\circ\text{C}$ , offering a facile way to improve the device performance.

Besides the application in FET devices, some heterostructures made from ultrathin 2D TMD nanosheets have also been used for the fabrication of optoelectronic devices.<sup>132,184,198,199,201</sup> For example, Chen and coworkers demonstrated that a type II lateral heterojunction composed of MoS<sub>2</sub> and WS<sub>2</sub> could serve as a monolayer *p-n* junction.<sup>201</sup> Because the Fermi level of monolayer-core MoS<sub>2</sub> was around 95 meV higher than that of the bilayer-shell WS<sub>2</sub>, a built-in potential could be formed, resulting in the effective separation of electrons and holes. The successful formation of the *p-n* diode was further confirmed by the observation of typical current rectification behaviour. Specifically, when irradiated by a 514 nm, 1 mW laser, the WS<sub>2</sub>-MoS<sub>2</sub> heterojunction based optoelectronic device showed an obvious photovoltaic effect with an open-circuit voltage of  $\sim 0.15 \text{ V}$  and a short-circuit current of  $\sim 5.2 \text{ pA}$  (**Figure 12A**). Notably, the charge transport in this optoelectronic device is partly limited by the *n*-type MoS<sub>2</sub> due to its relatively high Fermi level compared to WS<sub>2</sub>. As another example, Gong and coworkers reported that the WSe<sub>2</sub>-MoSe<sub>2</sub> vertical heterostructure could be applied in the fabrication

of optoelectronic devices.<sup>184</sup> It was found that the built-in electrical field originating from the formation of *p-n* junction could effectively separate the photogenerated electrons and holes, making the WSe<sub>2</sub>-MoSe<sub>2</sub> vertical heterostructure promising for fabrication of photodiode. More importantly, the observed photocurrent was different between forward and reverse biases, resulting in different external quantum efficiency of 6.4 and 1.2% for forward biased and reverse biased device, respectively. The internal quantum efficiency was also different between the forward bias (91%) and reverse bias (17%). When irradiated with a 619 mW cm<sup>-2</sup> 514 nm laser, the WSe<sub>2</sub>-MoSe<sub>2</sub> heterostructure based device exhibited a clear photovoltaic effect with an open-circuit voltage of 55 mV and an incident photon to converted electron efficiency of 0.12% (**Figure 12B**). In addition, Li and coworkers demonstrated that a monolayer WSe<sub>2</sub>-MoS<sub>2</sub> lateral *p-n* junction with atomically sharp interface was promising for fabrication of photovoltaic devices.<sup>189</sup> Notably, the electrical transport curves of the fabricated device exhibited a clear characteristic rectification, revealing the photovoltaic effect and the presence of a *p-n* junction. Due to the perfect formation of in-plane heterojunction, the WSe<sub>2</sub>-MoS<sub>2</sub> based optoelectronic device showed an open-circuit voltage of 0.22 V, a short-circuit current of 7.7 pA and a fill factor of 0.39 under 1 mW cm<sup>-2</sup> light illumination, leading to a power conversion efficiency (PCE) of 0.2% (**Figure 12C**).

Besides the application in photovoltaic devices, ultrathin 2D TMD nanosheets also exhibited great potential in fabrication of high-performance photodetector.<sup>215-220</sup> As a typical example, Huang and coworkers showed that the semiconducting 2D NbSe<sub>2</sub> nanoflake could be a promising candidate for photoconduction.<sup>215</sup> Compared to the metallic bulk NbSe<sub>2</sub> crystal, the NbSe<sub>2</sub> nanoflake (thickness is around 20 nm) based

device showed a strong photoresponse to 532- and 808-nm wavelength excitations at a bias of 0.1 V, and the photocurrent linearly increased with the optical power. The photoresponsivity of the fabricated device was estimated to be  $2.3 \text{ AW}^{-1}$  and  $3.8 \text{ AW}^{-1}$  under the irradiation with 532- and 808-nm wavelengths, respectively (**Figure 12D**). It is noteworthy that the NbSe<sub>2</sub> nanoflake based device exhibited a clear ambience-dependent photoconductivity. Moreover, Zheng and coworkers demonstrated that the 2D In<sub>2</sub>Se<sub>3</sub> crystal with high photosensitivity exhibited great potential in photodetector fabrication.<sup>216</sup> Generally, an excellent photoresponsivity of  $1650 \text{ AW}^{-1}$  at a bias of 5 V could be easily observed under the 633 nm,  $622 \text{ nW cm}^{-2}$  light illumination. The photoresponsivity of the device could be further modulated by simply tuning the sample thickness, incident light power and the bias voltage, leading to a highest measured value of around  $4470 \text{ AW}^{-1}$  at a bias of 5 V. More interestingly, when packaged on a flexible polyethylene terephthalate (PET) substrate, the fabricated photodetector still maintained the stable photocurrent output under repeated bending process, making it promising for the future flexible photodetectors. Recently, another similar photodetector based on  $\beta$ -In<sub>2</sub>Se<sub>3</sub> nanosheets was reported by Almeida and coworkers, which also showed great photoresponsivity.<sup>217</sup> A linear behavior of the output current-voltage (*I-V*) curve under 532 nm laser illumination was clearly observed, indicating its strong photoresponse with a high photoresponsivity of  $10^3 \text{ AW}^{-1}$  at low laser power (few pW). More importantly, a fast response time with the rise time of 2.5 ms and a fall time of 3.7 ms was also detected, further revealing the potential of the  $\beta$ -In<sub>2</sub>Se<sub>3</sub> based photodetector. In addition, Zhou and coworkers showed that the 2D GaSe crystal synthesized at low temperature also had great potential for application in flexible photodetector.<sup>218</sup> Owing to the considerable flexibility

and suitable bandgap of 2.1 eV, the prepared GaSe nanosheets could be easily transferred onto the EVA/PET substrate to form the flexible visible-light photodetector. Such flexible device exhibited a great photoresponse effect, with a photoresponsivity of  $5 \text{ AW}^{-1}$  under a 0.2 nW 532 nm laser illumination. Notably, even under the repeated bending test with the bending radii of 25 mm, the photocurrent output could still keep stable with only slightly decrease of the on-off switching ratio, indicating the great flexibility and durability of the GaSe based photodetector. Moreover, Zheng and coworkers successfully fabricated a photodetector composed of vertically oriented few-layer HfS<sub>2</sub> with uniform thickness of around 10 nm.<sup>219</sup> Impressively, under the 405 nm laser irradiation with a power density of around  $250 \text{ Wm}^{-2}$  and the bias voltage of 1 V, the HfS<sub>2</sub> based device exhibited a good photoresponse with a low off-state current of around 1.5 pA and high on-state current of around 1.2 nA, leading to a high photosensitivity with on/off ratio of around  $10^3$ . It is noteworthy that the fabricated HfS<sub>2</sub> photodetector showed an ultrafast photoresponse time of 24 ms because of the few Hf ion vacancies in the oriented grown HfS<sub>2</sub> nanosheets. In addition, Velusamy and coworkers reported that a flexible film photodetector composed of liquid-exfoliated MoSe<sub>2</sub> nanosheets and amine-terminated poly(styrene) (PS-NH<sub>2</sub>) showed great photoresponse performance in the near-infrared (NIR) region.<sup>220</sup> Specifically, under the illumination of 1064 nm laser with the power intensity of  $238 \text{ mW cm}^{-2}$  and a bias voltage of 5 V, a photoresponsivity of  $\sim 16 \text{ AW}^{-1}$  and a current on/off ratio of  $\sim 10^5$  could be observed. More impressively, it was found that the blended composite composed of liquid-exfoliated MoSe<sub>2</sub> and MoS<sub>2</sub> with the ratio of 5:5 was used for photodetection with a broad wavelength range in both visible and NIR region. This MoS<sub>2</sub>/MoSe<sub>2</sub> composite based device showed great photoresponsivity under

both 1064 nm and 532 nm light illumination with a power density of 230 mW cm<sup>-2</sup> and 63 mW cm<sup>-2</sup>, respectively. The photodetection performance of these devices kept stable even after 1000 bending cycles at a bending radius of 1 mm, indicating their great durability. Moreover, Jia and coworkers found that a WS<sub>2</sub>-SnS<sub>2</sub> hybrid composite showed great photoresponse due to the formation of *p-n* heterojunction.<sup>223</sup> Compared with the photodetector based on pure WS<sub>2</sub>, the WS<sub>2</sub>-SnS<sub>2</sub> hybrid based device exhibited a broader photodetection range from 457 nm to 1064 nm at the NIR region as well as an enhanced detectivity by ~3 orders of magnitude. Under the 457 nm laser illumination with the power density of 0.44 W cm<sup>-2</sup> and a bias voltage of 5 V, a photocurrent of ~6 μA and a photoresponsivity of ~2 AW<sup>-1</sup> were obtained. Notably, the WS<sub>2</sub>-SnS<sub>2</sub> based photodetector showed great response characteristics with the rise time of 51 μs and decay time of 98 μs. In addition, a photocurrent of 0.32 μA and photoresponsivity of ~0.1 AW<sup>-1</sup> could also be easily achieved under the NIR light excitation of 1064 nm with the power density of 0.44 W cm<sup>-2</sup> and bias voltage of 5 V.

### 3.2 Thermoelectrics

Due to various advantages such as low production cost, environmental friendliness and wasted thermal energy recyclability, the thermoelectric materials have attracted considerable research interest in the past few years.<sup>202-204, 224</sup> Recent studies also revealed the great potential of 2D TMD nanosheets in thermoelectrics, due to their tunable electronic properties and high conductivities confined in their 2D planes.<sup>202-204</sup> As a typical example, by intercalation of Hexylammonium (HA) and dimethylsulphoxide (DMSO) into the interlayer space of layered TiS<sub>2</sub> crystal, Wan and coworkers found that

the hybrid superlattice of  $\text{TiS}_2/[(\text{HA})_{0.08}(\text{H}_2\text{O})_{0.22}(\text{DMSO})_{0.03}]$  was suitable for fabrication of flexible *n*-type thermoelectric device at a high temperature up to 120 °C.<sup>202</sup> It is worth pointing out that, compared to bulk  $\text{TiS}_2$  crystal, the  $\text{TiS}_2/[(\text{HA})_{0.08}(\text{H}_2\text{O})_{0.22}(\text{DMSO})_{0.03}]$  composite exhibited a much higher electrical conductivity of 790 S cm<sup>-1</sup> (**Figure 13 A**), although the in-plane Seebeck coefficient of  $\text{TiS}_2$  decreased to -78  $\mu\text{V K}^{-1}$  from -171  $\mu\text{V K}^{-1}$  after intercalation of the hexylammonium ions (**Figure 13 B**). Moreover, due to the significant reduction in thermal conductivity of  $\text{TiS}_2/[(\text{HA})_{0.08}(\text{H}_2\text{O})_{0.22}(\text{DMSO})_{0.03}]$  (0.12 ± 0.03 W m<sup>-1</sup> K<sup>-1</sup>) as compared to bulk  $\text{TiS}_2$  crystal (4.2 W m<sup>-1</sup> K<sup>-1</sup>) (**Figure 13 C**), an excellent thermoelectric figure of merit (*ZT*) of 0.28 at 373 K can be achieved (**Figure 13D**). As a result, a power factor of 0.45 mW m<sup>-1</sup> K<sup>-2</sup> can be obtained on this  $\text{TiS}_2/[(\text{HA})_{0.08}(\text{H}_2\text{O})_{0.22}(\text{DMSO})_{0.03}]$  based thermoelectric device. Theoretical calculation result revealed that the intercalated organic hexylammonium molecules and the resulting wavy structure between the neighbouring layers played important roles on increasing the phonon scattering rate inside the  $\text{TiS}_2/[(\text{HA})_{0.08}(\text{H}_2\text{O})_{0.22}(\text{DMSO})_{0.03}]$  hybrid structure, resulting in the reduction of thermal conductivity. In addition, the hybrid also showed impressive flexibility with a flexural modulus of ~145 MPa at 300 K, which was comparable to a typical plastic material such as Teflon. Moreover, the same group reported that  $\text{TiS}_2$ /Hexylamine film prepared by an exfoliation-and-reassembly method was also promising for the thermoelectric application.<sup>204</sup> Generally, an electrical conductivity of ~660 S cm<sup>-1</sup> and a Seebeck coefficient of around -55  $\mu\text{V K}^{-1}$  could be obtained on the  $\text{TiS}_2$ /hexylamine hybrid film after annealing. Notably, the highest power factor achieved on the prepared hybrid film was 0.21 mW m<sup>-1</sup> K<sup>-2</sup> at room temperature. The measured in-plane thermal conductivity was around 4.2 W m<sup>-1</sup> K<sup>-1</sup>, leading to an in-

plane  $ZT$  of around ~0.17. Importantly, at a temperature gradient of 70 K, a voltage output of 33 mV with a maximum power density of  $2.5 \text{ W m}^{-2}$  was recorded on a fabricated prototype thermoelectric device, further revealing the great potential to power the future wearable electronic device. As another example, Huang and coworkers showed that metallic 1T-MoS<sub>2</sub> nanosheets were also promising for thermoelectric application.<sup>203</sup> Owing to the metallic nature of the 1T phase, the 1T-MoS<sub>2</sub> nanosheets showed a high conductivity of around 9978.3 S/m, a power factor of  $73.1 \mu\text{W m}^{-1} \text{ K}^{-2}$  and a Seebeck coefficient of  $+85.6 \mu\text{V K}^{-1}$  at room temperature, which indicated their hole-transport nature and far better than those of the 2H-MoS<sub>2</sub> single crystals. More importantly, further controlled temperature annealing test proved that the ideal working temperature of the thermoelectric film based on the 1T-MoS<sub>2</sub> nanosheets was around 100 °C, showing a slightly decreased power factor of  $58.3 \mu\text{W m}^{-1} \text{ K}^{-2}$ , which met the requirement for wearable electronic devices.

### 3.3 Catalysis

As known, catalytic activity is highly dependent on the chemical composition, surface functionality, and intrinsic electronic structure of the catalyst.<sup>63,206,225-230</sup> Owing to the various chemical compositions, tunable surface properties, unique electronic structures, low production cost and earth abundance, 2D TMD nanosheets have attracted intensive research interest for catalytic applications, including HER,<sup>25,63,152,206</sup> photocatalysis<sup>35,183,205,229,230</sup> and CO<sub>2</sub> reduction.<sup>228</sup> For example, Geng and coworkers found that the metallic 1T-MoS<sub>2</sub> synthesized by colloidal method was promising for electrocatalytic HER.<sup>25</sup> A low overpotential of 175 mV at current density of  $10 \text{ mA cm}^{-2}$ ,

and a Tafel slope of 41 mV decade<sup>-1</sup> were readily realized on the prepared metallic 1T-MoS<sub>2</sub> in 0.5 M H<sub>2</sub>SO<sub>4</sub> electrolyte, with a good stability, i.e. only 12% decay in activity after 1000 cycles of continuous test. It was believed that the enhanced HER activity was attributed to the decreased charge transfer resistance originated from the metallic conductive nature of the 1T phase. Notably, the phase of synthesized metallic 1T-MoS<sub>2</sub> could be stabilized in solution at ambient conditions for even 90 days, which was promising for practical applications. Moreover, Yin and coworkers demonstrated that by engineering the crystal phase, sulfur vacancy and edge of MoS<sub>2</sub>, the HER activity of the porous 1T-MoS<sub>2</sub> nanosheets was superior to that of 2H-MoS<sub>2</sub> and non-porous 1T-MoS<sub>2</sub> nanosheets.<sup>152</sup> Due to the synergistic effect of crystal phase, S-vacancies, and edges, the prepared porous 1T-MoS<sub>2</sub> nanosheets exhibited high HER activity with the overpotential of 153 mV (versus reversible hydrogen electrode (RHE)) at current density of 10 mA cm<sup>-2</sup>, a Tafel slope of 43 mV decade<sup>-1</sup> and a higher electrochemically active surface area (**Figure 14A, B**). The long-time stability of the porous 1T-MoS<sub>2</sub> nanosheets was evaluated by 1000 continuous testing cycles for 20000 s, showing negligible deterioration of activity after the test. As another example, the exfoliated TaS<sub>2</sub> nanosheets with atomic-sized pores induced by post oxygen plasma treatment also showed enhanced HER activity in 0.5 M H<sub>2</sub>SO<sub>4</sub> electrolyte with a very low catalyst loading of 0.24 mg cm<sup>-2</sup>.<sup>74</sup> Specifically, the exfoliated TaS<sub>2</sub> nanosheets with 10 min oxygen plasma treatment showed the best HER performance with an onset-potential of 200 mV, an overpotential of 564 mV at the current density of 10 mA cm<sup>-2</sup> and a Tafel slope of 135 mV decade<sup>-1</sup>, which were far better than those of the exfoliated pristine TaS<sub>2</sub> nanosheets. DFT calculations revealed that the under-coordinated edge S atoms around the fabricated

atomically sized pore were the active sites for HER. Note that the way used for engineering pores of the exfoliated 2D nanosheets was also applicable for other TMD nanomaterials, leading to a new general method for invention of TMD based catalysts for HER with enhanced catalytic activity. Moreover, Gao and coworkers reported that the lithiation of vertically grown 1T'-ReS<sub>2</sub> nanosheets could enhance the HER activity in 0.5 M H<sub>2</sub>SO<sub>4</sub> electrolyte with a small onset-potential of around 100 mV, a Tafel slope of 84 mV decade<sup>-1</sup> and an exchanged current density of around 67.6 μA cm<sup>-2</sup>.<sup>128</sup> However, the HER performance decreased by ~15% after 1000 cycles stability test. Besides the binary TMD nanomaterials, some multinary TMD nanosheets also showed great potential for HER application. For example, Yang and coworkers demonstrated that layered MoS<sub>2(1-x)Se<sub>2x</sub></sub> ( $x=0.39, 0.51, 0.61$ ) nanosheets showed enhanced catalytic activity for HER compared to that of MoS<sub>2</sub> and MoSe<sub>2</sub> nanosheets.<sup>231</sup> In general, the overpotentials at current density of 10 mA cm<sup>-2</sup> were measured to be 300 mV, 273 mV and 279 mV for MoS<sub>2(1-x)Se<sub>2x</sub></sub> ( $x=0.39, 0.51, 0.61$ ) nanosheets, respectively, while the corresponding Tafel slopes were 100 mV decade<sup>-1</sup>, 119 mV decade<sup>-1</sup> and 106 mV decade<sup>-1</sup>, respectively. The stability of the MoS<sub>2(1-x)Se<sub>2x</sub></sub> ( $x=0.61$ ) nanosheets was evaluated by the continuous test at a constant potential of -0.24 V vs RHE for 22 h, showing only slight degradation of the current density. As another example, Huang and the coworkers showed that SnO<sub>2</sub>-MoSe<sub>2</sub> hybrid nanostructure with the few-layer MoSe<sub>2</sub> grown on both inner and outer surfaces of SnO<sub>2</sub> nanotube exhibited excellent activity toward HER.<sup>232</sup> A small onset-potential of around 110 mV, a low overpotential of 174 mV at current density of 10 mA cm<sup>-2</sup> and a small Tafel slope of 51 mV decade<sup>-1</sup> were obtained on the prepared catalyst. The current density was slightly decayed after 3000 cycles of cyclic voltammetry (CV)

test from -0.4 V to 0.2 V (vs RHE). It was concluded that the open structure and larger surface area of the hybrid structure played important role on reduction of the charge transfer resistance, resulting in the enhancement of HER activity. Moreover, Ma and coworkers reported that the 2D MoS<sub>2</sub> inlaid nanosheets grown on graphene were highly active for HER, presenting a small onset potential of around 30 mV, an overpotential of around 110 mV at current density of 10 mA cm<sup>-2</sup> and a small Tafel slope of 67.4 mV decade<sup>-1</sup>.<sup>233</sup> The HER performance of this catalyst remained stable after 100000 s continuous testing under static overpotential of -0.15 V, showing great stability with almost unchanged activity. The huge number of exposed active sites, enhanced charge transfer induced by the conductive nature of graphene and strong bonding between MoS<sub>2</sub> and graphene were considered as the most important reasons for the high HER activity and stability of this catalyst.

In addition, some ultrathin TMD nanosheets also exhibited potential in photocatalytic application.<sup>35,183,229</sup> For instance, Yu and coworkers demonstrated that the solution-processed 2D WSe<sub>2</sub> film with a thickness of 25 nm showed a sustained *p*-type photocurrent under standard light illumination (1 sun, 100 mW cm<sup>-2</sup>).<sup>234</sup> After the 2D WSe<sub>2</sub> film was functionalized with Pt catalyst, a hydrogen evolution photocurrent around 1.0 mA cm<sup>-2</sup> was obtained. Moreover, a WS<sub>2</sub>-WO<sub>3</sub>·H<sub>2</sub>O heterostructure prepared by partially oxidizing the 2H-WS<sub>2</sub> nanosheet also showed great photocatalytic activity toward the decomposition of methyl orange (MO) under visible-light irradiation.<sup>235</sup> More than 90% MO was degraded after the test, indicating the great efficiency of WS<sub>2</sub>-WO<sub>3</sub>·H<sub>2</sub>O heterostructure used as the photocatalyst, which was further confirmed by the measured photocurrent response of  $6 \times 10^{-5}$  A cm<sup>-2</sup> under visible light irradiation. It was

believed that the well-aligned band structure between  $\text{WS}_2$  and  $\text{WO}_3 \cdot \text{H}_2\text{O}$  was crucial for the efficient photogenerated charge separation, resulting in the good photocatalytic activity. Furthermore, Yang and coworkers reported a series of photocatalysts based on TMD heterostructures of  $\text{MoSe}_2$  nanosheets and  $\text{ZnInS}_4/\text{CdInS}_4/\text{In}_2\text{S}_3$  toward the efficient visible-light-driven hydrogen evolution.<sup>236</sup> The photocatalytic  $\text{H}_2$  evolution performance of  $\text{ZnInS}_4/1\%\text{MoSe}_2$  heterostructure was evaluated under the visible light irradiation ( $\lambda > 400$  nm) using lactic acid as hole scavenger, giving rise to a highest  $\text{H}_2$  evolution rate of  $\sim 6454 \mu\text{mol g}^{-1} \text{ h}^{-1}$ , which was  $\sim 15$  and 4 times as high as that of single layer  $\text{ZnInS}_4$  and pristine  $\text{ZnInS}_4$  crystal, respectively. This result also surpassed the performance obtained on  $\text{ZnIn}_2\text{S}_4/1\%\text{Pt}$  ( $4353 \mu\text{mol g}^{-1} \text{ h}^{-1}$ ) and  $\text{ZnIn}_2\text{S}_4/1\%\text{MoS}_2$  ( $3860 \mu\text{mol g}^{-1} \text{ h}^{-1}$ ), further revealing the superior activity of the  $\text{ZnInS}_4/1\%\text{MoSe}_2$  heterostructure (**Figure 14C**). The photocatalytic  $\text{H}_2$  evolution test of  $\text{CdInS}_4/1\%\text{MoSe}_2$  and  $\text{In}_2\text{S}_3/1\%\text{MoSe}_2$  also exhibited the similar enhancement compared to that of their bare single-layer and bulk counterparts. Notably, the photocatalytic activity of  $\text{ZnInS}_4/1\%\text{MoSe}_2$  showed negligible degradation after 20 consecutive cycles, indicating its great stability (**Figure 14D**).

In addition to the promising application in hydrogen evolution reaction, recent studies also revealed the potential of TMD nanosheets in  $\text{CO}_2$  reduction.<sup>228</sup> For example, Asadi and coworkers found that  $\text{WSe}_2$  nanoflakes showed great electrochemical activity for conversion of  $\text{CO}_2$  to  $\text{CO}$  in an ionic liquid electrolyte, with 50 volume percent (vol%) EMIM- $\text{BF}_4^-$  and 50 vol % deionized water.<sup>228</sup> Importantly, a high current density of  $18.95 \text{ mA cm}^{-2}$  (**Figure 14E**), CO faradaic efficiency of 24% and CO formation turnover frequency of 0.28 per second (**Figure 14F**) were obtained at a low overpotential of 54 mV, which were far better than those of previously reported Ag nanoparticles (NPs) and

bulk MoS<sub>2</sub>. Further theoretical calculations proved that the metallic edge of the WSe<sub>2</sub> nanoflakes was more active than that of Ag NPs for the formation of the intermediate COOH\* species, which played an important role during the reaction of electrochemical reduction of CO<sub>2</sub>. In addition, the lowest work function of WSe<sub>2</sub> nanoflakes, compared to MoS<sub>2</sub>, WS<sub>2</sub> and MoSe<sub>2</sub>, also made themselves the best TMD-based catalyst for CO<sub>2</sub> activation in electrochemical reduction reaction.

### 3.4 Energy storage and conversion

Owing to the low production cost, tunable chemical compositions and functionalities, TMD nanosheets are also promising for energy storage and conversion applications, such as supercapacitors and lithium ion batteries (LIBs).<sup>116,128,208-211</sup> For example, Acerce and coworkers demonstrated that metallic 1T-MoS<sub>2</sub> was a promising candidate for fabrication of high-performance supercapacitor.<sup>116</sup> Compared with 2H-MoS<sub>2</sub>, the electrode based on the restacked 1T-MoS<sub>2</sub> film exhibited rectangular CV shapes when tested in 0.5 M H<sub>2</sub>SO<sub>4</sub>, Li<sub>2</sub>SO<sub>4</sub>, Na<sub>2</sub>SO<sub>4</sub> and K<sub>2</sub>SO<sub>4</sub> electrolytes with the potentials ranging from -0.15 V to 0.85 V versus NHE, indicating the much larger specific gravimetric capacitance of the 1T phase electrode (**Figure 15A**). Importantly, the capacitance of the 1T phase electrode retained at a very high value even at a very high scan rates of over 200 mV s<sup>-1</sup>, and an exceptionally high volumetric capacitance ranging from 400 to 650 F cm<sup>-3</sup> was obtained at scan rate of 20 mV s<sup>-1</sup> (**Figure 15B**). After performing 5000 charge/discharge cycles at a current density of 2 A g<sup>-1</sup>, the capacitive retention of the 1T phase electrode still kept at high values, i.e. 93% in neutral electrolytes and 97% in acidic electrolytes, indicating the great stability and high efficiency of the 1T-MoS<sub>2</sub> based supercapacitor. The

electrochemical storage performance of the 1T electrode was also evaluated in non-aqueous electrolytes, including tetraethylammonium tetrafluoroborate (TEA BF<sub>4</sub>)/MeCN and 1-ethyl-3-methylimidazolium tetrafluoroborate (EMIM BF<sub>4</sub>)/MeCN organic electrolytes, showing high capacitance of 199 F cm<sup>-3</sup> in TEA BF<sub>4</sub>/MeCN and 250 F cm<sup>-3</sup> in EMIMBF<sub>4</sub>/MeCN. The capacitive retention could be as high as over 90% even after 5000 cycles (**Figure 15C**). More importantly, high energy density of 0.11 Wh cm<sup>-3</sup> and power density of 1.1 W cm<sup>-3</sup> were obtained at a current density of 0.5 A g<sup>-1</sup>, and 0.051 Wh cm<sup>-3</sup> and 51 W cm<sup>-3</sup> were obtained at the current density of 32 A g<sup>-1</sup>. As another example, Hu and coworkers demonstrated that the highly conductive hydrogenated-Cu<sub>2</sub>WS<sub>4</sub> nanosheet could be used as electrode material for fabrication of all-solid-state supercapacitor, exhibiting specific capacitance of 583.3 F cm<sup>-3</sup> and 314.1 F cm<sup>-3</sup> at current density of 0.31 A cm<sup>-3</sup> and 1.25 A cm<sup>-3</sup>, respectively.<sup>237</sup> An energy density of 0.029 Wh cm<sup>-3</sup> was achieved at a current density of 0.31 A cm<sup>-3</sup>, resulting in a power density of 0.187 W cm<sup>-3</sup>. While at a current density of 1.25 A cm<sup>-3</sup>, the measured energy and power density were as high as 0.016 Wh cm<sup>-3</sup> and 0.75 W cm<sup>-3</sup>, respectively. In addition, Geng and coworkers demonstrated another example by using metallic phase multilayer MoS<sub>2</sub> as electrode material for supercapacitor.<sup>238</sup> The electrochemical storage performance of the metallic MoS<sub>2</sub> electrode was tested in 1 M Li<sub>2</sub>SO<sub>4</sub> electrolyte, showing maximum specific capacitance of 380 and 105 F g<sup>-1</sup> at the scan rates of 5 and 10000 mV s<sup>-1</sup>, respectively. Importantly, an assembled symmetric supercapacitor cell based on the metallic MoS<sub>2</sub> could deliver a specific capacitance of 249 F g<sup>-1</sup> at scan rate of 50 mV s<sup>-1</sup> as well as a high capacity retention of 150 F g<sup>-1</sup> (up to 88%) even after 10000 cycle test, showing great cyclic performance. Moreover, Liu and coworkers

showed that ultrathin 1T'-MoTe<sub>2</sub> nanosheets synthesized by colloidal method were also promising for supercapacitor application.<sup>239</sup> The electrochemical storage properties of the 1T'-MoTe<sub>2</sub> nanosheet based electrodes were tested in 2 M KOH solution using a common three-electrode cell, showing pseudocapacitance behavior. The galvanostatic charge-discharge tests at voltage range of 0-0.56 V (versus Hg/HgO) showed a high specific capacitance of 1393 F g<sup>-1</sup> and 714 F g<sup>-1</sup> at current density of 1 A g<sup>-1</sup> and 100 A g<sup>-1</sup>, respectively. The capacitance retention after 1000 cycles at current density of 50 A g<sup>-1</sup> and 100 A g<sup>-1</sup> could reach 98% and 87%, respectively, further confirming the great cycling stability of the 1T'-MoTe<sub>2</sub> nanosheet electrodes. Notably, a high specific capacitance of 158.7 F g<sup>-1</sup> could be obtained at the current density of 1 A g<sup>-1</sup> in a fabricated asymmetric supercapacitor composed of 1T'-MoTe<sub>2</sub> and active carbon, delivering a high energy density of 56.4 Wh kg<sup>-1</sup> and 28.2 Wh kg<sup>-1</sup> at power density of 800 W kg<sup>-1</sup> and 16 W kg<sup>-1</sup>, respectively.

Besides the application in supercapacitors, some 2D TMD nanosheets are also considered as electrode materials for LIBs and sodium ion batteries (SIBs).<sup>128, 208-211</sup> For instance, Huang and coworkers showed that free-standing 2D SnS<sub>2</sub> nanosheets grown on 3D graphene foam (SnS<sub>2</sub>/3DG) could deliver a high reversible capacity of 771.2 and 174.1 mAh g<sup>-1</sup> at the current density of 200 and 2000 mA g<sup>-1</sup>, respectively.<sup>209</sup> It is noteworthy that, even after 50 charge/discharge cycles at a high current density of 1000 mA g<sup>-1</sup>, the SnS<sub>2</sub>/3DG based LIB still delivered a discharge capacity of 451.2 mAh g<sup>-1</sup> with a capacity retention of 99%, which was superior to that of commercial graphite anode (~372 mAh g<sup>-1</sup>), indicating its great cycling stability. Moreover, the [001] preferentially-oriented 2D WS<sub>2</sub> nanosheet also showed good performance in LIBs.<sup>210</sup> Generally, a

reversible capacity of 539.1 mAh g<sup>-1</sup> after 60 cycles could be obtained at a current density of 200 mA g<sup>-1</sup>, while a high capacity retention of 193.7 mAh g<sup>-1</sup> could still remain over 1000 cycles at a high current density of 1000 mA g<sup>-1</sup>. The rate performance of the WS<sub>2</sub> nanosheet electrode was evaluated at varying current densities at 0.1, 0.2, 0.4, 0.8 and 1.6 A g<sup>-1</sup>, showing good reversible capacity of 634.2, 552, 484.6, 410.9, and 321 mAh g<sup>-1</sup>, respectively. Notably, after switching to the current density of 0.1 A g<sup>-1</sup>, a good capacity retention of 541.7 mAh g<sup>-1</sup> was obtained, indicating the good structural stability and rate performance of the WS<sub>2</sub> nanosheet electrode. In addition, Liu and coworkers showed that few-layer MoS<sub>2</sub> nanosheets grown on MoO<sub>3</sub> nanowires could be a high-performance electrode material for LIB.<sup>211</sup> The MoS<sub>2</sub>-MoO<sub>3</sub> hybrid electrode exhibited high specific capacity of 1510 and 1362 mAh g<sup>-1</sup> at the current density of 100 mA g<sup>-1</sup> in the initial discharge and charge process, respectively, leading to a high Columbic efficiency of 90.2%, which was superior to that of pure MoO<sub>3</sub> nanowire. In addition, a high reversible capacity of 781 mAh g<sup>-1</sup> at a current density of 100 mA g<sup>-1</sup> could be retained after 100 cycles. It was concluded that the unique structure of the MoS<sub>2</sub>-MoO<sub>3</sub> hybrid with apparent porous surface and large number of exposed edges for the accommodation of more Li<sup>+</sup> insertion greatly contributed to the enhanced capacity. Moreover, recent studies also revealed the possibility of using TMD nanomaterials for Li-S battery. As an example, Babu and coworkers reported that WS<sub>2</sub> nanosheet based electrode could deliver a stable specific capacity of 590 mAh g<sup>-1</sup> at 0.5 C rate, with an excellent Coulombic efficiency of 99% over 350 discharge-charge cycles.<sup>240</sup> As another example, Gao and coworkers demonstrated that the vertically grown 1T'-ReS<sub>2</sub> nanosheets could also be used as electrode material in Li-S battery, due to the higher efficiency of adsorbing and

trapping polysulfide than that of conventional carbon-based materials.<sup>128</sup> The ReS<sub>2</sub> nanosheet electrode exhibited high capacity and rate capability with the discharge capacities of ~1100, 960, 903, 876, 787, and 732 mAh g<sup>-1</sup> at the current density of 0.2, 0.5, 0.8, 1, 2, and 3 C, respectively. A high specific capacity of over 750 mAh g<sup>-1</sup> could be retained at the current density of 0.5 C after 300 cycles with only ~0.063% decay per cycle, which was much better than that of the carbon nanofiber membrane electrode. Moreover, the ultrathin TMD nanosheets were also considered as electrode material for SIBs. For example, Bang and coworkers showed that the liquid exfoliated MoS<sub>2</sub> nanosheets and MoS<sub>2</sub>-rGO composite were promising anode materials for SIBs.<sup>212</sup> At the 50<sup>th</sup> discharge/charge cycle, the MoS<sub>2</sub> nanosheet based SIB exhibited good sodiation and desodiation capacities of 165 and 161 mAh g<sup>-1</sup> at the current density of 20 mA g<sup>-1</sup>, corresponding to a Coulombic efficiency of 97%. Compared to the pristine MoS<sub>2</sub> powder, the MoS<sub>2</sub> nanosheet electrode exhibited better rate performance with a higher capacity at a high current density of 400 and 800 mA g<sup>-1</sup>. Notably, when hybridizing with rGO in a mass ratio of 1:1 to form the composite, the MoS<sub>2</sub>-rGO electrode could deliver a much higher first discharge capacity of 376 mAh g<sup>-1</sup> than the pure MoS<sub>2</sub> nanosheet. In addition, Sun and coworkers reported another SnS<sub>2</sub> nanosheet based anode electrode for SIBs, showing high apparent diffusion coefficient of Na<sup>+</sup> and fast sodiation/desodiation reaction kinetics.<sup>241</sup> Specifically, the SnS<sub>2</sub> nanosheets synthesized at 160 °C exhibited the highest reversible capacity of 733 and 435 mAh g<sup>-1</sup> at a current density of 0.1 and 2 A g<sup>-1</sup>, respectively. The cycling durability of the SnS<sub>2</sub> nanosheet electrode was tested by performing 50 discharge/charge cycles at a current density of 0.1 A g<sup>-1</sup>, showing a high capacity of 647 mAh g<sup>-1</sup> at the 50<sup>th</sup> cycle (**Figure 15D**).<sup>241</sup> During the rate performance

test, the charge capacity of the SnS<sub>2</sub> nanosheet based electrode retained the value of 710 mAh g<sup>-1</sup>, when the current density was switched to 0.1 A g<sup>-1</sup>. Notably, a reversible capacity of 375 mAh g<sup>-1</sup> at current density of 0.1 A g<sup>-1</sup> with a Coulombic efficiency of 67% could be obtained on a full SIB cell consisting of SnS<sub>2</sub> nanosheet anode and Na<sub>3</sub>V<sub>2</sub>(PO<sub>4</sub>)<sub>3</sub> cathode, further proving the potential of SnS<sub>2</sub> nanosheet for SIBs.

### 3.5 Biomedical application

The growing demand for low cost, high efficiency and precise accuracy of clinical biomedicine and the fast development of nanotechnology have urgently required the invention of novel theranostic nanoagents, which can target the disease with high precision and eliminate it with high efficiency.<sup>214</sup> Among all the newly developed biocompatible nanoagents, photothermal theranostic nanoagents have attracted huge research interest mainly because of the simple requirement of light, which is the only required energy source to generate the local heat for the elimination of infected cells, like cancer cells.<sup>214</sup> Due to their unique structures and physicochemical properties, biocompatible ultrathin 2D nanosheets have emerged as a new unique family of photothermal therapy nanoagents with unprecedented advantages and superior performances in biomedicines.<sup>214</sup> Because the heat and charge transportation are usually confined in their 2D plane, these biocompatible 2D nanomaterials demonstrate extraordinary performance when used as photothermal agent. For example, Qian and coworkers demonstrated that TiS<sub>2</sub> nanosheets modified with polyethylene glycol (PEG) (TiS<sub>2</sub>-PEG), which showed an extinction coefficient of 26.8 L g<sup>-1</sup> at 808 nm wavelength, was effective for photothermal cancer therapy.<sup>213</sup> Generally, under the irradiation of 808

nm NIR laser with the power density of  $0.8 \text{ W cm}^{-2}$ , the  $\text{TiS}_2$ -PEG exhibited an obvious and stable concentration-dependent temperature increase behavior, with a low cytotoxicity (**Figure 16A**). The photothermal effectiveness of  $\text{TiS}_2$ -PEG was confirmed by testing the livability of the 4T1 cells incubated with varying concentrations of  $\text{TiS}_2$ -PEG for 6 h under the irradiation of 808 nm laser. The cells were eliminated after being incubated with  $0.1 \text{ mg mL}^{-1}$   $\text{TiS}_2$ -PEG under 5 min 808 nm laser irradiation (**Figure 16B**). The in-vivo test further showed that the tumors on the experiment mice injected with a  $\text{TiS}_2$ -PEG solution ( $2 \text{ mg mL}^{-1}$ ,  $200 \mu\text{l}$ ) were completely ablated without re-growth after being exposed to 808 nm laser at a power density of  $0.8 \text{ W cm}^{-2}$ , due to the increased temperate up to  $\sim 65^\circ\text{C}$  within 5 min. Moreover, Zhu and coworkers demonstrated that ultrathin ternary  $\text{Ta}_2\text{NiS}_5$  modified with an amphiphilic triblock copolymer (PEG-b-PPG-b-PEG) ( $\text{Ta}_2\text{NiS}_5$ -P) was also a promising photothermal nanoagent for cancer therapy.<sup>242</sup> A high photothermal conversion efficiency of 35% was recorded for the  $\text{Ta}_2\text{NiS}_5$ -P due to its high absorption toward light at wavelength of 500, 755 and 845 nm. Compared to PEGylated rGO (GO-P), the  $\text{Ta}_2\text{NiS}_5$ -P solution with the concentration of  $0.2 \text{ mg mL}^{-1}$  exhibited a much higher increase in temperature under the irradiation of 808 nm laser at the power density of  $1.0 \text{ W cm}^{-2}$ , reaching  $72^\circ\text{C}$  within 8 min. The photothermal efficacy of  $\text{Ta}_2\text{NiS}_5$ -P for ablation of cancer cells was tested by exposing the HeLa cells incubated with  $\text{Ta}_2\text{NiS}_5$ -P ( $0.1 \text{ mg mL}^{-1}$ ) to a  $1.0 \text{ W cm}^{-2}$  808 nm laser for 8 min, showing a 90% elimination rate after irradiation. Furthermore, the in-vivo test on the xenograft 4T1 tumor mouse injected with  $\text{Ta}_2\text{NiS}_5$ -P showed that the tumor growth was effectively inhibited after the irradiation of 808 nm laser with the power density of  $0.5 \text{ W cm}^{-2}$  for 5 min, due to the dramatically increased temperature in the irradiated area. In addition, our group showed that

solution-processed ultrathin 2D metal oxide/sulfide hybrid nanosheets, i.e.,  $Ti_xTa_{1-x}S_yO_z$  ( $x=0.71, 0.49$ , and  $0.30$ ), with a large extinction coefficient of  $54.1\text{ Lg}^{-1}\text{cm}^{-1}$  at  $808\text{ nm}$ , was also highly effective for photothermal therapy.<sup>243</sup> Owing to the strong absorbance in the NIR region, the  $Ti_{0.71}Ta_{0.29}S_yO_z$  nanosheets modified with polyethylene glycol (LA-PEG) exhibited a high photothermal conversion efficiency of  $39.2\%$ , with the solution temperature increased by  $34.4\text{ }^{\circ}\text{C}$  after  $10\text{ min}$  irradiation with a  $808\text{ nm}$  laser at the power density of  $1.0\text{ W cm}^{-2}$  (**Figure 16C**). Notably, low viabilities of HeLa cells incubated with  $20$  and  $50\text{ ppm}$  LA-PEG-modified  $Ti_{0.71}Ta_{0.29}S_yO_z$  nanosheets were obtained by irradiating the cancer cells with  $808\text{ nm}$  laser, further revealing the high efficacy of  $Ti_{0.71}Ta_{0.29}S_yO_z$  nanosheets as photothermal agent (**Figure 16D**).

### 3.6 Other promising applications

In addition to the aforementioned applications, some other promising ones by utilization of the 2D TMD nanosheets with the unique 2D feature and physiochemical properties are reported in recent years. For example, Feng and coworkers demonstrated that porous  $MoS_2$  nanosheets with the typical diameter in the range of  $2\text{-}25\text{ nm}$  could serve as nanopower generators by harvesting osmotic energy in a salt solution, such as potassium chloride (KCl).<sup>60</sup> In principle, the ion flux, driven by the chemical potential through the pore, is screened by the negatively charged pore, leading to form the diffusion current composed of mostly positively charged ions (**Figure 17A, B**). The generated osmotic current could be modulated by changing the surface charge density, which was highly dependent on the pore sizes, the salt concentrations and the pH values of the electrolytes. For instance, surface charges of  $-0.024$ ,  $-0.053$ , and  $-0.088\text{ C m}^{-2}$  could be obtained at pH

5 from pore sizes of 2, 6, and 25 nm, respectively. Impressively, it was estimated that a power density of  $106 \text{ W m}^{-2}$  could be reached in a single-layer MoS<sub>2</sub> membrane with a homogeneous pore size of 10 nm and porosity of 30% with a KCl salt gradient. Such a considerable energy output could be a highly efficient nanopower source for a self-powered nanosystem, such as MoS<sub>2</sub> FETs (**Figure 17C, D**). Notably, by varying the top gate voltage in a range of -0.78 to 0.78 V, the channel conductivity could be modulated by a factor of 50 to 80 (**Figure 17E**). By fixing the gate voltage and varying the drain-source voltage, a linear  $I_{ds}-V_{ds}$  curve can be obtained, revealing the efficient injection of electrons into the transistor channel (**Figure 17E**). As another example, Acerce and coworkers showed that metallic 1T-MoS<sub>2</sub> based electrode could be exploited as high-performance electrochemical actuator due to the highly conductive nature of 1T phase and the high ionic diffusivity in the restacked 1T-MoS<sub>2</sub> nanosheets (**Figure 18A**).<sup>244</sup> The actuation behavior of the device composed of the Kapton beam coated with 1T-MoS<sub>2</sub> nanosheet film was tested in a 0.5 M H<sub>2</sub>SO<sub>4</sub> electrolyte, which could be controlled by the applied potential and the scan rate, showing a reversible bending behavior even at high frequency (**Figure 18B, C**). Notably, a prototype based on metallic 1T-MoS<sub>2</sub> nanosheet electrode, i.e., inverted-series-connected (ISC) bimorph actuation device, was prepared to further reveal the potential in real application. An energy density of  $6 \text{ kJ m}^{-3}$  could be obtained on the ISC bimorph actuator by considering the gravitational, buoyancy, spring and friction forces (**Figure 18D**). Amazingly, the 1T-MoS<sub>2</sub> actuator was able to lift more than 150 times its own weight, with a highly stable actuation behavior over hundreds of tested cycles (**Figure 18E, F**).

#### **4. Outlook and perspective**

Great progress has been made in the exploration of new structured 2D TMD nanosheets.

In this review, we have introduced the latest research progress on the synthesis, characterizations and applications of emerging ultrathin TMD nanosheets with new structures. Six subtypes of TMD nanosheets (as shown in Figure 1), including vacancy-containing TMD nanosheets (subtype 1), heteroatom-doped TMD nanosheets (subtype 2), alloyed TMD nanosheets (subtype 3), phase-based TMD new structures (subtype 4), TMD heterostructures (subtype 5), and Janus TMD nanosheets (subtype 6) have been summarized. A broad range of techniques, such as ADF-STEM, Raman, AFM, XPS, and XAFS have been employed to characterize the sizes, thicknesses, compositions, crystal phases, interfaces, and atom arrangements of these materials. Furthermore, these new-structured TMD nanosheets are promising for a number of applications, including electronics/optoelectronics, thermoelectrics, catalysis, energy storage and conversion, and biomedicine, etc.

The research on the new structured TMD nanosheets is still at its infant stage, and there are still many challenges and opportunities in this promising research field. First, for the vacancy-containing TMD nanosheets (subtype 1) and heteroatom-doped TMD nanosheets (subtype 2), the vacancies and heteroatoms are usually randomly distributed in the TMD nanosheets. It remains a challenge to precisely control the anchored position and desirable concentration of vacancies and heteroatoms at atomic level. Therefore, the development of novel approaches is urgently required to effectively control and/or engineer the vacancies and heteroatoms with atomic accuracy in TMD nanosheets. Second, for the alloyed TMD nanosheets (subtype 3), it was recently reported that the

crystal phases of some specific alloys, such as  $\text{WSe}_{2(1-x)}\text{Te}_{2x}$ <sup>109</sup> and  $\text{Mo}_{1-x}\text{W}_x\text{Te}_2$ <sup>111,112</sup>, can be tuned by controlling the alloying ratio, showing tunable physicochemical properties. However, such kind of composition-dependent phase change was only realized in limited compounds. How to extend this strategy to other alloyed TMD nanosheets is critically important in this research filed. Third, to form phase-based TMD new structures (subtype 4), the crystal phase engineering of TMDs is critically important. Although current methods, such as alkali metal intercalation, electron beam irradiation, and strain engineering, are widely used to change the phase of TMDs, it is still difficult to produce the pure metastable phase, such as 1T or 1T', with unique properties.<sup>43</sup> Specifically, the preparation of single-layer metastable 1T- or 1T'-TMD compounds is challenging, due to their low stability.<sup>43</sup> Therefore, the development of a feasible and general method is urgently required to prepare the high phase-purity metastable phase TMD nanosheets. Forth, for TMD heterostructures (subtype 5), most of TMD heterostructures have been synthesized through the CVD method, which lacks scalability and requires harsh experimental conditions (e.g., high temperature and high vacuum).<sup>1,31</sup> As known, solution-based synthetic methods allow the production of 2D nanomaterials in large scale. Therefore, more efforts can be devoted to the preparation of TMD heterostructures via solution-based methods. One possible strategy to prepare the epitaxial TMD heterostructures in solution is through the template/seed growth. As an example, our group has reported the solution-based epitaxial growth of CuS, ZnS and  $\text{Ni}_3\text{S}_2$  nanoplates on  $\text{TiS}_2$  nanosheet templates to form heterostructures, which is a promising strategy for preparation of 2D vertical heterostructure in solution.<sup>245</sup> Last but not least, although many new TMD nanosheets with novel structures, including the Janus TMD nanosheet

(subtype 6), have been theoretically predicted,<sup>246-248</sup> most of these new structures have not been realized experimentally. Therefore, rational design and synthesis of these new structured TMD nanosheets with more unique properties are an attractive research direction, although it still remains big challenge.

Further research efforts are also required for the applications of the TMD nanosheets. Although a wide range of promising applications have been demonstrated, the mechanism for the novel structured TMD nanosheets to enhance the performance is still not clear. A fundamental understanding on the relationship between the structural characteristics and performance in various applications is of great importance for the rational design and controlled synthesis of novel TMD nanosheets with atomic accuracy. Moreover, many newly emerged promising applications, such as the osmotic power source<sup>60</sup> and electrochemical actuator,<sup>244</sup> have been developed by utilization of the unique structures and crystal phases of TMD nanosheets. Therefore, the exploration of new applications based on the structural characteristics and unique properties of TMD nanosheets is also an interesting and promising research direction.

**Acknowledgement:**

This work was supported by MOE under AcRF Tier 2 (ARC 19/15, No. MOE2014-T2-2-093; MOE2015-T2-2-057; MOE2016-T2-2-103; MOE2017-T2-1-162) and AcRF Tier 1 (2016-T1-001-147; 2016-T1-002-051; 2017-T1-001-150), and NTU under Start-Up Grant (M4081296.070.500000) in Singapore. This research is supported by the National Research Foundation, Prime Minister's Office, Singapore under its Campus for Research Excellence and Technological Enterprise (CREATE) programme. We would like to acknowledge the Facility for Analysis, Characterization, Testing and Simulation, Nanyang Technological University, Singapore, for use of their electron microscopy facilities.

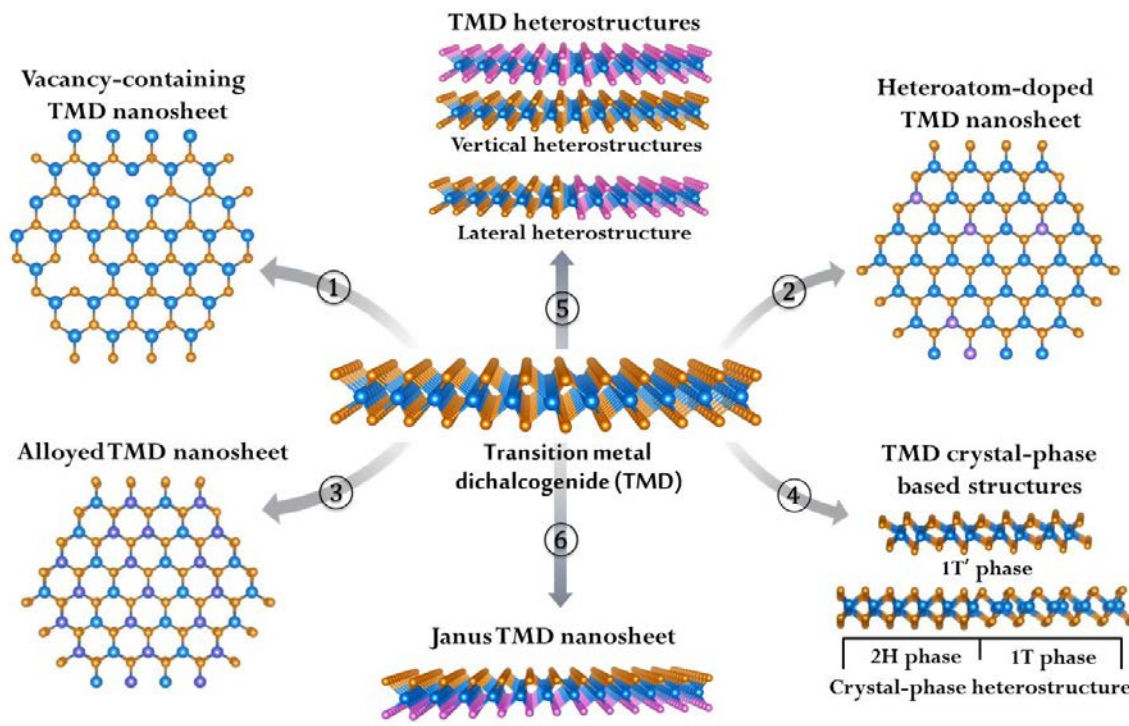


**Figure 1.** Schematic illustration of the recently emerged novel structured TMD nanosheets.

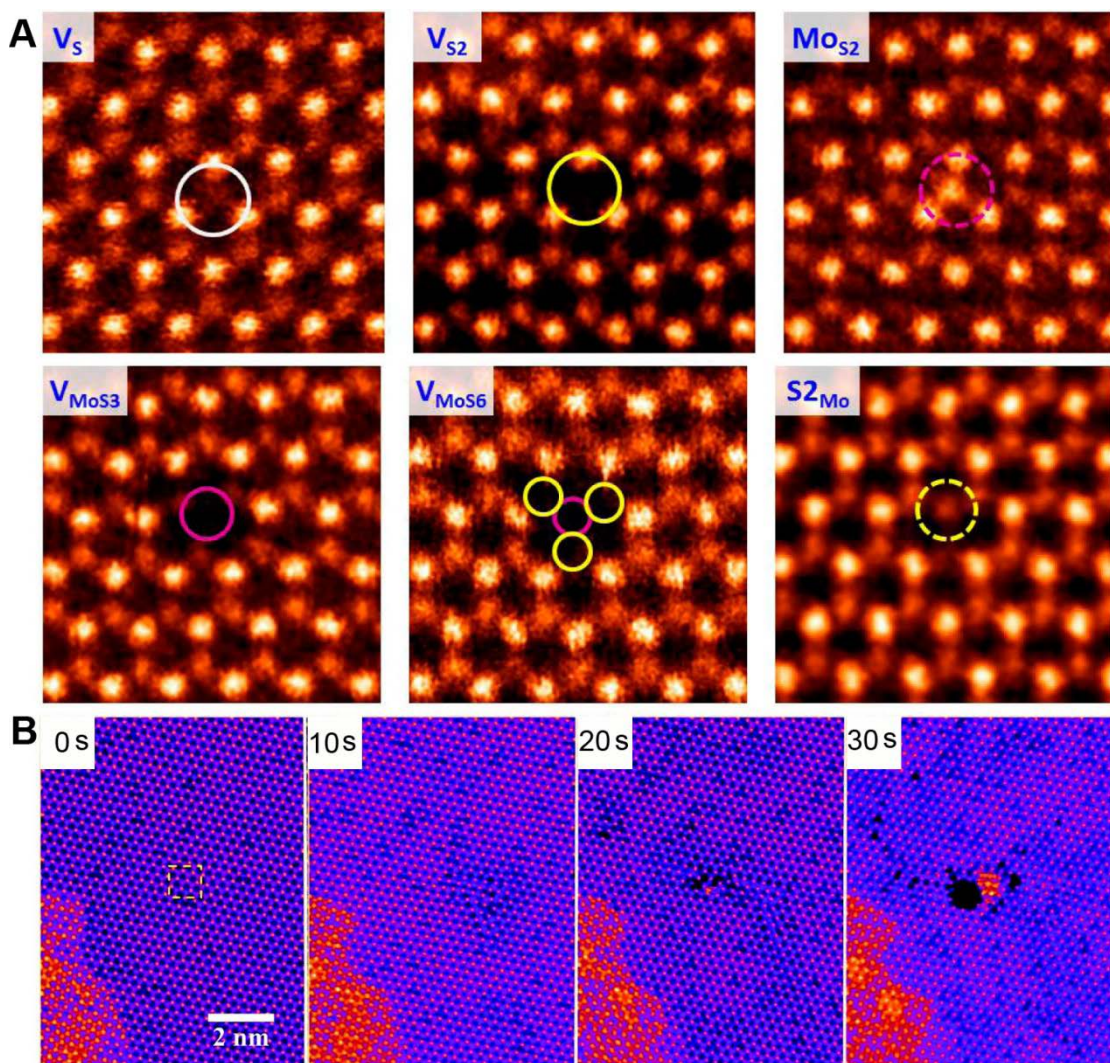


**Figure 2.** (A) Atomic resolution ADF-STEM images of various intrinsic point defects present in monolayer CVD Mo<sub>2</sub>, including V<sub>S</sub>, V<sub>S2</sub>, Mo<sub>S2</sub>, V<sub>MoS3</sub>, V<sub>MoS6</sub>, and S<sub>2Mo</sub>. Reproduced with permission from ref. 56. Copyright 2013, American Chemical Society.<sup>56</sup> (B) ADF-STEM images showing step-by-step drilling of a nanopore in monolayer Mo<sub>2</sub> using 80 kV accelerating voltage taken after 0 s, 10 s, 20 s and 30 s. Reproduced with permission from ref. 71. Copyright 2017, Royal Society of Chemistry.<sup>71</sup>

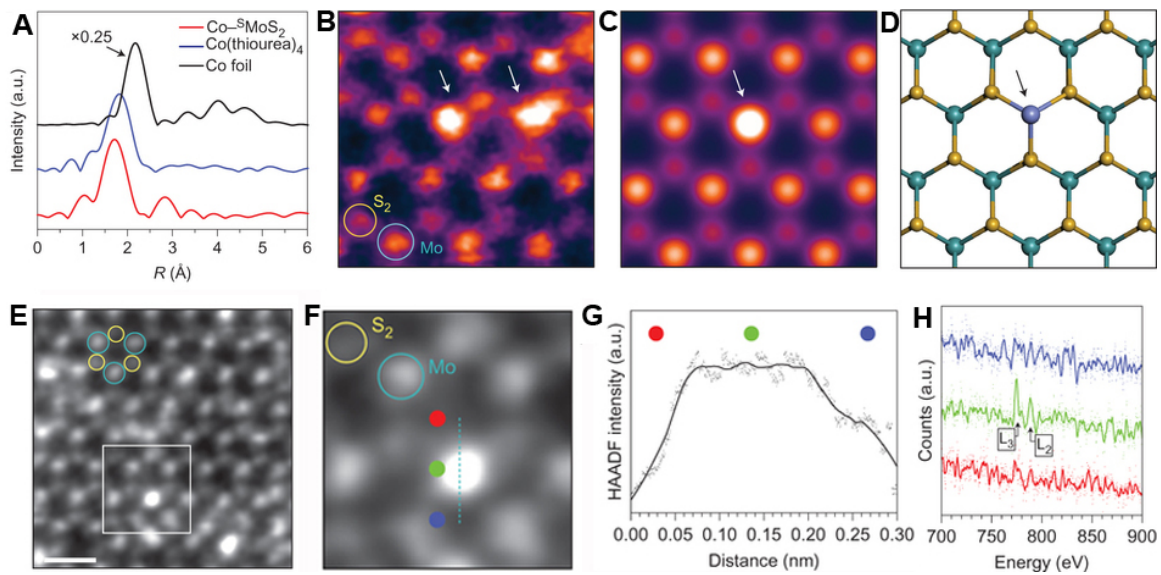


**Figure 3.** (A) Fourier transforms of  $k^3$ -weighted Co K-edge of X-ray absorption fine structure spectroscopy (EXAFS) spectra of Co-MoS<sub>2</sub>, Co(thiourea)<sub>4</sub> and Co foil. (B) ADF-STEM image of Co-MoS<sub>2</sub>, showing two bright contrast sites in the MoS<sub>2</sub> monolayer (arrows). (C, D) An ADF image simulation (C), and corresponding atomic model (D), from geometry optimized DFT of a single Co on Mo atop site. (E) HAADF-STEM image of Co-MoS<sub>2</sub>. Scale bar = 0.5 nm. (F) A magnified view of a Co atom on Mo atop site (boxed area of E). (G, H) Simultaneous acquisition ADF (G) and EELS (H) acquired along the line in F, with EELS extracted from above (red), on (green), and below (blue) the Co atom on Mo atop site. The L<sub>3,2</sub> edges for Co are indicated, confirming the scanned atomic column contains a Co atom. Reproduced with permission from ref. 79. Copyright 2017, Nature Publishing Group.<sup>79</sup>

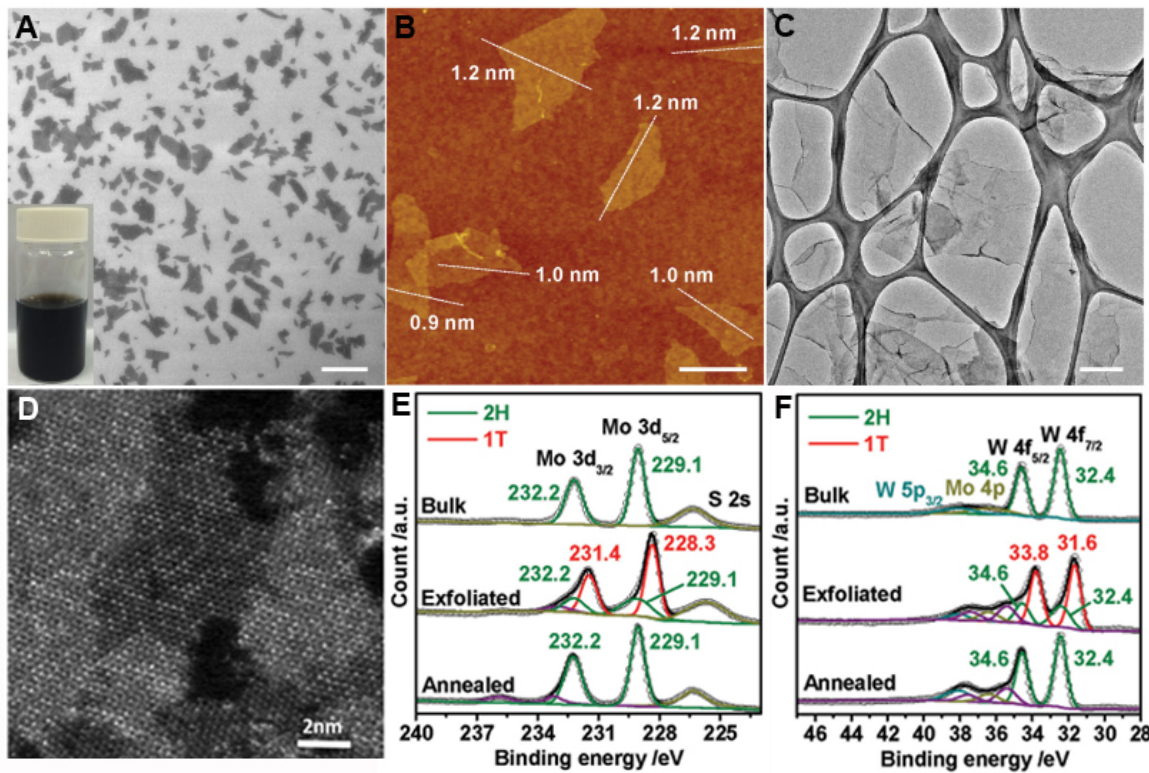


**Figure 4.** (A) SEM image and (B) AFM height image of  $\text{Mo}_x\text{W}_{1-x}\text{S}_2$  nanosheets (scale bars, A: 2  $\mu\text{m}$ ; B: 500 nm). Inset in (A): photograph of colloidal suspension of  $\text{Mo}_x\text{W}_{1-x}\text{S}_2$  nanosheets. (C) TEM image of  $\text{Mo}_x\text{W}_{1-x}\text{S}_2$  nanosheets (scale bar, 500 nm). (D) Atomic STEM image of a typical exfoliated  $\text{Mo}_x\text{W}_{1-x}\text{S}_2$  nanosheet. High-resolution XPS of (E) Mo 3d and (F) W 4f spectrum of bulk crystal of  $\text{Mo}_x\text{W}_{1-x}\text{S}_2$ , the exfoliated and annealed  $\text{Mo}_x\text{W}_{1-x}\text{S}_2$  nanosheets. Reproduced with permission from ref. 96. Copyright 2016, John Wiley & Sons, Inc.<sup>96</sup>

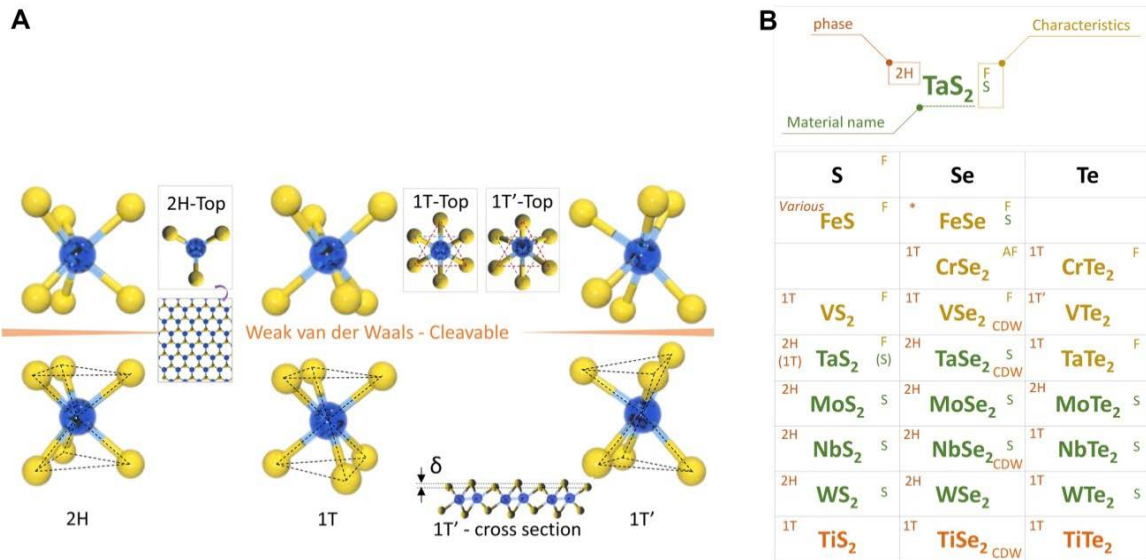


**Figure 5.** (A) Typical structure model of layered TMDs. Cleavable 2H, 1T and 1T' structures in layered TMD are shown. (B) Table for various TMD nanosheets exhibiting various crystal structures (2H, 1T and 1T') and physical properties such as magnetism (ferromagnetic (F)/antiferromagnetic (AF)), superconductivity (S) and charge density wave (CDW) and crystal structures. Reproduced with permission from ref. 115. Copyright 2017, Elsevier.<sup>115</sup>

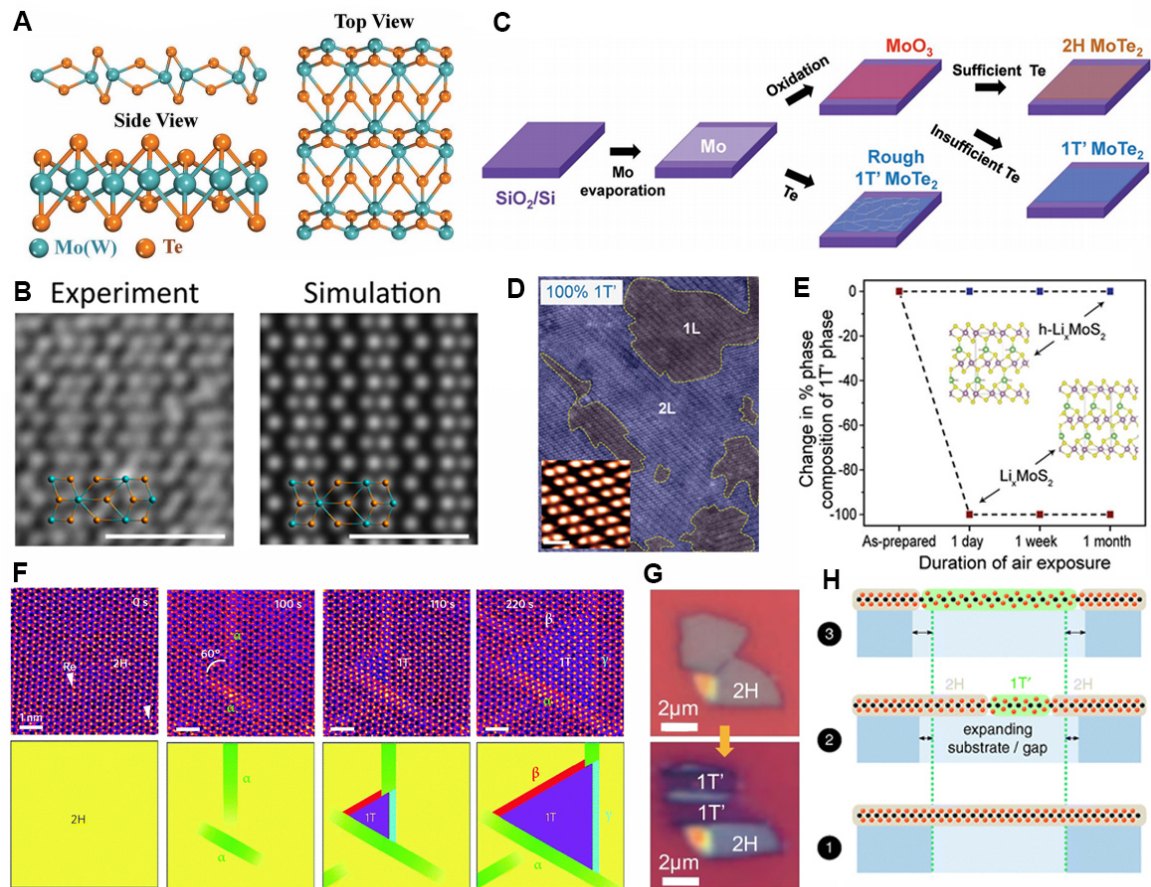


**Figure 6.** (A) Side and top views of the crystal structure of 1T'-MoTe<sub>2</sub>. Reproduced with permission from ref. 137. Copyright 2017, John Wiley & Sons, Inc.<sup>137</sup> (B) The experimental and simulated ADF-STEM image of 1T'-MoTe<sub>2</sub> nanosheets, Mo (blue), Te (orange). The scale bar is 1 nm. Reproduced with permission from ref. 135. Copyright 2016, American Chemical Society.<sup>135</sup> (C) A schematic illustration of the growth process for 1T' and 1H MoTe<sub>2</sub> using Mo and MoO<sub>3</sub> as precursors. Reproduced with permission from ref. 131. Copyright 2016, John Wiley & Sons, Inc.<sup>131</sup> (D) ADF-STEM image of monolayer and bilayer Li<sub>x</sub>MoS<sub>2</sub> regions with false color to differentiate the different layers. Inset: the magnified filtered image of 1T' phase region indicated by the dotted orange box. Scale bars for image and inset are 2.5 and 0.5 nm, respectively. (E) Degradation of Li<sub>x</sub>MoS<sub>2</sub> in ambient conditions as function of time. Reproduced with permission from ref. 153. Copyright 2017, American Chemical Society.<sup>153</sup> (F) 1H to 1T transformation of a single-layer of MoS<sub>2</sub> under electron-beam irradiation. Reproduced with permission from ref. 140. Copyright 2014, Nature Publishing Group.<sup>140</sup> (G) Optical

microscope images of a mechanically exfoliated 1H-MoTe<sub>2</sub> flake before (top) and after (bottom) laser irradiation. Reproduced with permission from ref. 51. Copyright 2015, American Association for the Advancement of Science.<sup>51</sup> (H) 1H to 1T phase transformation of monolayer TMDs when applying uniaxial strain. Reproduced with permission from ref. 160. Copyright 2014, Nature Publishing Group.<sup>160</sup>

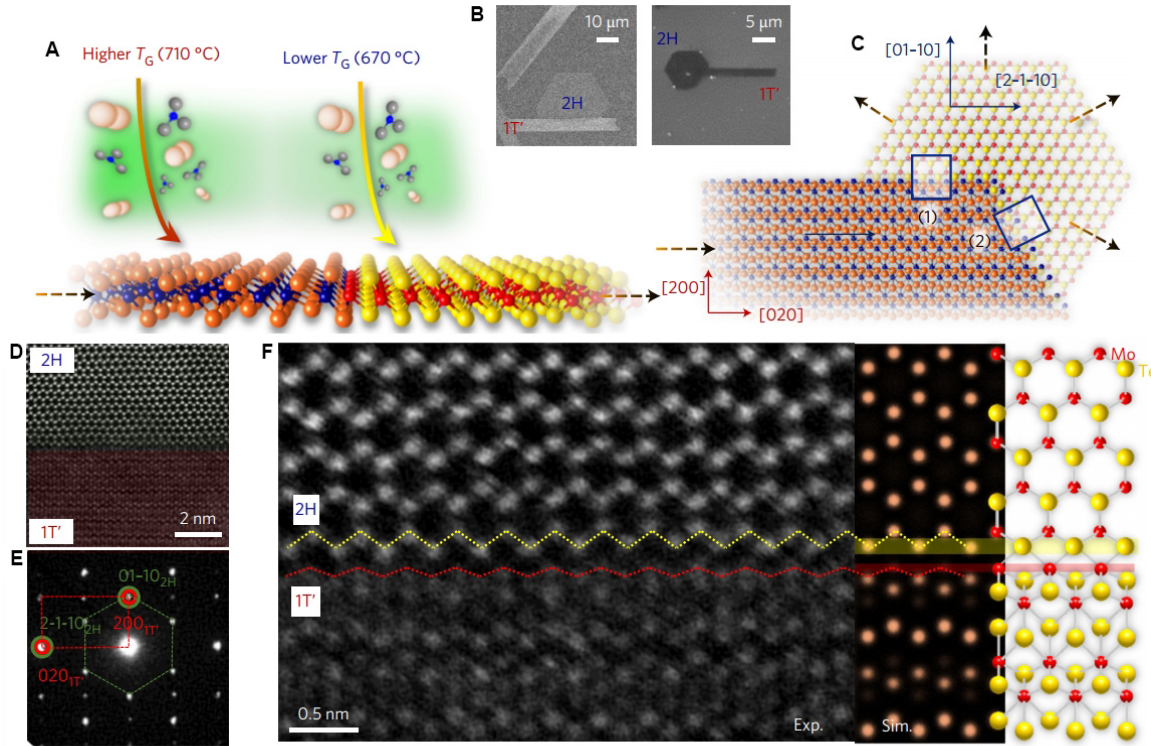


**Figure 7.** (A) Sequential growth scheme for coplanar heteroepitaxy of 1T'-2H MoTe<sub>2</sub> polymorphs. (B) Representative SEM images of the first (left) and second (right) types of crystallographic variants in the heterojunctions between 1T'- and 1H-MoTe<sub>2</sub> crystals. (C) In-plane-view schematics of the two heteroepitaxial variants. (D) Low-magnification ADF-STEM image of the first-type variant of the polymorphic interfaces and (E) SAED patterns taken from the 1T'-2H interface. The dotted rectangle and hexagon denote the crystal symmetry formed by diffracted spots of 1T' (red) and 2H (green) regions, respectively. (F) Left: atomic-resolution ADF-STEM image of the first-type polymorphic interface. This atomically sharp heteroepitaxial 1T'-2H interface verified that the (200) plane of 1T' is bonded to the (01-10) plane of 2H at the zigzag edge (yellow dotted line) formed by Te-termination of 1T' and Mo-termination of 2H (red dotted line). Right: simulated ADF-STEM image of the 1T'/2H interface with superimposed unit-cell schematic (far right). Reproduced with permission from ref. 50. Copyright 2017, Nature Publishing Group.<sup>50</sup>

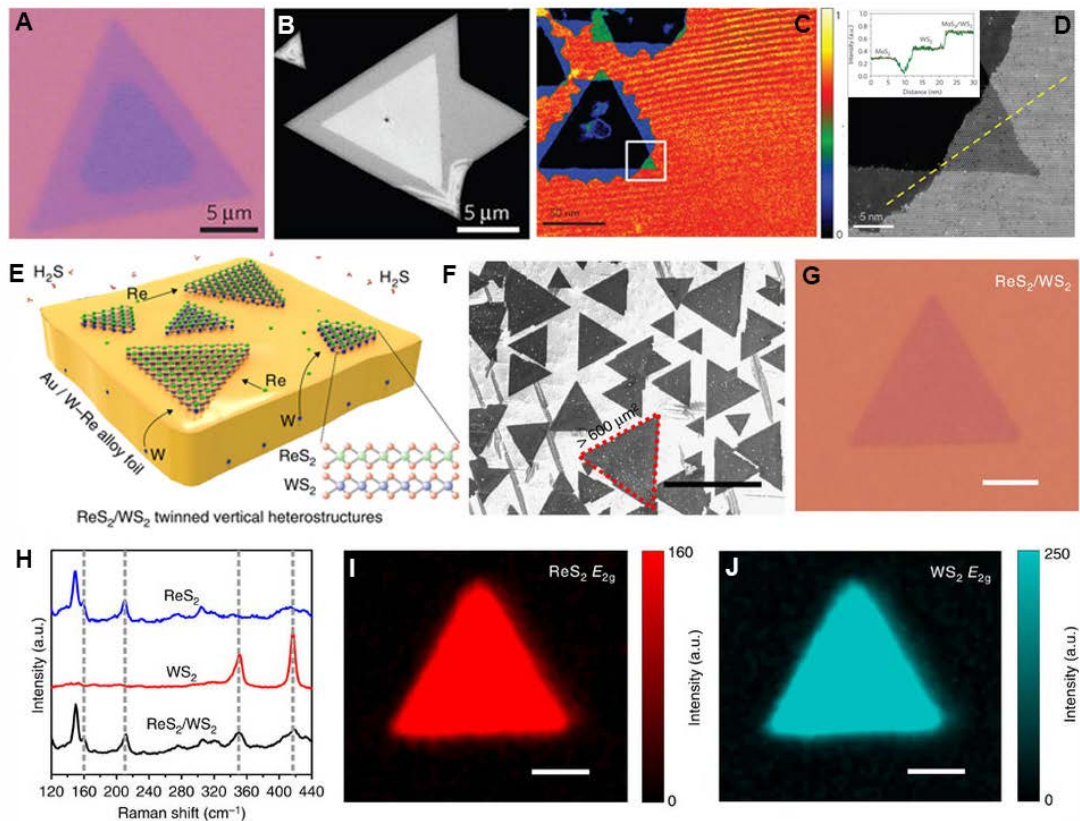


**Figure 8.** (A–B) Optical and SEM images of the vertically stacked WS<sub>2</sub>/MoS<sub>2</sub> heterostructures. (C) Low-magnification false-colour Z-contrast image of the sample, where monolayer MoS<sub>2</sub> is shown in blue, monolayer WS<sub>2</sub> in green, and the WS<sub>2</sub>/MoS<sub>2</sub> bilayer in orange. (D) Zoom-in view of the region outlined by the square in C. The Z-contrast image intensity profile along the dashed line in D is inserted, showing the distinct contrast variation among the different monolayer and bilayer regions. Reproduced with permission from ref. 175. Copyright 2014, Nature Publishing Group.<sup>175</sup>

(E) Schematic for the twinned growth of ReS<sub>2</sub>-WS<sub>2</sub>. (F) SEM image of the triangular ReS<sub>2</sub>-WS<sub>2</sub> vertical crystalline heterostructures over Au. A ReS<sub>2</sub>-WS<sub>2</sub> crystal with grain size up to 600 mm<sup>2</sup> is indicated. (G) Optical image of a ReS<sub>2</sub>-WS<sub>2</sub> twinned vertical heterostructure crystal after transfer onto a Si/SiO<sub>2</sub> substrate. (H) Comparison of the Raman spectra of ReS<sub>2</sub>, WS<sub>2</sub>, and ReS<sub>2</sub>-WS<sub>2</sub>, in which four distinct peaks are observed from the twinned ReS<sub>2</sub>-WS<sub>2</sub> crystal. (I, J) Raman mappings of peak intensity at 160.5 and 351.3 cm<sup>-1</sup> respectively, corresponding to the E<sub>2g</sub> mode of ReS<sub>2</sub> and WS<sub>2</sub> respectively. Scale bar, 40 nm (F); 5 mm (G, I, J). Reproduced with permission from ref. 173. Copyright 2016, Nature Publishing Group.<sup>173</sup>

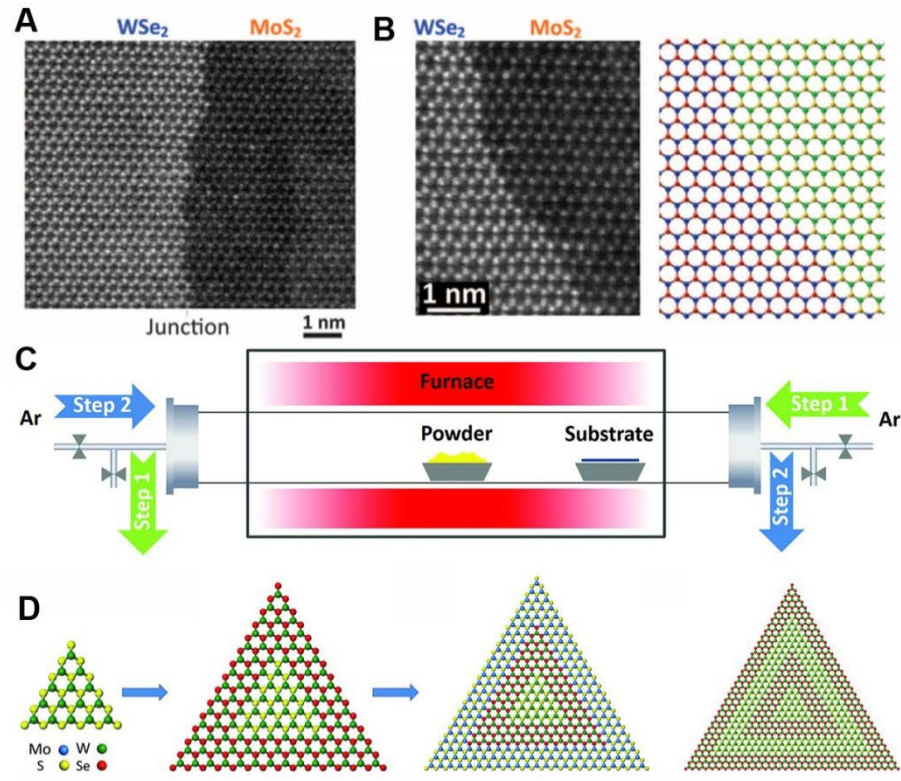


**Figure 9.** (A, B) High-resolution STEM images taken from the WSe<sub>2</sub>-MoS<sub>2</sub> in-plane heterostructure. Reproduced with permission from ref. 189. Copyright 2017, American Association for the Advancement of Science.<sup>189</sup> (C) Schematic illustration of a modified CVD system for the robust epitaxial growth of lateral heterostructures. (D) The sequential growth of monolayer WS<sub>2</sub> seed, WS<sub>2</sub>-WSe<sub>2</sub> heterostructure, WS<sub>2</sub>-WSe<sub>2</sub>-MoS<sub>2</sub> multiheterostructures, and WS<sub>2</sub>-WSe<sub>2</sub>-WS<sub>2</sub>-WSe<sub>2</sub> superlattices. Reproduced with permission from ref. 46. Copyright 2017, American Association for the Advancement of Science.<sup>46</sup>

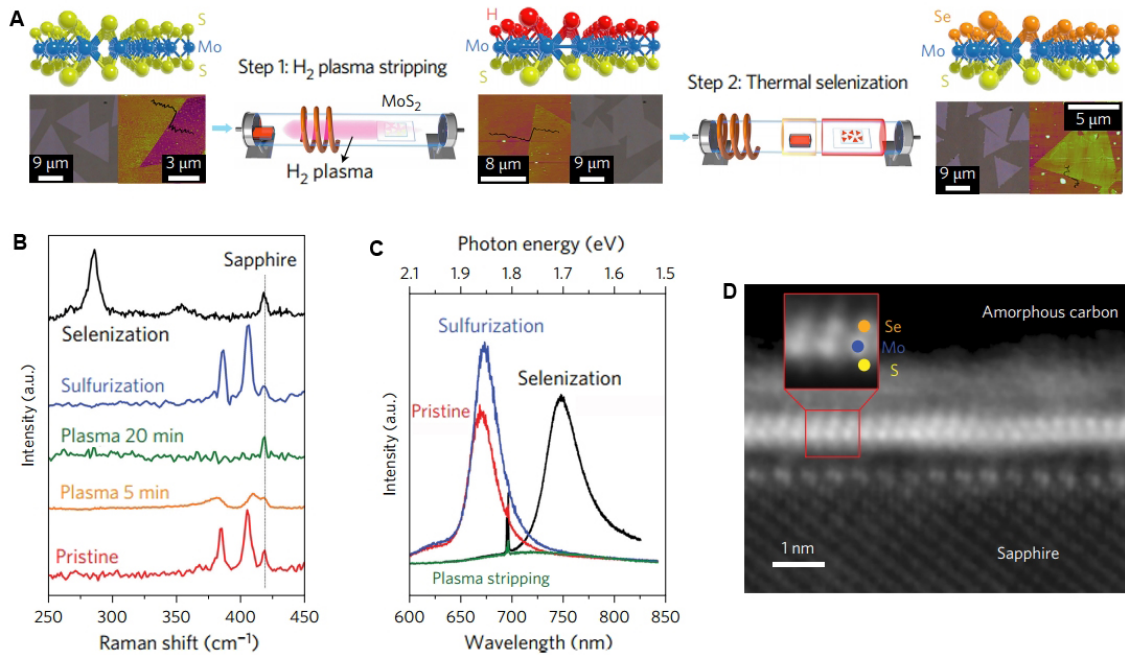


**Figure 10.** (A) Schematic illustration of the procedure for growth of Janus MoSSe monolayers. (B) Raman and (C) PL measurements of the pristine MoS<sub>2</sub> and the MoS<sub>2</sub> after H<sub>2</sub> plasma treatment, sulfurization and selenization. (D) ADF-STEM image of the cross-section of MoSSe monolayer, showing the asymmetric MoSSe monolayer structure with Se (orange) on top and S (yellow) at the bottom of the Mo atoms (blue). Reproduced with permission from ref. 52. Copyright 2017, Nature Publishing Group.<sup>52</sup>

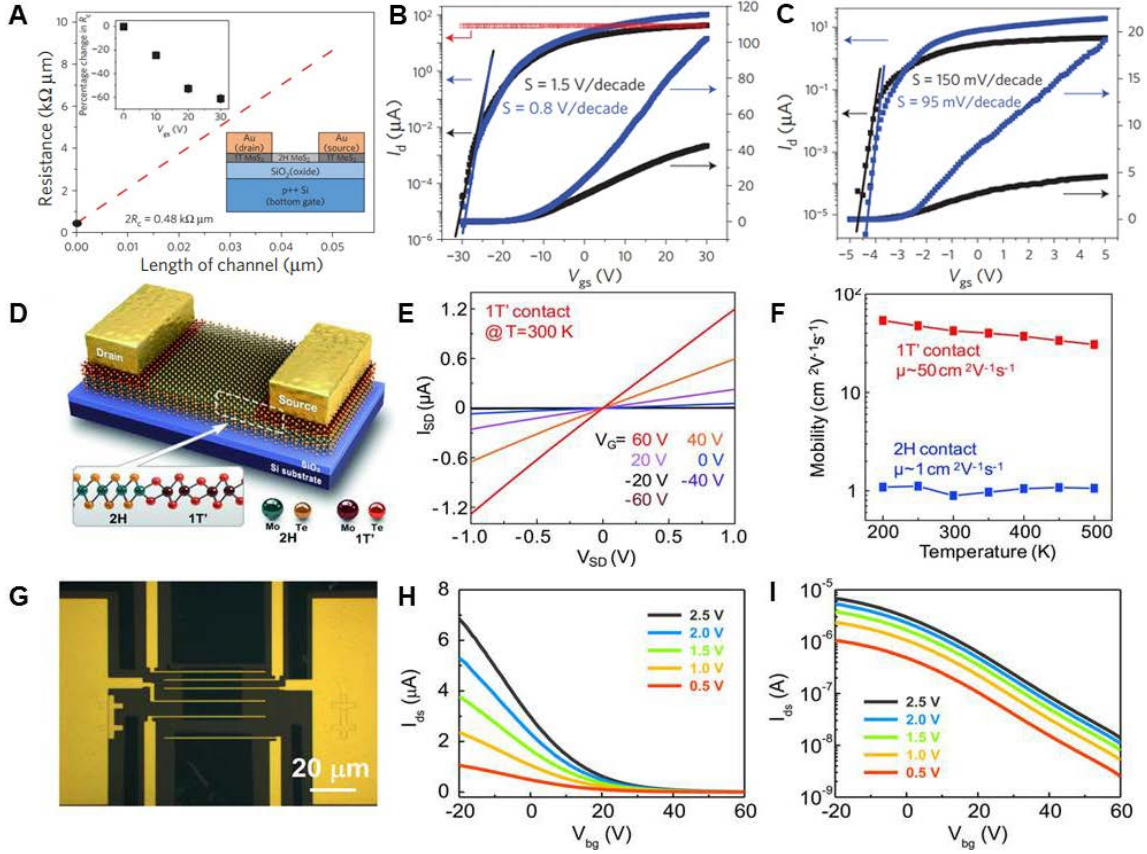


**Figure 11.** (A) The plot of resistance versus length of the 2H-MoS<sub>2</sub> channel. Au electrodes were deposited on the 1T-MoS<sub>2</sub>. Insets: (Top-left) The plot of percentage decrease in contact resistance versus gate bias; (Bottom-right): Scheme of the device configuration. (B, C) Transfer characteristics ( $I$ - $V$ ) of (B) bottom-gated and (C) top-gated devices. Blue curves represent devices with Au electrodes coated 1T-MoS<sub>2</sub>, and the black curves represent devices with Au electrodes coated on the 2H-MoS<sub>2</sub>. The red curve in (B) is the  $I_d$  of the device based on 1T-MoS<sub>2</sub> channel with Au electrodes, showing an absence of gate modulation owing to the metallic character of the 1T-MoS<sub>2</sub>. Reproduced with permission from ref. 48. Copyright 2014, Nature Publishing Group.<sup>48</sup> (D) Schematic diagram of a device with a 1T'/2H-MoTe<sub>2</sub> homojunction. (E) Source-drain current  $I_{\text{SD}}$  characteristics of the device based on 1T'/2H-MoTe<sub>2</sub> homojunction at gate voltage ( $V_G$ ) ranging from -60 V to 60 V. (F) Field-effect mobility as a function of temperature on the 1T'/2H-MoTe<sub>2</sub> homojunction based device. Reproduced with permission from ref. 51. Copyright 2015, American Association for the Advancement of Science.<sup>51</sup> (G) Typical optical image of a 1H-MoTe<sub>2</sub> device on 90 nm SiO<sub>2</sub>/Si. (H, I) Transfer characteristics  $I_{\text{ds}}$ -

$V_{bg}$  curves for the 2H-MoTe<sub>2</sub> based devices at various values of  $V_{ds}$ . Reproduced with permission from ref. 130. Copyright 2015, American Chemical Society.<sup>130</sup>

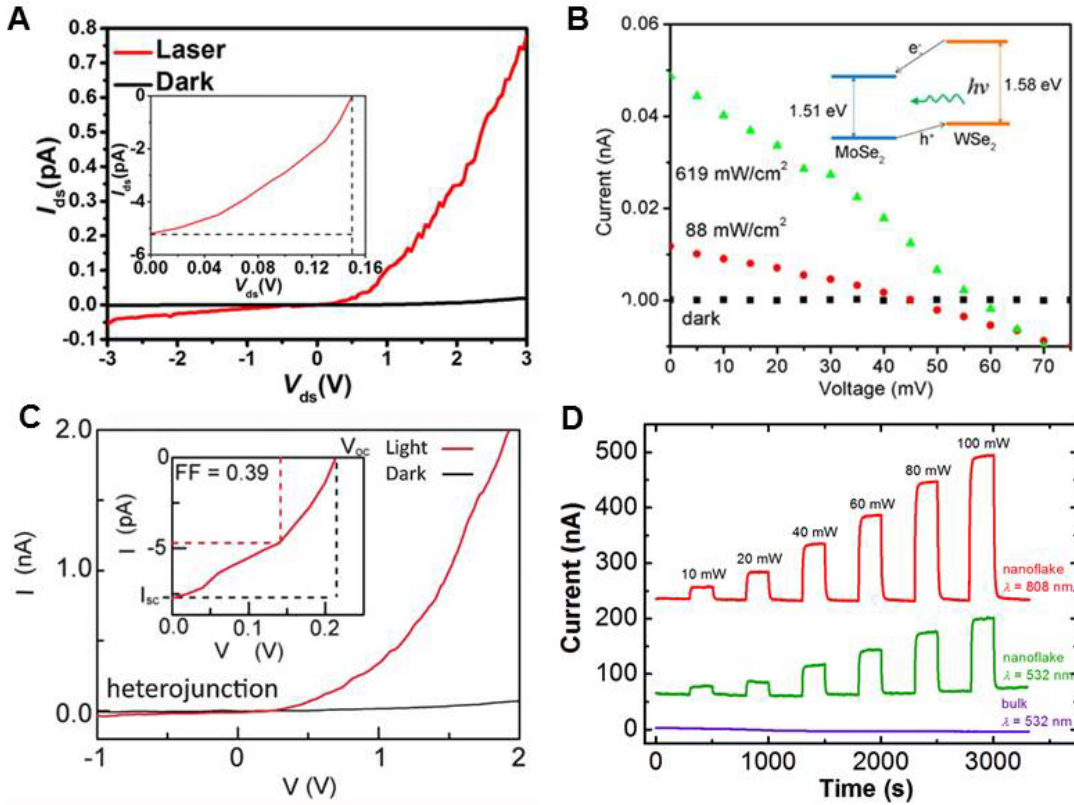


**Figure 12.** (A) Experimental  $I-V$  curve of the lateral  $\text{WS}_2\text{-MoS}_2$  heterojunction diode in the dark (black line) and under illumination with the 514 nm 1 mW laser (red line). Inset: enlarged plot showing an open-circuit voltage of ~0.15 V and a short-circuit current of ~5.2 pA. Reproduced with permission from ref. 201. Copyright 2015, American Chemical Society.<sup>201</sup> (B) The photovoltaic  $I-V$  curve of the  $\text{MoSe}_2\text{-WSe}_2$  heterojunction. Inset: schematic diagram of  $\text{MoSe}_2\text{-WSe}_2$  heterojunction band structure and photoexcitation process in  $\text{MoSe}_2\text{-WSe}_2$  heterojunction. Reproduced with permission from ref. 184. Copyright 2015, American Chemical Society.<sup>184</sup> (C) Electrical transport curves ( $I-V$ ) of the  $\text{WSe}_2\text{-MoS}_2$  heterostructure with and without light exposure (1 mW  $\text{cm}^{-2}$ ), showing the presence of a  $p-n$  junction and photovoltaic effect. Inset: enlarged plot showing an open-circuit voltage of 0.22 V, a short-circuit current of 7.7 pA and a fill factor of 0.39. Reproduced with permission from ref. 189. Copyright 2015, American Association for the Advancement of Science.<sup>189</sup> (D) Photocurrent responses to the excitation wavelengths ( $\lambda$ ) of 532 and 808 nm measured in air for the  $\text{NbSe}_2$  nanoflake with a thickness of 20 nm. A measurement under 532 nm excitation for the bulk crystal is

also shown for comparison. Reproduced with permission from ref. 215. Copyright 2015, Royal Society of Chemistry.<sup>215</sup>

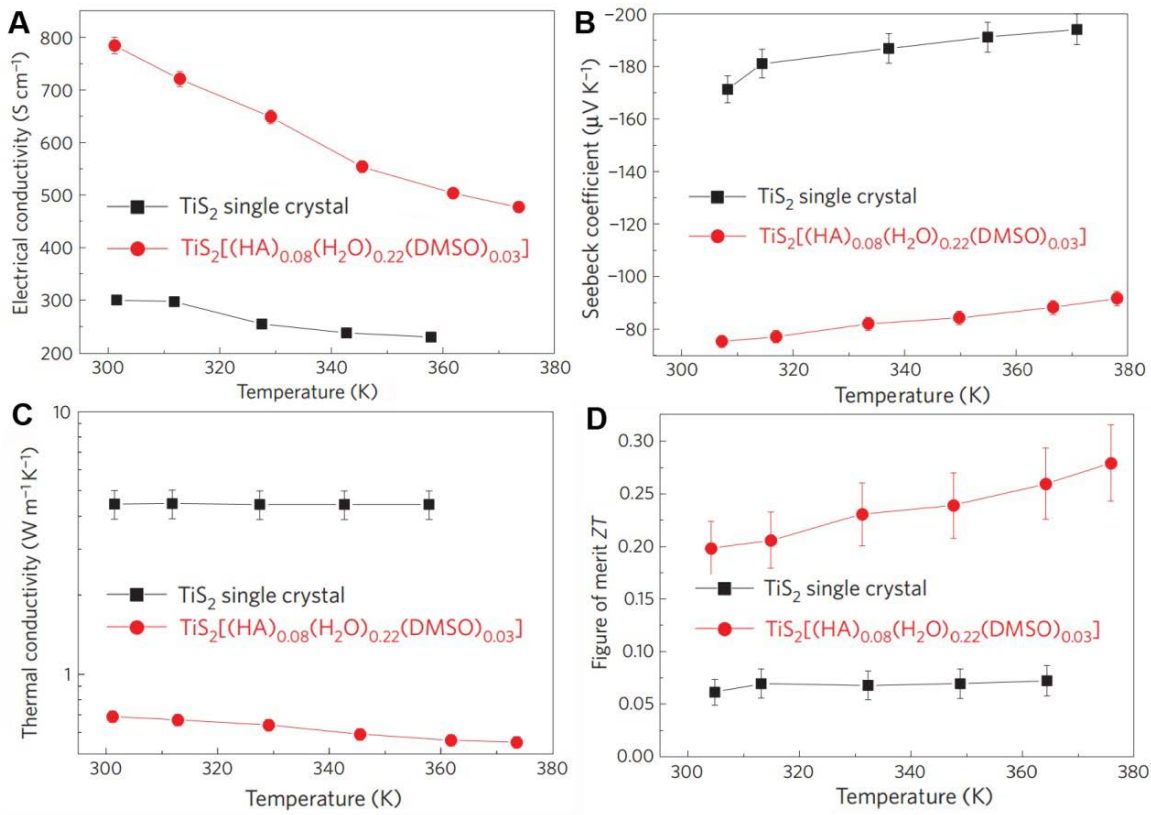


**Figure 13.** (A-D) Comparison of in-plane thermoelectric transport properties of TiS<sub>2</sub>[(HA)<sub>0.08</sub>(H<sub>2</sub>O)<sub>0.22</sub>(DMSO)<sub>0.03</sub>] hybrid superlattice and pristine TiS<sub>2</sub> single crystal: (A) In-plane electrical conductivity, (B) in-plane Seebeck coefficient, (C) in-plane thermal conductivity, and (D) in-plane thermoelectric figure of merit, ZT. Reproduced with permission from ref. 202. Copyright 2015, Nature Publishing Group.<sup>202</sup>

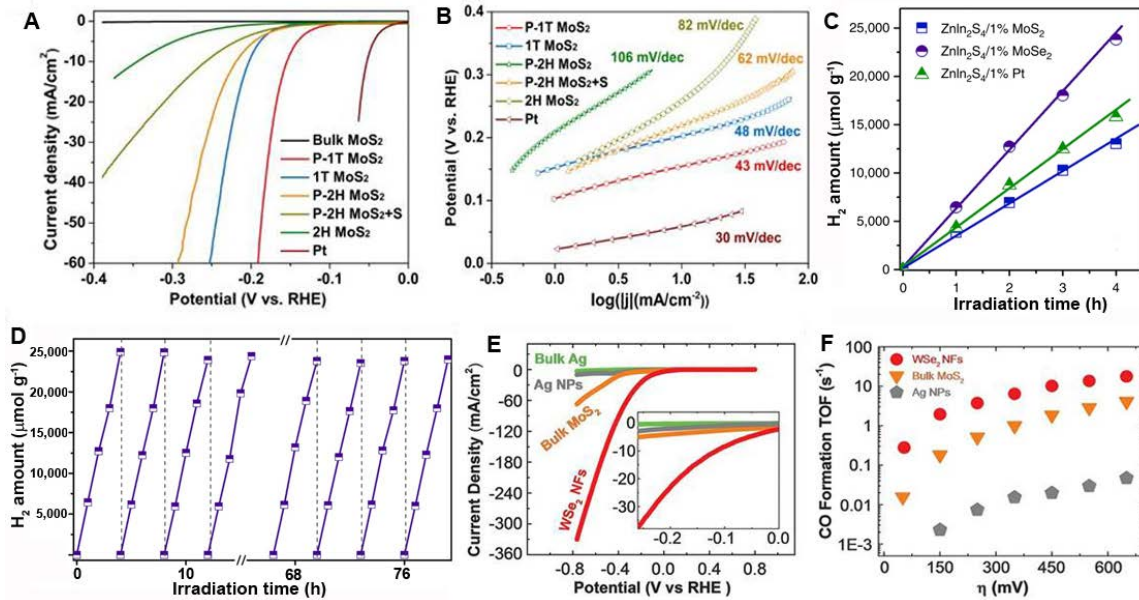


**Figure 14.** (A)  $J$ - $V$  curves after iR correction showing the catalytic performance of various MoS<sub>2</sub> samples in comparison to a Pt wire. (B) Tafel plots obtained from (A). Reproduced with permission from ref. 152. Copyright 2017, American Chemical Society.<sup>152</sup> (C) Comparison of photocatalytic H<sub>2</sub> evolution activities of ZnIn<sub>2</sub>S<sub>4</sub>/1%Pt, ZnIn<sub>2</sub>S<sub>4</sub>/1%MoS<sub>2</sub> and ZnIn<sub>2</sub>S<sub>4</sub>/1%MoSe<sub>2</sub>. (D) Recycling photocatalytic activity tests of ZnIn<sub>2</sub>S<sub>4</sub>/1%MoSe<sub>2</sub>. Reproduced with permission from ref. 236. Copyright 2017, Nature Publishing Group.<sup>236</sup> (E) CV curves for WSe<sub>2</sub> nanoflakes (NFs), bulk MoS<sub>2</sub>, Ag nanoparticles (NPs), and bulk Ag in CO<sub>2</sub> environment. Inset: Current densities in low overpotentials. (F) CO formation turnover frequency (TOF) of WSe<sub>2</sub> NFs, bulk MoS<sub>2</sub>, and Ag NPs in ionic liquid electrolyte at overpotentials from 54 to 650 mV. At the overpotential of 54 mV, the CO formation TOF of Ag NPs is zero. Reproduced with permission from ref. 228. Copyright 2016, American Association for the Advancement of Science.<sup>228</sup>

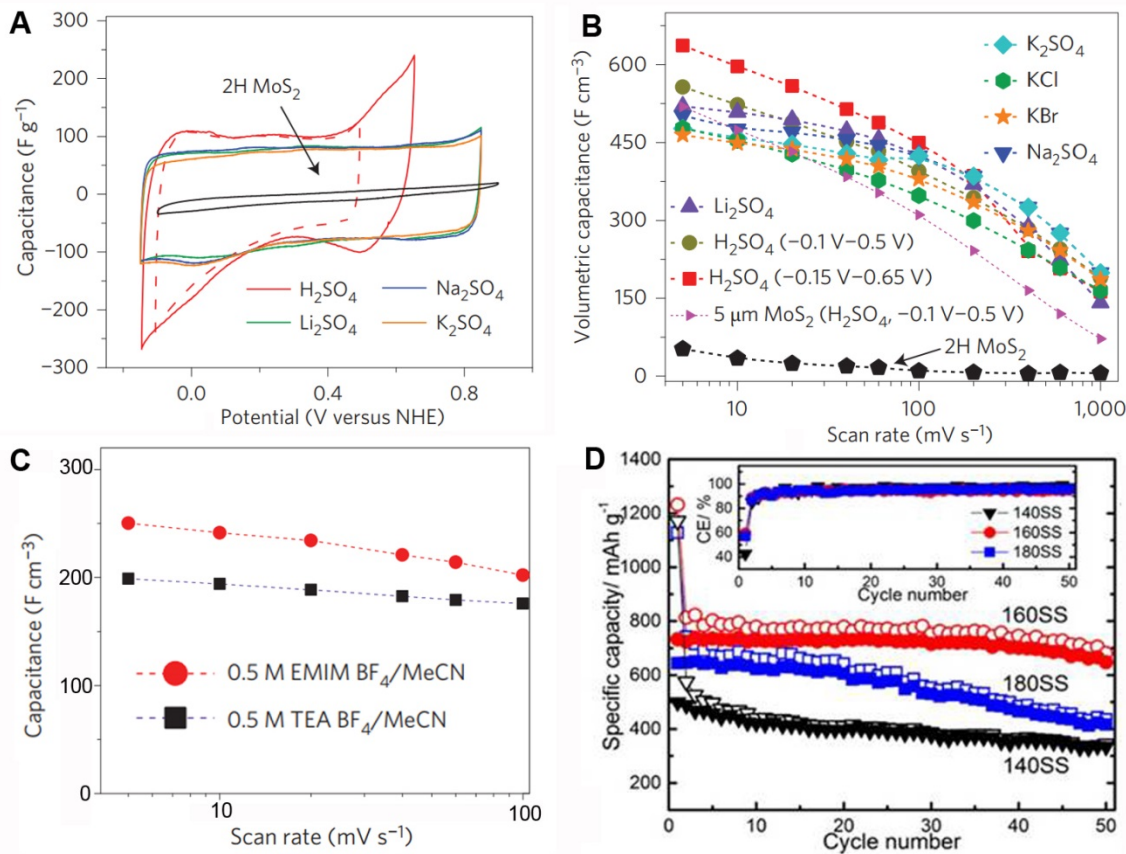


**Figure 15.** (A) CV curves of 1T-MoS<sub>2</sub> nanosheet based electrode in 0.5 M sulphate-based electrolyte solutions at scan rate of 20 mV s<sup>-1</sup>. (B) The scan rate-dependent volumetric capacitance of the 1-μm-thick 1T-MoS<sub>2</sub> electrodes in different electrolytes and 5-μm-thick 1T-MoS<sub>2</sub> electrode in H<sub>2</sub>SO<sub>4</sub>. (C) The plot of capacitance versus scan rate of 1T-MoS<sub>2</sub> electrodes in TEA BF<sub>4</sub>/MeCN and EMIM BF<sub>4</sub>/MeCN electrolytes. Reproduced with permission from ref. 116. Copyright 2015, Nature Publishing Group.<sup>116</sup> (D) Cycling performances of the cells at 0.1 A g<sup>-1</sup> with electrodes of SnS<sub>2</sub> nanosheets synthesized at 140 °C (140SS), 160 °C (160SS), and 180 °C (180SS). Inset: the Coulombic efficiencies of the three cells. Reproduced with permission from ref. 241. Copyright 2015, American Chemical Society.<sup>241</sup>

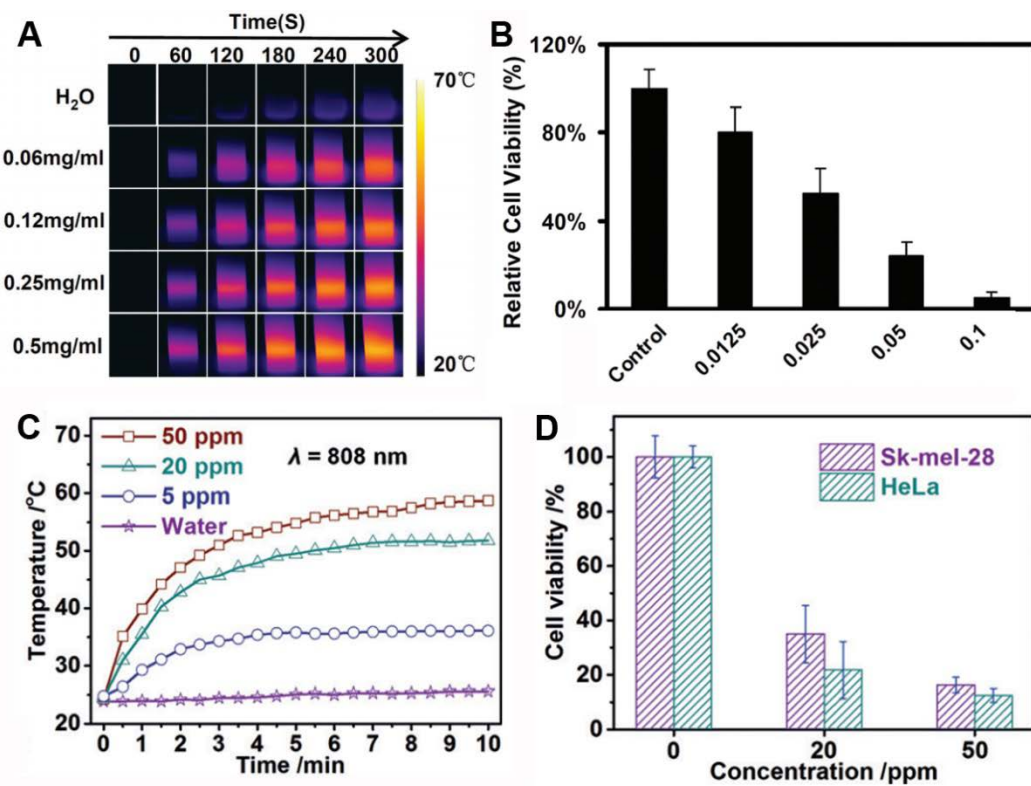


**Figure 16.** (A) IR thermal images of pure water and TiS<sub>2</sub>-PEG solutions with different concentrations (0.06, 0.12, 0.25, and 0.5 mg mL<sup>-1</sup>) under 808 nm laser irradiation at a power density of 0.8 W cm<sup>-2</sup>. (B) Relative viabilities of 4T1 cells after incubation with different concentrations of TiS<sub>2</sub>-PEG and then being exposed to an 808 nm laser at a power density of 0.8 W cm<sup>-2</sup> for 5 min. Reproduced with permission from ref. 213. Copyright 2015, Royal Society of Chemistry.<sup>213</sup> (C) Photothermal heating curves of pure water and solutions of LA-PEG modified Ti<sub>0.71</sub>Ta<sub>0.29</sub>S<sub>y</sub>O<sub>z</sub> nanosheets at concentrations of 5, 20, and 50 ppm. Irradiation wavelength is 808 nm. (D) Relative viabilities of Sk-mel-28 and HeLa cells incubated in LA-PEG-modified Ti<sub>0.71</sub>Ta<sub>0.29</sub>S<sub>y</sub>O<sub>z</sub> nanosheets at different concentrations (0, 20, and 50 ppm) under laser irradiation ( $\lambda=808$  nm). Reproduced with permission from ref. 243. Copyright 2016, John Wiley & Sons, Inc.<sup>243</sup>

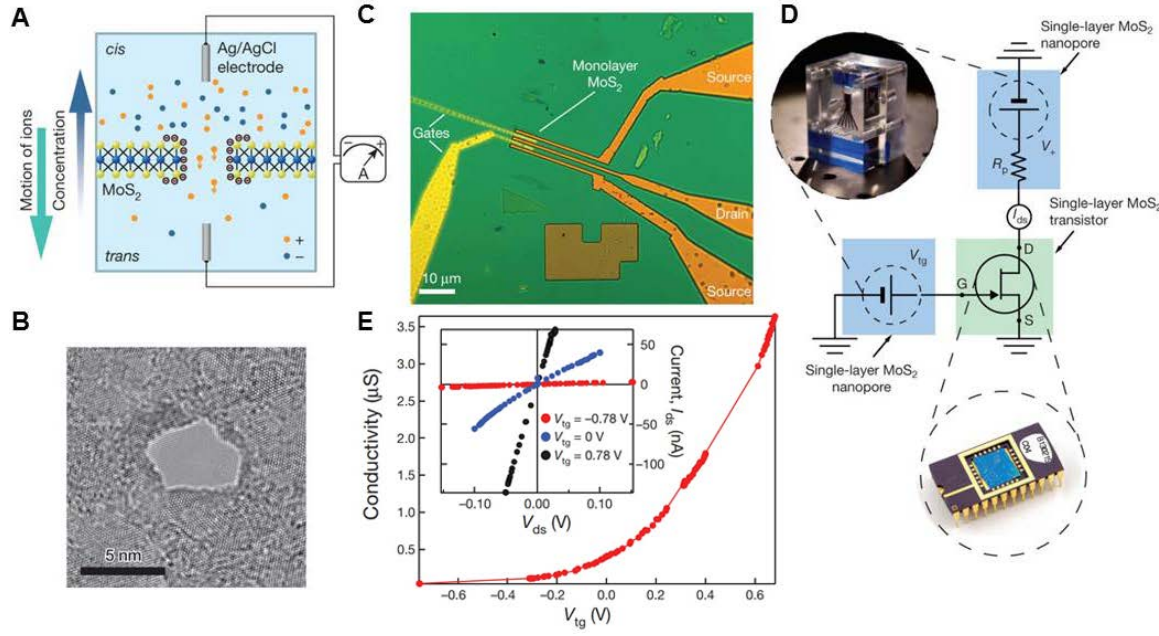


**Figure 17.** (A) The schematic experimental set-up based on porous  $\text{MoS}_2$  for harvesting osmotic energy. Two salt solutions with different concentrations are separated by a 0.65-nm-thick  $\text{MoS}_2$  nanopore membrane. An ion flux driven by chemical potential through the pore is screened by the negatively charged pore, forming a diffusion current composed of mostly positively charged ions. (B) Example of a TEM-drilled  $\text{MoS}_2$  nanopore with diameter of 5 nm. (C) Optical image of the fabricated  $\text{MoS}_2$  transistor with designed gate, drain and source electrodes. (D) Circuit diagram for the self-powered nanosystem composed of two nanopore generators. The drain-source supply for the  $\text{MoS}_2$  transistor is provided by a  $\text{MoS}_2$  nanopore, while a second nanopore device operates as the gate voltage source. D: drain; G: gate; S: source;  $R_p$ : pore resistance;  $V_{tg}$ : gate voltage;  $V_+$ : nanopore output voltage.  $R_p$  connected in series with  $V_{tg}$  has been omitted. (E) The modulated conductivity of the  $\text{MoS}_2$  transistor powered by nanopore generators as a function of the top gate voltage ( $V_{tg}$ ). Inset:  $I-V$  characteristics at various gate voltages ( $-0.78$  V,  $0$  V and  $0.78$  V). Reproduced with permission from ref. 60. Copyright 2016, Nature Publishing Group.<sup>60</sup>

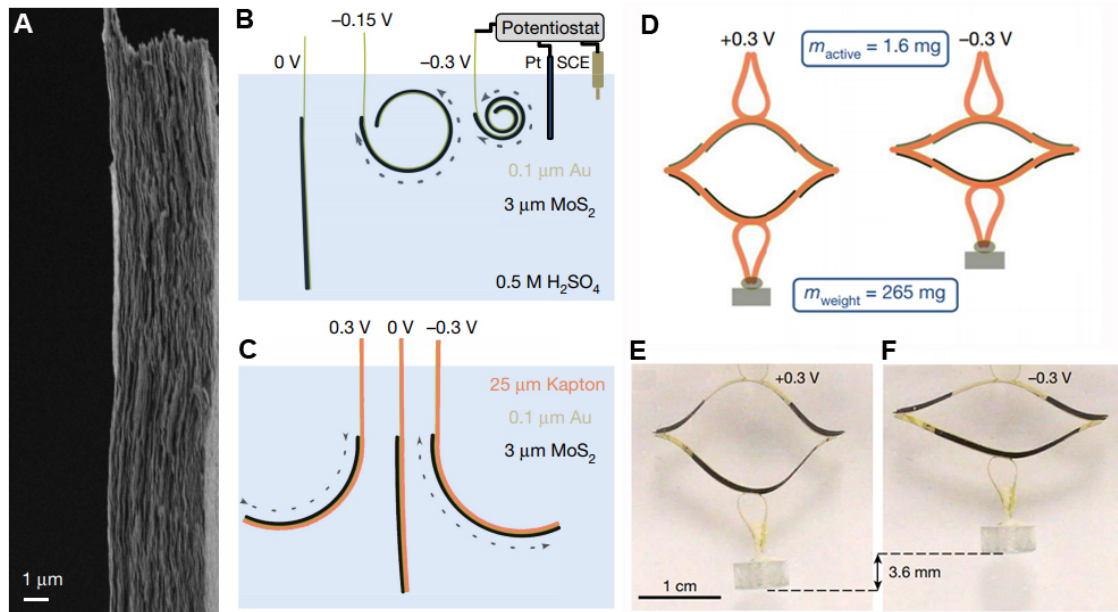


**Figure 18.** (A) SEM image of the restacked 1T-MoS<sub>2</sub> film. (B) The electrochemical system consists of a working electrode (the actuator) along with a counter electrode (Pt) and a reference electrode (standard calomel electrode, SCE) submerged in 0.5 M H<sub>2</sub>SO<sub>4</sub>. (C) Diagram of actuation in forward and backward directions by modulation of the electrode potential between -0.3 V and +0.3 V. (D) Diagrams of the assembled inverted-series-connected (ISC) bimorph actuator attached with a 265-mg weight. The black regions in the schematic represent the locations of the MoS<sub>2</sub> films in the assembled device. Left: the equilibrium position at an open circuit voltage of +0.3 V; Right: lifting of the weight via the application of -0.3 V. (E, F) Photographs of the actuator at the equilibrium position (E) and lifting the weight by 3.6 mm upon charging of the MoS<sub>2</sub> film (F). Reproduced with permission from ref. 244. Copyright 2017, Nature Publishing Group.<sup>244</sup>

## Reference

1. C. Tan, X. Cao, X.-J. Wu, Q. He, J. Yang, X. Zhang, J. Chen, W. Zhao, S. Han, G.-H. Nam, M. Sindoro, H. Zhang, *Chem. Rev.*, 2017, **117**, 6225-6331.
2. H. Zhang, *ACS Nano*, 2015, **9**, 9451-9469.
3. S. Das, J. A. Robinson, M. Dubey, H. Terrones, M. Terrones, *Annu. Rev. Mater. Res.*, 2015, **45**, 1-27.
4. X. Duan, C. Wang, A. Pan, R. Yu, X. Duan, *Chem. Soc. Rev.*, 2015, **44**, 8859-8876.
5. A. Gupta, T. Sakthivel, S. Seal, *Prog. Mater. Sci.*, 2015, **73**, 44-126.
6. R. Lv, J. A. Robinson, R. E. Schaak, D. Sun, Y. F. Sun, T. E. Mallouk, M. Terrones, *Acc. Chem. Res.*, 2015, **48**, 56-64.
7. S. Manzeli, D. Ovchinnikov, D. Pasquier, O. V. Yazyev, A. Kis, *Nat. Rev. Mater.*, 2017, **2**, 17033.
8. V. Nicolosi, M. Chhowalla, M. G. Kanatzidis, M. S. Strano, J. N. Coleman, *Science*, 2013, **340**, 1226419.
9. M. Chhowalla, Z. F. Liu, H. Zhang, *Chem. Soc. Rev.*, 2015, **44**, 2584-2586.
10. X. Huang, Z. Y. Zeng, H. Zhang, *Chem. Soc. Rev.*, 2013, **42**, 1934-1946.
11. S. Z. Butler, S. M. Hollen, L. Cao, Y. Cui, J. A. Gupta, H. R. Gutiérrez, T. F. Heinz, S. S. Hong, J. Huang, A. F. Ismach, E. Johnston-Halperin, M. Kuno, V. V. Plashnitsa, R. D. Robinson, R. S. Ruoff, S. Salahuddin, J. Shan, L. Shi, M. G. Spencer, M. Terrones, W. Windl, J. E. Goldberger, *ACS Nano*, 2013, **7**, 2898-2926.
12. L. Zhong, M. Amber, B. Natalie, S. Shruti, Z. Kehao, S. Yifan, L. Xufan, J. B.

- Nicholas, Y. Hongtao, K. F.-S. Susan, C. Alexey, Z. Hui, M. Stephen, M. L. Aaron, X. Kai, J. L. Brian, D. Marija, C. M. H. James, P. Jiwoong, C. Manish, E. S. Raymond, J. Ali, C. H. Mark, R. Joshua, T. Mauricio, *2D Materials*, 2016, **3**, 042001.
13. X. Zhang, H. Cheng, H. Zhang, *Adv. Mater.*, 2017, **29**, 1701704.
14. X. Zhang, Z. Lai, Z. Liu, C. Tan, Y. Huang, B. Li, M. Zhao, L. Xie, W. Huang, H. Zhang, *Angew. Chem. Int. Ed.*, 2015, **54**, 5425-5428.
15. Y. Liu, N. O. Weiss, X. D. Duan, H. C. Cheng, Y. Huang, X. F. Duan, *Nat. Rev. Mater.*, 2016, **1**, 16042.
16. Q. H. Wang, K. Kalantar-Zadeh, A. Kis, J. N. Coleman, M. S. Strano, *Nat. Nanotechnol.*, 2012, **7**, 699-712.
17. K. F. Mak, J. Shan, *Nat. Photonics*, 2016, **10**, 216-226.
18. F. H. L. Koppens, T. Mueller, P. Avouris, A. C. Ferrari, M. S. Vitiello, M. Polini, *Nat. Nanotechnol.*, 2014, **9**, 780-793.
19. G. Fiori, F. Bonaccorso, G. Iannaccone, T. Palacios, D. Neumaier, A. Seabaugh, S. K. Banerjee, L. Colombo, *Nat. Nanotechnol.*, 2014, **9**, 768-779.
20. M. Chhowalla, D. Jena, H. Zhang, *Nat. Rev. Mater.*, 2016, **1**, 16052.
21. Z. Zeng, Z. Yin, X. Huang, H. Li, Q. He, G. Lu, F. Boey, H. Zhang, *Angew. Chem. Int. Ed.*, 2011, **50**, 11093-11097.
22. X. Zhang, Z. Lai, C. Tan, H. Zhang, *Angew. Chem. Int. Ed.*, 2016, **55**, 8816-8838.
23. H. Li, J. M. T. Wu, Z. Y. Yin, H. Zhang, *Acc. Chem. Res.*, 2014, **47**, 1067-1075.
24. H. Li, G. Lu, Y. Wang, Z. Yin, C. Cong, Q. He, L. Wang, F. Ding, T. Yu, H. Zhang, *Small*, 2013, **9**, 1974-1981.

25. X. M. Geng, W. W. Sun, W. Wu, B. Chen, A. Al-Hilo, M. Benamara, H. L. Zhu, F. Watanabe, J. B. Cui, T. P. Chen, *Nat. Commun.*, 2016, **7**, 10672.
26. R. J. Smith, P. J. King, M. Lotya, C. Wirtz, U. Khan, S. De, A. O'Neill, G. S. Duesberg, J. C. Grunlan, G. Moriarty, J. Chen, J. Wang, A. I. Minett, V. Nicolosi, J. N. Coleman, *Adv. Mater.*, 2011, **23**, 3944-3948.
27. Z. Zeng, T. Sun, J. Zhu, X. Huang, Z. Yin, G. Lu, Z. Fan, Q. Yan, H. H. Hng, H. Zhang, *Angew. Chem. Int. Ed.*, 2012, **51**, 9052-9056.
28. J. N. Coleman, M. Lotya, A. O'Neill, S. D. Bergin, P. J. King, U. Khan, K. Young, A. Gaucher, S. De, R. J. Smith, I. V. Shvets, S. K. Arora, G. Stanton, H.-Y. Kim, K. Lee, G. T. Kim, G. S. Duesberg, T. Hallam, J. J. Boland, J. J. Wang, J. F. Donegan, J. C. Grunlan, G. Moriarty, A. Shmeliiov, R. J. Nicholls, J. M. Perkins, E. M. Grieveson, K. Theuwissen, D. W. McComb, P. D. Nellist, V. Nicolosi, *Science*, 2011, **331**, 568-571.
29. Y.-H. Lee, X.-Q. Zhang, W. Zhang, M.-T. Chang, C.-T. Lin, K.-D. Chang, Y.-C. Yu, J. T.-W. Wang, C.-S. Chang, L.-J. Li, T.-W. Lin, *Adv. Mater.*, 2012, **24**, 2320-2325.
30. J. Yu, J. Li, W. Zhang, H. Chang, *Chem. Sci.*, 2015, **6**, 6705-6716.
31. Y. Shi, H. Li, L.-J. Li, *Chem. Soc. Rev.*, 2015, **44**, 2744-2756.
32. Q. L. Feng, N. N. Mao, J. X. Wu, H. Xu, C. M. Wang, J. Zhang, L. M. Xie, *ACS Nano*, 2015, **9**, 7450-7455.
33. J. Wang, H. Zheng, G. Xu, L. Sun, D. Hu, Z. Lu, L. Liu, J. Zheng, C. Tao, L. Jiao, *J. Am. Chem. Soc.*, 2016, **138**, 16216-16219.
34. D. K. Hu, G. C. Xu, L. Xing, X. X. Yan, J. Y. Wang, J. Y. Zheng, Z. X. Lu, P.

- Wang, X. Q. Pan, L. Y. Jiao, *Angew. Chem. Int. Ed.*, 2017, **56**, 3611-3615.
35. B. Mahler, V. Hoepfner, K. Liao, G. A. Ozin, *J. Am. Chem. Soc.*, 2014, **136**, 14121-14127.
36. Y. Sun, K. Fujisawa, Z. Lin, Y. Lei, J. S. Mondschein, M. Terrones, R. E. Schaak, *J. Am. Chem. Soc.*, 2017, **139**, 11096-11105.
37. L. Zhong, R. C. Bruno, K. Ethan, L. Ruitao, R. Rahul, T. Humberto, A. P. Marcos, T. Mauricio, *2D Mater.*, 2016, **3**, 022002.
38. J. Hong, C. Jin, J. Yuan, Z. Zhang, *Adv. Mater.*, 2017, **29**, 1606434.
39. A. Yoon, Z. Lee, *Appl. Microsc.*, 2017, **47**, 19-28.
40. A. Kutana, E. S. Penev, B. I. Yakobson, *Nanoscale*, 2014, **6**, 5820-5825.
41. H. Li, Y. Li, A. Aljarb, Y. Shi, L.-J. Li, *Chem. Rev.*, 2017, DOI: 10.1021/acs.chemrev.7b00212.
42. H. Yang, S. W. Kim, M. Chhowalla, Y. H. Lee, *Nat. Phys.*, 2017, **13**, 931-937.
43. D. Voiry, A. Mohite, M. Chhowalla, *Chem. Soc. Rev.*, 2015, **44**, 2702-2712.
44. C. Tan, Z. Luo, A. Chaturvedi, Y. Cai, Y. Du, Y. Gong, Y. Huang, Z. Lai, X. Zhang, L. Zheng, X. Qi, M. H. Goh, J. Wang, S. Han, X. J. Wu, L. Gu, C. Kloc, H. Zhang, *Adv. Mater.*, 2018, **30**, 1705509.
45. K. S. Novoselov, A. Mishchenko, A. Carvalho, A. H. Castro Neto, *Science*, 2016, **353**, aac9439.
46. Z. Zhang, P. Chen, X. Duan, K. Zang, J. Luo, X. Duan, *Science*, 2017, **357**, 788-792.
47. Y. Yu, G.-H. Nam, Q. He, X.-J. Wu, K. Zhang, Z. Yang, J. Chen, Q. Ma, M. Zhao, Z. Liu, F.-R. Ran, X. Wang, H. Li, B. Li, Q. Xiong, Q. Zhang, Z. Liu, L.

- Gu, Y. Du, W. Huang, H. Zhang, *Nat. Chem.*, 2018. DOI: 10.1038/s41557-018-0035-6.
48. R. Kappera, D. Voiry, S. E. Yalcin, B. Branch, G. Gupta, A. D. Mohite, M. Chhowalla, *Nat. Mater.*, 2014, **13**, 1128-1134.
49. X. Lin, J. C. Lu, Y. Shao, Y. Y. Zhang, X. Wu, J. B. Pan, L. Gao, S. Y. Zhu, K. Qian, Y. F. Zhang, D. L. Bao, L. F. Li, Y. Q. Wang, Z. L. Liu, J. T. Sun, T. Lei, C. Liu, J. O. Wang, K. Ibrahim, D. N. Leonard, W. Zhou, H. M. Guo, Y. L. Wang, S. X. Du, S. T. Pantelides, H. J. Gao, *Nat. Mater.*, 2017, **16**, 717-721.
50. J. H. Sung, H. Heo, S. Si, Y. H. Kim, H. R. Noh, K. Song, J. Kim, C.-S. Lee, S.-Y. Seo, D.-H. Kim, H. K. Kim, H. W. Yeom, T.-H. Kim, S.-Y. Choi, J. S. Kim, M.-H. Jo, *Nat. Nanotechnol.*, 2017, **12**, 1064–1070.
51. S. Cho, S. Kim, J. H. Kim, J. Zhao, J. Seok, D. H. Keum, J. Baik, D.-H. Choe, K. J. Chang, K. Suenaga, S. W. Kim, Y. H. Lee, H. Yang, *Science*, 2015, **349**, 625-628.
52. A. Y. Lu, H. Zhu, J. Xiao, C. P. Chuu, Y. Han, M. H. Chiu, C. C. Cheng, C. W. Yang, K. H. Wei, Y. Yang, Y. Wang, D. Sokaras, D. Nordlund, P. Yang, D. A. Muller, M. Y. Chou, X. Zhang, L. J. Li, *Nat. Nanotechnol.*, 2017, **12**, 744-749.
53. J. Zhang, S. Jia, I. Kholmanov, L. Dong, D. Er, W. Chen, H. Guo, Z. Jin, V. B. Shenoy, L. Shi, J. Lou, *ACS Nano*, 2017, **11**, 8192-8198.
54. H. Liu, N. Han, J. Zhao, *RSC Adv.*, 2015, **5**, 17572-17581.
55. S. S. Chou, M. De, J. Kim, S. Byun, C. Dykstra, J. Yu, J. Huang, V. P. Dravid, *J. Am. Chem. Soc.*, 2013, **135**, 4584-4587.
56. W. Zhou, X. Zou, S. Najmaei, Z. Liu, Y. Shi, J. Kong, J. Lou, P. M. Ajayan, B. I.

- Yakobson, J.-C. Idrobo, *Nano Lett.*, 2013, **13**, 2615-2622.
57. J. Hong, Z. Hu, M. Probert, K. Li, D. Lv, X. Yang, L. Gu, N. Mao, Q. Feng, L. Xie, J. Zhang, D. Wu, Z. Zhang, C. Jin, W. Ji, X. Zhang, J. Yuan, Z. Zhang, *Nat. Commun.*, 2015, **6**, 6293.
58. Y. Tong, Y. Guo, K. Mu, H. Shan, J. Dai, Y. Liu, Z. Sun, A. Zhao, X. C. Zeng, C. Wu, Y. Xie, *Adv. Mater.*, 2017, **29**, 1703123.
59. M. K. Jaiswal, J. K. Carrow, J. L. Gentry, J. Gupta, N. Altangerel, M. Scully, A. K. Gaharwar, *Adv. Mater.*, 2017, **29**, 1702037.
60. J. Feng, M. Graf, K. Liu, D. Ovchinnikov, D. Dumcenco, M. Heiranian, V. Nandigana, N. R. Aluru, A. Kis, A. Radenovic, *Nature*, 2016, **536**, 197-200.
61. J. Feng, K. Liu, R. D. Bulushev, S. Khlybov, D. Dumcenco, A. Kis, A. Radenovic, *Nat. Nanotechnol.*, 2015, **10**, 1070-1076.
62. C. C. Cheng, A. Y. Lu, C. C. Tseng, X. L. Yang, M. N. Hedhili, M. C. Chen, K. H. Wei, L. J. Li, *Nano Energy*, 2016, **30**, 846-852.
63. H. Li, C. Tsai, A. L. Koh, L. Cai, A. W. Contryman, A. H. Fragapane, J. Zhao, H. S. Han, H. C. Manoharan, F. Abild-Pedersen, J. K. Nørskov, X. Zheng, *Nat. Mater.*, 2016, **15**, 48-53.
64. M. Liu, J. Shi, Y. Li, X. Zhou, D. Ma, Y. Qi, Y. Zhang, Z. Liu, *Small*, 2017, **13**, 1602967.
65. C. Tsai, H. Li, S. Park, J. Park, H. S. Han, J. K. Nørskov, X. Zheng, F. Abild-Pedersen, *Nat. Commun.*, 2017, **8**, 15113.
66. S. Tongay, J. Suh, C. Ataca, W. Fan, A. Luce, J. S. Kang, J. Liu, C. Ko, R. Raghunathanan, J. Zhou, F. Ogletree, J. Li, J. C. Grossman, J. Wu, *Sci. Rep.*,

- 2013, **3**, 2657.
67. S. Mignuzzi, A. J. Pollard, N. Bonini, B. Brennan, I. S. Gilmore, M. A. Pimenta, D. Richards, D. Roy, *Phys. Rev. B*, 2015, **91**, 195411.
68. T.-Y. Kim, K. Cho, W. Park, J. Park, Y. Song, S. Hong, W.-K. Hong, T. Lee, *ACS Nano*, 2014, **8**, 2774-2781.
69. M. Yamamoto, S. Dutta, S. Aikawa, S. Nakaharai, K. Wakabayashi, M. S. Fuhrer, K. Ueno, K. Tsukagoshi, *Nano Lett.*, 2015, **15**, 2067-2073.
70. H.-P. Komsa, J. Kotakoski, S. Kurasch, O. Lehtinen, U. Kaiser, A. V. Krasheninnikov, *Phys. Rev. Lett.*, 2012, **109**, 035503.
71. S. Wang, H. Li, H. Sawada, C. S. Allen, A. I. Kirkland, J. C. Grossman, J. H. Warner, *Nanoscale*, 2017, **9**, 6417-6426.
72. K. Liu, J. Feng, A. Kis, A. Radenovic, *ACS Nano*, 2014, **8**, 2504-2511.
73. M. Heiranian, A. B. Farimani, N. R. Aluru, *Nat. Commun.*, 2015, **6**, 8616.
74. H. Li, Y. W. Tan, P. Liu, C. G. Guo, M. Luo, J. H. Han, T. Q. Lin, F. Q. Huang, M. W. Chen, *Adv. Mater.*, 2016, **28**, 8945-8949.
75. J. Min Hwan, A. Chisung, U. K. Hyeong, K. Kyong Nam, N. Tai Zhe Li, Q. Hongyi, K. Yeongseok, L. Sehan, K. Taesung, Y. Geun Young, *Nanotechnology*, 2015, **26**, 355706.
76. M. Chen, H. Nam, S. Wi, G. Priessnitz, I. M. Gunawan, X. Liang, *ACS Nano*, 2014, **8**, 4023-4032.
77. A. A. Tedstone, D. J. Lewis, P. O'Brien, *Chem. Mater.*, 2016, **28**, 1965-1974.
78. J. Suh, T.-E. Park, D.-Y. Lin, D. Fu, J. Park, H. J. Jung, Y. Chen, C. Ko, C. Jang, Y. Sun, R. Sinclair, J. Chang, S. Tongay, J. Wu, *Nano Lett.*, 2014, **14**, 6976-6982.

79. G. Liu, A. W. Robertson, M. M.-J. Li, W. C. H. Kuo, M. T. Darby, M. H. Muhieddine, Y.-C. Lin, K. Suenaga, M. Stamatakis, J. H. Warner, S. C. E. Tsang, *Nat. Chem.*, 2017, **9**, 810-816.
80. H. Tan, W. Hu, C. Wang, C. Ma, H. Duan, W. Yan, L. Cai, P. Guo, Z. Sun, Q. Liu, X. Zheng, F. Hu, S. Wei, *Small*, 2017, **13**, 1701389.
81. K. Zhang, S. Feng, J. Wang, A. Azcatl, N. Lu, R. Addou, N. Wang, C. Zhou, J. Lerach, V. Bojan, M. J. Kim, L.-Q. Chen, R. M. Wallace, M. Terrones, J. Zhu, J. A. Robinson, *Nano Lett.*, 2015, **15**, 6586-6591.
82. G. Bai, S. Yuan, Y. Zhao, Z. Yang, S. Y. Choi, Y. Chai, S. F. Yu, S. P. Lau, J. Hao, *Adv. Mater.*, 2016, **28**, 7472-7477.
83. A. W. Robertson, Y.-C. Lin, S. Wang, H. Sawada, C. S. Allen, Q. Chen, S. Lee, G.-D. Lee, J. Lee, S. Han, E. Yoon, A. I. Kirkland, H. Kim, K. Suenaga, J. H. Warner, *ACS Nano*, 2016, **10**, 10227-10236.
84. J. Deng, H. Li, J. Xiao, Y. Tu, D. Deng, H. Yang, H. Tian, J. Li, P. Ren, X. Bao, *Energy Environ. Sci.*, 2015, **8**, 1594-1601.
85. Y.-C. Lin, D. O. Dumcenco, H.-P. Komsa, Y. Niimi, A. V. Krasheninnikov, Y.-S. Huang, K. Suenaga, *Adv. Mater.*, 2014, **26**, 2857-2861.
86. D. J. Lewis, A. A. Tedstone, X. L. Zhong, E. A. Lewis, A. Rooney, N. Savjani, J. R. Brent, S. J. Haigh, M. G. Burke, C. A. Muryn, J. M. Raftery, C. Warrens, K. West, S. Gaemers, P. O'Brien, *Chem. Mater.*, 2015, **27**, 1367-1374.
87. L. Cheng, C. Yuan, S. Shen, X. Yi, H. Gong, K. Yang, Z. Liu, *ACS Nano*, 2015, **9**, 11090-11101.
88. Y. Chen, J. Xi, D. O. Dumcenco, Z. Liu, K. Suenaga, D. Wang, Z. Shuai, Y.-S.

- Huang, L. Xie, *ACS Nano*, 2013, **7**, 4610-4616.
89. Y. Chen, D. O. Dumcenco, Y. Zhu, X. Zhang, N. Mao, Q. Feng, M. Zhang, J. Zhang, P.-H. Tan, Y.-S. Huang, L. Xie, *Nanoscale*, 2014, **6**, 2833-2839.
90. J.-S. Kim, S. T. Moran, A. P. Nayak, S. Pedahzur, I. Ruiz, G. Ponce, D. Rodriguez, J. Henny, J. Liu, J.-F. Lin, D. Akinwande, *2D Mater.*, 2016, **3**, 025003.
91. H. Liu, K. K. A. Antwi, S. Chua, D. Chi, *Nanoscale*, 2014, **6**, 624-629.
92. W. Zhang, X. Li, T. Jiang, J. Song, Y. Lin, L. Zhu, X. Xu, *Nanoscale*, 2015, **7**, 13554-13560.
93. X. Li, A. A. Puretzky, X. Sang, S. Kc, M. Tian, F. Ceballos, M. Mahjouri-Samani, K. Wang, R. R. Unocic, H. Zhao, G. Duscher, V. R. Cooper, C. M. Rouleau, D. B. Geohegan, K. Xiao, *Adv. Funct. Mater.*, 2017, **27**, 1603850.
94. X. Liu, J. Wu, W. Yu, L. Chen, Z. Huang, H. Jiang, J. He, Q. Liu, Y. Lu, D. Zhu, W. Liu, P. Cao, S. Han, X. Xiong, W. Xu, J.-P. Ao, K.-W. Ang, Z. He, *Adv. Funct. Mater.*, 2017, **27**, 1606469.
95. Z. Wang, P. Liu, Y. Ito, S. Ning, Y. Tan, T. Fujita, A. Hirata, M. Chen, *Sci. Rep.*, 2016, **6**, 21536.
96. C. Tan, W. Zhao, A. Chaturvedi, Z. Fei, Z. Zeng, J. Chen, Y. Huang, P. Ercius, Z. Luo, X. Qi, B. Chen, Z. Lai, B. Li, X. Zhang, J. Yang, Y. Zong, C. Jin, H. Zheng, C. Kloc, H. Zhang, *Small*, 2016, **12**, 1866-1874.
97. K. Yang, X. Wang, H. Li, B. Chen, X. Zhang, S. Li, N. Wang, H. Zhang, X. Huang, W. Huang, *Nanoscale*, 2017, **9**, 5102-5109.
98. Y. Gong, Z. Liu, A. R. Lupini, G. Shi, J. Lin, S. Najmaei, Z. Lin, A. L. Elías, A.

- Berkdemir, G. You, H. Terrones, M. Terrones, R. Vajtai, S. T. Pantelides, S. J. Pennycook, J. Lou, W. Zhou, P. M. Ajayan, *Nano Lett.*, 2014, **14**, 442-449.
99. H. L. Li, X. D. Duan, X. P. Wu, X. J. Zhuang, H. Zhou, Q. L. Zhang, X. L. Zhu, W. Hu, P. Y. Ren, P. F. Guo, L. Ma, X. P. Fan, X. X. Wang, J. Y. Xu, A. L. Pan, X. F. Duan, *J. Am. Chem. Soc.*, 2014, **136**, 3756-3759.
100. Q. Fu, L. Yang, W. Wang, A. Han, J. Huang, P. Du, Z. Fan, J. Zhang, B. Xiang, *Adv. Mater.*, 2015, **27**, 4732-4738.
101. X. D. Duan, C. Wang, Z. Fan, G. L. Hao, L. Z. Kou, U. Halim, H. L. Li, X. P. Wu, Y. C. Wang, J. H. Jiang, A. L. Pan, Y. Huang, R. Q. Yu, X. F. Duan, *Nano Lett.*, 2016, **16**, 264-269.
102. Q. Ma, M. Isarraraz, C. S. Wang, E. Preciado, V. Klee, S. Bobek, K. Yamaguchi, E. Li, P. M. Odenthal, A. Nguyen, D. Barroso, D. Sun, G. von Son Palacio, M. Gomez, A. Nguyen, D. Le, G. Pawin, J. Mann, T. F. Heinz, T. S. Rahman, L. Bartels, *ACS Nano*, 2014, **8**, 4672-4677.
103. J. Mann, Q. Ma, P. M. Odenthal, M. Isarraraz, D. Le, E. Preciado, D. Barroso, K. Yamaguchi, G. von Son Palacio, A. Nguyen, T. Tran, M. Wurch, A. Nguyen, V. Klee, S. Bobek, D. Sun, T. F. Heinz, T. S. Rahman, R. Kawakami, L. Bartels, *Adv. Mater.*, 2014, **26**, 1399-1404.
104. Q. Gong, L. Cheng, C. Liu, M. Zhang, Q. Feng, H. Ye, M. Zeng, L. Xie, Z. Liu, Y. Li, *ACS Catal.*, 2015, **5**, 2213-2219.
105. J. Xu, X. Li, W. Liu, Y. Sun, Z. Ju, T. Yao, C. Wang, H. Ju, J. Zhu, S. Wei, Y. Xie, *Angew. Chem. Int. Ed.*, 2017, **56**, 9121-9125.
106. W. Wen, Y. Zhu, X. Liu, H.-P. Hsu, Z. Fei, Y. Chen, X. Wang, M. Zhang, K.-H.

- Lin, F.-S. Huang, Y.-P. Wang, Y.-S. Huang, C.-H. Ho, P.-H. Tan, C. Jin, L. Xie, *Small*, 2017, **13**, 1603788.
107. Z. Yang, H. Liang, X. Wang, X. Ma, T. Zhang, Y. Yang, L. Xie, D. Chen, Y. Long, J. Chen, Y. Chang, C. Yan, X. Zhang, X. Zhang, B. Ge, Z. Ren, M. Xue, G. Chen, *ACS Nano*, 2016, **10**, 755-762.
108. S. Susarla, A. Kutana, J. A. Hachtel, V. Kochat, A. Apte, R. Vajtai, J. C. Idrobo, B. I. Yakobson, C. S. Tiwary, P. M. Ajayan, *Adv. Mater.*, 2017, **29**, 1702457.
109. P. Yu, J. H. Lin, L. F. Sun, Q. L. Le, X. C. Yu, G. H. Gao, C. H. Hsu, D. Wu, T. R. Chang, Q. S. Zeng, F. C. Liu, Q. J. Wang, H. T. Jeng, H. Lin, A. Trampert, Z. X. Shen, K. Suenaga, Z. Liu, *Adv. Mater.*, 2017, **29**, 1603991.
110. J. Lin, J. Zhou, S. Zuluaga, P. Yu, M. Gu, Z. Liu, S. T. Pantelides, K. Suenaga, *ACS Nano*, 2018, **12**, 894-901.
111. D. Rhodes, D. A. Chenet, B. E. Janicek, C. Nyby, Y. Lin, W. Jin, D. Edelberg, E. Mannebach, N. Finney, A. Antony, T. Schiros, T. Klarr, A. Mazzoni, M. Chin, Y. C. Chiu, W. Zheng, Q. R. Zhang, F. Ernst, J. I. Dadayp, X. Tong, J. Ma, R. Lou, S. Wan, T. Qian, H. Ding, R. M. Osgood, D. W. Paley, A. M. Lindenberg, P. Y. Huang, A. N. Pasupathy, M. Dubey, J. Hone, L. Balicas, *Nano Lett.*, 2017, **17**, 1616-1622.
112. C. X. Zhang, K. C. Santosh, Y. F. Nie, C. P. Liang, W. G. Vandenberghe, R. C. Longo, Y. P. Zheng, F. T. Kong, S. Hong, R. M. Wallace, K. Cho, *ACS Nano*, 2016, **10**, 7370-7375.
113. H. X. Luo, W. W. Xie, J. Tao, I. Pletikosic, T. Valla, G. S. Sahasrabudhe, G. Osterhoudt, E. Sutton, K. S. Burch, E. M. Seibel, J. W. Krizan, Y. M. Zhu, R. J.

- Cava, *Chem. Mater.*, 2016, **28**, 1927-1935.
114. A. R. Kim, Y. Kim, J. Nam, H.-S. Chung, D. J. Kim, J.-D. Kwon, S. W. Park, J. Park, S. Y. Choi, B. H. Lee, J. H. Park, K. H. Lee, D.-H. Kim, S. M. Choi, P. M. Ajayan, M. G. Hahm, B. Cho, *Nano Lett.*, 2016, **16**, 1890-1895.
115. W. Choi, N. Choudhary, G. H. Han, J. Park, D. Akinwande, Y. H. Lee, *Mater. Today*, 2017, **20**, 116-130.
116. M. Acerce, D. Voiry, M. Chhowalla, *Nat. Nanotechnol.*, 2015, **10**, 313-318.
117. M. Kan, J. Y. Wang, X. W. Li, S. H. Zhang, Y. W. Li, Y. Kawazoe, Q. Sun, P. Jena, *J. Phys. Chem. C*, 2014, **118**, 1515-1522.
118. S. Tongay, H. Sahin, C. Ko, A. Luce, W. Fan, K. Liu, J. Zhou, Y.-S. Huang, C.-H. Ho, J. Yan, D. F. Ogletree, S. Aloni, J. Ji, S. Li, J. Li, F. M. Peeters, J. Wu, *Nat. Commun.*, 2014, **5**, 3252.
119. J. Peng, J. Wu, X. Li, Y. Zhou, Z. Yu, Y. Guo, J. Wu, Y. Lin, Z. Li, X. Wu, C. Wu, Y. Xie, *J. Am. Chem. Soc.*, 2017, **139**, 9019-9025.
120. D. H. Keum, S. Cho, J. H. Kim, D.-H. Choe, H.-J. Sung, M. Kan, H. Kang, J.-Y. Hwang, S. W. Kim, H. Yang, K. J. Chang, Y. H. Lee, *Nat. Phys.*, 2015, **11**, 482-486.
121. X. L. Ma, P. J. Guo, C. J. Yi, Q. H. Yu, A. M. Zhang, J. T. Ji, Y. Tian, F. Jin, Y. Y. Wang, K. Liu, T. L. Xia, Y. G. Shi, Q. M. Zhang, *Phys. Rev. B*, 2016, **94**, 214105.
122. R. He, J. van Baren, J. A. Yan, X. X. Xi, Z. P. Ye, G. H. Ye, I. H. Lu, S. M. Leong, C. H. Lui, *2D Mater.*, 2016, **3**, 031008.
123. R. Zhao, Y. Wang, D. Deng, X. Luo, W. J. Lu, Y.-P. Sun, Z.-K. Liu, L.-Q. Chen,

- J. Robinson, *Nano Lett.*, 2017, **17**, 3471-3477.
124. L. Hart, S. Dale, S. Hoye, J. L. Webb, D. Wolverson, *Nano Lett.*, 2016, **16**, 1381-1386.
125. D. Ovchinnikov, F. Gargiulo, A. Allain, D. J. Pasquier, D. Dumcenco, C. H. Ho, O. V. Yazyev, A. Kis, *Nat. Commun.*, 2016, **7**, 12391.
126. D. A. Chenet, O. B. Aslan, P. Y. Huang, C. Fan, A. M. van der Zande, T. F. Heinz, J. C. Hone, *Nano Lett.*, 2015, **15**, 5667-5672.
127. P. Yu, W. Fu, Q. Zeng, J. Lin, C. Yan, Z. Lai, B. Tang, K. Suenaga, H. Zhang, Z. Liu, *Adv. Mater.*, 2017, **29**, 1701909.
128. J. Gao, L. Li, J. Tan, H. Sun, B. Li, J. C. Idrobo, C. V. Singh, T.-M. Lu, N. Koratkar, *Nano Lett.*, 2016, **16**, 3780-3787.
129. J. C. Park, S. J. Yun, H. Kim, J. H. Park, S. H. Chae, S. J. An, J. G. Kim, S. M. Kim, K. K. Kim, Y. H. Lee, *ACS Nano*, 2015, **9**, 6548-6554.
130. L. Zhou, K. Xu, A. Zubair, A. D. Liao, W. J. Fang, F. P. Ouyang, Y. H. Lee, K. Ueno, R. Saito, T. Palacios, J. Kong, M. S. Dresselhaus, *J. Am. Chem. Soc.*, 2015, **137**, 11892-11895.
131. L. Zhou, A. Zubair, Z. Q. Wang, X. Zhang, F. P. Ouyang, K. Xu, W. J. Fang, K. Ueno, J. Li, T. Palacios, J. Kong, M. S. Dresselhaus, *Adv. Mater.*, 2016, **28**, 9526.
132. L. Fu, F. Wang, B. Wu, N. Wu, W. Huang, H. Wang, C. Jin, L. Zhuang, J. He, L. Fu, Y. Liu, *Adv. Mater.*, 2017, **29**, 1700439.
133. J. Zhou, F. Liu, J. Lin, X. Huang, J. Xia, B. Zhang, Q. Zeng, H. Wang, C. Zhu, L. Niu, X. Wang, W. Fu, P. Yu, T.-R. Chang, C.-H. Hsu, D. Wu, H.-T. Jeng, Y. Huang, H. Lin, Z. Shen, C. Yang, L. Lu, K. Suenaga, W. Zhou, S. T. Pantelides,

- G. Liu, Z. Liu, *Adv. Mater.*, 2017, **29**, 1603471.
134. Q. Zhang, Y. Xiao, T. Zhang, Z. Weng, M. Zeng, S. Yue, R. G. Mendes, L. Wang, S. Chen, M. H. Rümmeli, L. Peng, L. Fu, *Chem. Mater.*, 2017, **29**, 4641-4644.
135. C. H. Naylor, W. M. Parkin, J. L. Ping, Z. L. Gao, Y. R. Zhou, Y. Kim, F. Streller, R. W. Carpick, A. M. Rappe, M. Drndic, J. M. Kikkawa, A. T. C. Johnson, *Nano Lett.*, 2016, **16**, 4297-4304.
136. H. N. Carl, M. P. William, G. Zhaoli, K. Hojin, N. Mehmet, B. W. Robert, Z. T. Liang, K. Youngkuk, E. K. Christopher, S. Frank, Z. Yu Ren, C. Robert, L. Zhengtang, P. Yung Woo, M. R. Andrew, D. Marija, M. K. James, A. T. C. Johnson, *2D Mater.*, 2017, **4**, 021008.
137. K. Chen, Z. Chen, X. Wan, Z. Zheng, F. Xie, W. Chen, X. Gui, H. Chen, W. Xie, J. Xu, *Adv. Mater.*, 2017, **29**, 1700704.
138. Y. F. Sun, Y. X. Wang, D. Sun, B. R. Carvalho, C. G. Read, C. H. Lee, Z. Lin, K. Fujisawa, J. A. Robinson, V. H. Crespi, M. Terrones, R. E. Schaak, *Angew. Chem. Int. Ed.*, 2016, **55**, 2830-2834.
139. K. K. Amara, Y. Chen, Y.-C. Lin, R. Kumar, E. Okunishi, K. Suenaga, S. Y. Quek, G. Eda, *Chem. Mater.*, 2016, **28**, 2308-2314.
140. Y.-C. Lin, D. O. Dumcenco, Y.-S. Huang, K. Suenaga, *Nat. Nanotechnol.*, 2014, **9**, 391-396.
141. Y. Kang, S. Najmaei, Z. Liu, Y. Bao, Y. Wang, X. Zhu, N. J. Halas, P. Nordlander, P. M. Ajayan, J. Lou, Z. Fang, *Adv. Mater.*, 2014, **26**, 6467-6471.
142. S. Song, D. H. Keum, S. Cho, D. Perello, Y. Kim, Y. H. Lee, *Nano Lett.*, 2016,

- 16**, 188-193.
143. G. Eda, H. Yamaguchi, D. Voiry, T. Fujita, M. Chen, M. Chhowalla, *Nano Lett.*, 2011, **11**, 5111-5116.
144. J. Xia, D.-F. Li, J.-D. Zhou, P. Yu, J.-H. Lin, J.-L. Kuo, H.-B. Li, Z. Liu, J.-X. Yan, Z.-X. Shen, *Small*, 2017, **13**, 1701887.
145. A. P. Nayak, S. Bhattacharyya, J. Zhu, J. Liu, X. Wu, T. Pandey, C. Jin, A. K. Singh, D. Akinwande, J.-F. Lin, *Nat. Commun.*, 2014, **5**, 3731.
146. Y. Wang, J. Xiao, H. Zhu, Y. Li, Y. Alsaad, K. Y. Fong, Y. Zhou, S. Wang, W. Shi, Y. Wang, A. Zettl, E. J. Reed, X. Zhang, *Nature*, 2017, **550**, 487–491.
147. M. A. Py, R. R. Haering, *Can. J. Phys.*, 1983, **61**, 76-84.
148. G. Eda, T. Fujita, H. Yamaguchi, D. Voiry, M. Chen, M. Chhowalla, *ACS Nano*, 2012, **6**, 7311-7317.
149. D. Voiry, H. Yamaguchi, J. Li, R. Silva, D. C. B. Alves, T. Fujita, M. Chen, T. Asefa, V. B. Shenoy, G. Eda, M. Chhowalla, *Nat. Mater.*, 2013, **12**, 850-855.
150. J. Zheng, H. Zhang, S. H. Dong, Y. P. Liu, C. T. Nai, H. S. Shin, H. Y. Jeong, B. Liu, K. P. Loh, *Nat. Commun.*, 2014, **5**, 2995.
151. D. Voiry, M. Salehi, R. Silva, T. Fujita, M. Chen, T. Asefa, V. B. Shenoy, G. Eda, M. Chhowalla, *Nano Lett.*, 2013, **13**, 6222-6227.
152. Y. Yin, J. Han, Y. Zhang, X. Zhang, P. Xu, Q. Yuan, L. Samad, X. Wang, Y. Wang, Z. Zhang, P. Zhang, X. Cao, B. Song, S. Jin, *J. Am. Chem. Soc.*, 2016, **138**, 7965-7972.
153. S. J. R. Tan, I. Abdelwahab, Z. Ding, X. Zhao, T. Yang, G. Z. J. Loke, H. Lin, I. Verzhbitskiy, S. M. Poh, H. Xu, C. T. Nai, W. Zhou, G. Eda, B. Jia, K. P. Loh, *J.*

- Am. Chem. Soc.*, 2017, **139**, 2504-2511.
154. X. Huang, Z. Zeng, S. Bao, M. Wang, X. Qi, Z. Fan, H. Zhang, *Nat. Commun.*, 2013, **4**, 1444.
155. Z. Zeng, C. Tan, X. Huang, S. Bao, H. Zhang, *Energy Environ. Sci.*, 2014, **7**, 797-803.
156. H. Wang, Z. Lu, S. Xu, D. Kong, J. J. Cha, G. Zheng, P.-C. Hsu, K. Yan, D. Bradshaw, F. B. Prinz, Y. Cui, *Proc. Natl. Acad. Sci. USA*, 2013, **110**, 19701-19706.
157. K. He, C. Poole, K. F. Mak, J. Shan, *Nano Lett.*, 2013, **13**, 2931-2936.
158. P. Johari, V. B. Shenoy, *ACS Nano*, 2012, **6**, 5449-5456.
159. S. Manzeli, A. Allain, A. Ghadimi, A. Kis, *Nano Lett.*, 2015, **15**, 5330-5335.
160. K.-A. N. Duerloo, Y. Li, E. J. Reed, *Nat. Commun.*, 2014, **5**, 4214.
161. J. Zhu, Z. Wang, H. Yu, N. Li, J. Zhang, J. Meng, M. Liao, J. Zhao, X. Lu, L. Du, R. Yang, D. Shi, Y. Jiang, G. Zhang, *J. Am. Chem. Soc.*, 2017, **139**, 10216-10219.
162. A. K. Geim, I. V. Grigorieva, *Nature*, 2013, **499**, 419-425.
163. K. Ray, A. E. Yore, T. Mou, S. Jha, K. K. H. Smithe, B. Wang, E. Pop, A. K. M. Newaz, *ACS Nano*, 2017, **11**, 6024-6030.
164. A. J. Molina-Mendoza, E. Giovanelli, W. S. Paz, M. A. Niño, J. O. Island, C. Evangelisti, L. Aballe, M. Foerster, H. S. J. van der Zant, G. Rubio-Bollinger, N. Agraït, J. J. Palacios, E. M. Pérez, A. Castellanos-Gómez, *Nat. Commun.*, 2017, **8**, 14409.
165. M. Velický, P. S. Toth, A. M. Rakowski, A. P. Rooney, A. Kozikov, C. R. Woods, A. Mishchenko, L. Fumagalli, J. Yin, V. Zólyomi, T. Georgiou, S. J.

- Haigh, K. S. Novoselov, R. A. W. Dryfe, *Nat. Commun.*, 2017, **8**, 14410.
166. X. Li, L. Basile, B. Huang, C. Ma, J. Lee, I. V. Vlassiouk, A. A. Puretzky, M.-W. Lin, M. Yoon, M. Chi, J. C. Idrobo, C. M. Rouleau, B. G. Sumpter, D. B. Geohegan, K. Xiao, *ACS Nano*, 2015, **9**, 8078-8088.
167. J. A. Miwa, M. Dendzik, S. S. Grønborg, M. Bianchi, J. V. Lauritsen, P. Hofmann, S. Ulstrup, *ACS Nano*, 2015, **9**, 6502-6510.
168. Y.-C. Lin, N. Lu, N. Perea-Lopez, J. Li, Z. Lin, X. Peng, C. H. Lee, C. Sun, L. Calderin, P. N. Browning, M. S. Bresnehan, M. J. Kim, T. S. Mayer, M. Terrones, J. A. Robinson, *ACS Nano*, 2014, **8**, 3715-3723.
169. Y. Shi, W. Zhou, A.-Y. Lu, W. Fang, Y.-H. Lee, A. L. Hsu, S. M. Kim, K. K. Kim, H. Y. Yang, L.-J. Li, J.-C. Idrobo, J. Kong, *Nano Lett.*, 2012, **12**, 2784-2791.
170. A. Yan, J. Velasco, S. Kahn, K. Watanabe, T. Taniguchi, F. Wang, M. F. Crommie, A. Zettl, *Nano Lett.*, 2015, **15**, 6324-6331.
171. S. Wang, X. Wang, J. H. Warner, *ACS Nano*, 2015, **9**, 5246-5254.
172. M. Cattelan, B. Markman, G. Lucchini, P. K. Das, I. Vobornik, J. A. Robinson, S. Agnoli, G. Granozzi, *Chem. Mater.*, 2015, **27**, 4105-4113.
173. T. Zhang, B. Jiang, Z. Xu, R. G. Mendes, Y. Xiao, L. F. Chen, L. W. Fang, T. Gemming, S. L. Chen, M. H. Rummeli, L. Fu, *Nat. Commun.*, 2016, **7**, 13911.
174. D. Horacio Coy, C. Redhouane, M. Yujing, B. Matthias, *2D Mater.*, 2015, **2**, 044010.
175. Y. J. Gong, J. H. Lin, X. L. Wang, G. Shi, S. D. Lei, Z. Lin, X. L. Zou, G. L. Ye, R. Vajtai, B. I. Yakobson, H. Terrones, M. Terrones, Beng K. Tay, J. Lou, S. T.

- Pantelides, Z. Liu, W. Zhou, P. M. Ajayan, *Nat. Mater.*, 2014, **13**, 1135-1142.
176. K. E. Aretouli, P. Tsipas, D. Tsoutsou, J. Marquez-Velasco, E. Xenogiannopoulou, S. A. Giamini, E. Vassalou, N. Kelaidis, A. Dimoulas, *Appl. Phys. Lett.*, 2015, **106**, 143105.
177. Z. Xing, Z. Nan, L. Chao, S. Hongyue, Z. Qi, H. Xiaozong, G. Lin, L. Huiqiao, L. Jingtao, L. Jun, X. Jie, Z. Tianyou, *2D Mater.*, 2017, **4**, 025048.
178. X. Li, M.-W. Lin, J. Lin, B. Huang, A. A. Puretzky, C. Ma, K. Wang, W. Zhou, S. T. Pantelides, M. Chi, I. Kravchenko, J. Fowlkes, C. M. Rouleau, D. B. Geohegan, K. Xiao, *Sci. Adv.*, 2016, **2**, e1501882.
179. R. Q. Ai, X. Guan, J. Li, K. K. Yao, P. Chen, Z. W. Zhang, X. D. Duan, X. F. Duan, *ACS Nano*, 2017, **11**, 3413-3419.
180. J. Li, X. Guan, C. Wang, H.-C. Cheng, R. Ai, K. Yao, P. Chen, Z. Zhang, X. Duan, X. Duan, *Small*, 2017, **13**, 1701034.
181. M. B. Alemayehu, M. Falmbigl, K. Ta, J. Ditto, D. L. Medlin, D. C. Johnson, *Angew. Chem. Int. Ed.*, 2015, **54**, 15468-15472.
182. Y.-C. Lin, R. K. Ghosh, R. Addou, N. Lu, S. M. Eichfeld, H. Zhu, M.-Y. Li, X. Peng, M. J. Kim, L.-J. Li, R. M. Wallace, S. Datta, J. A. Robinson, *Nat. Commun.*, 2015, **6**, 7311.
183. J. Shi, R. Tong, X. Zhou, Y. Gong, Z. Zhang, Q. Ji, Y. Zhang, Q. Fang, L. Gu, X. Wang, Z. Liu, Y. Zhang, *Adv. Mater.*, 2016, **28**, 10664-10672.
184. Y. J. Gong, S. D. Lei, G. L. Ye, B. Li, Y. M. He, K. Keyshar, X. Zhang, Q. Z. Wang, J. Lou, Z. Liu, R. Vajtai, W. Zhou, P. M. Ajayan, *Nano Lett.*, 2015, **15**, 6135-6141.

185. C. Huang, S. Wu, A. M. Sanchez, J. J. P. Peters, R. Beanland, J. S. Ross, P. Rivera, W. Yao, D. H. Cobden, X. Xu, *Nat. Mater.*, 2014, **13**, 1096-1101.
186. C. H. Naylor, W. M. Parkin, Z. Gao, J. Berry, S. Zhou, Q. Zhang, J. B. McClimon, L. Z. Tan, C. E. Kehayias, M.-Q. Zhao, R. S. Gona, R. W. Carpick, A. M. Rappe, D. J. Srolovitz, M. Drndic, A. T. C. Johnson, *ACS Nano*, 2017, **11**, 8619-8627.
187. F. Ullah, Y. Sim, C. T. Le, M.-J. Seong, J. I. Jang, S. H. Rhim, B. C. Tran Khac, K.-H. Chung, K. Park, Y. Lee, K. Kim, H. Y. Jeong, Y. S. Kim, *ACS Nano*, 2017, **11**, 8822-8829.
188. X. Duan, C. Wang, J. C. Shaw, R. Cheng, Y. Chen, H. Li, X. Wu, Y. Tang, Q. Zhang, A. Pan, J. Jiang, R. Yu, Y. Huang, X. Duan, *Nat. Nanotechnol.*, 2014, **9**, 1024-1030.
189. M.-Y. Li, Y. Shi, C.-C. Cheng, L.-S. Lu, Y.-C. Lin, H.-L. Tang, M.-L. Tsai, C.-W. Chu, K.-H. Wei, J.-H. He, W.-H. Chang, K. Suenaga, L.-J. Li, *Science*, 2015, **349**, 524-528.
190. M.-L. Tsai, M.-Y. Li, J. R. D. Retamal, K.-T. Lam, Y.-C. Lin, K. Suenaga, L.-J. Chen, G. Liang, L.-J. Li, J.-H. He, *Adv. Mater.*, 2017, **29**, 1701168.
191. Y. Yoo, Z. P. Degregorio, J. E. Johns, *J. Am. Chem. Soc.*, 2015, **137**, 14281-14287.
192. K. Bogaert, S. Liu, J. Chasin, D. Titow, S. Gradecak, S. Garaj, *Nano Lett.*, 2016, **16**, 5129-5134.
193. H. L. Li, X. P. Wu, H. J. Liu, B. Y. Zheng, Q. L. Zhang, X. L. Zhu, Z. We, X. J. Zhuang, H. Zhou, W. X. Tang, X. F. Duan, A. L. Pan, *ACS Nano*, 2017, **11**, 961-

- 967.
194. Y. Tsai, Z. Chu, Y. Han, C.-P. Chuu, D. Wu, A. Johnson, F. Cheng, M.-Y. Chou, D. A. Muller, X. Li, K. Lai, C.-K. Shih, *Adv. Mater.*, 2017, **29**, 1703680.
195. M. Mahjouri-Samani, M.-W. Lin, K. Wang, A. R. Lupini, J. Lee, L. Basile, A. Boulesbaa, C. M. Rouleau, A. A. Puretzky, I. N. Ivanov, K. Xiao, M. Yoon, D. B. Geohegan, *Nat. Commun.*, 2015, **6**, 7749.
196. H. N. Li, P. Li, J. K. Huang, M. Y. Li, C. W. Yang, Y. M. Shi, X. X. Zhang, L. J. Li, *ACS Nano*, 2016, **10**, 10516-10523.
197. X. Ling, Y. Lin, Q. Ma, Z. Wang, Y. Song, L. Yu, S. Huang, W. Fang, X. Zhang, A. L. Hsu, Y. Bie, Y.-H. Lee, Y. Zhu, L. Wu, J. Li, P. Jarillo-Herrero, M. Dresselhaus, T. Palacios, J. Kong, *Adv. Mater.*, 2016, **28**, 2322-2329.
198. R. Ganatra, Q. Zhang, *ACS Nano*, 2014, **8**, 4074-4099.
199. D. Jariwala, V. K. Sangwan, L. J. Lauhon, T. J. Marks, M. C. Hersam, *ACS Nano*, 2014, **8**, 1102-1120.
200. J. Xu, L. Chen, Y.-W. Dai, Q. Cao, Q.-Q. Sun, S.-J. Ding, H. Zhu, D. W. Zhang, *Sci. Adv.*, 2017, **3**, e1602246.
201. K. Chen, X. Wan, J. X. Wen, W. G. Xie, Z. W. Kang, X. L. Zeng, H. J. Chen, J. B. Xu, *ACS Nano*, 2015, **9**, 9868-9876.
202. C. L. Wan, X. K. Gu, F. Dang, T. Itoh, Y. F. Wang, H. Sasaki, M. Kondo, K. Koga, K. Yabuki, G. J. Snyder, R. G. Yang, K. Koumoto, *Nat. Mater.*, 2015, **14**, 622-627.
203. H. H. Huang, Y. Cui, Q. Li, C. C. Dun, W. Zhou, W. X. Huang, L. Chen, C. A. Hewitt, D. L. Carroll, *Nano Energy*, 2016, **26**, 172-179.

204. R. M. Tian, C. L. Wan, Y. F. Wang, Q. S. Wei, T. Ishida, A. Yamamoto, A. Tsuruta, W. S. Shin, S. Li, K. Koumoto, *J. Mater. Chem. A*, 2017, **5**, 564-570.
205. J. Chen, X.-J. Wu, L. Yin, B. Li, X. Hong, Z. Fan, B. Chen, C. Xue, H. Zhang, *Angew. Chem. Int. Ed.*, 2015, **54**, 1210-1214.
206. Y. Yu, S.-Y. Huang, Y. Li, S. N. Steinmann, W. Yang, L. Cao, *Nano Lett.*, 2014, **14**, 553-558.
207. S. S. Chou, N. Sai, P. Lu, E. N. Coker, S. Liu, K. Artyushkova, T. S. Luk, B. Kaehr, C. J. Brinker, *Nat. Commun.*, 2015, **6**, 8311.
208. Q. Yun, Q. Lu, X. Zhang, C. Tan, H. Zhang, *Angew. Chem. Int. Ed.*, 2018, **57**, 626-646.
209. Z. X. Huang, Y. Wang, J. I. Wong, H. Y. Yang, *2D Mater.*, 2015, **2**, 024010.
210. W. F. Yang, J. W. Wang, C. H. Si, Z. Q. Peng, J. Frenzel, G. Eggeler, Z. H. Zhang, *J. Mater. Chem. A*, 2015, **3**, 17811-17819.
211. H. Liu, X. J. Chen, L. Deng, M. Ding, J. Q. Li, X. M. He, *J. Mater. Chem. A*, 2016, **4**, 17764-17772.
212. G. S. Bang, K. W. Nam, J. Y. Kim, J. Shin, J. W. Choi, S. Y. Choi, *ACS Appl. Mater. Interfaces*, 2014, **6**, 7084-7089.
213. X. X. Qian, S. D. Shen, T. Liu, L. Cheng, Z. Liu, *Nanoscale*, 2015, **7**, 6380-6387.
214. Y. Chen, C. Tan, H. Zhang, L. Wang, *Chem. Soc. Rev.*, 2015, **44**, 2681-2701.
215. Y. H. Huang, R. S. Chen, J. R. Zhang, Y. S. Huang, *Nanoscale*, 2015, **7**, 18964-18970.
216. W. S. Zheng, T. Xie, Y. Zhou, Y. L. Chen, W. Jiang, S. L. Zhao, J. X. Wu, Y. M. Jing, Y. Wu, G. C. Chen, Y. F. Guo, J. B. Yin, S. Y. Huang, H. Q. Xu, Z. F. Liu,

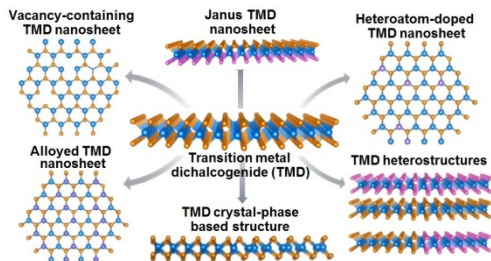
- H. L. Peng, *Nat. Commun.*, 2015, **6**, 6972.
217. G. Almeida, S. Dogan, G. Bertoni, C. Giannini, R. Gaspari, S. Perissinotto, R. Krahne, S. Ghosh, L. Manna, *J. Am. Chem. Soc.*, 2017, **139**, 3005-3011.
218. Y. B. Zhou, B. Deng, Y. Zhou, X. B. Ren, J. B. Yin, C. H. Jin, Z. F. Liu, H. L. Peng, *Nano Lett.*, 2016, **16**, 2103-2107.
219. B. J. Zheng, Y. F. Chen, Z. G. Wang, F. Qi, Z. S. Huang, X. Hao, P. J. Li, W. L. Zhang, Y. R. Li, *2D Mater.*, 2016, **3**, 035024.
220. D. B. Velusamy, R. H. Kim, S. Cha, J. Huh, R. Khazaeinezhad, S. H. Kassani, G. Song, S. M. Cho, S. H. Cho, I. Hwang, J. Lee, K. Oh, H. Choi, C. Park, *Nat. Commun.*, 2015, **6**, 8063.
221. K. Park, Y. Kim, J. G. Song, S. J. Kim, C. W. Lee, G. H. Ryu, Z. Lee, J. Park, H. Kim, *2D Mater.*, 2016, **3**, 014004.
222. B. L. Liu, Y. Q. Ma, A. Y. Zhang, L. Chen, A. N. Abbas, Y. H. Liu, C. F. Shen, H. C. Wan, C. W. Zhou, *ACS Nano*, 2016, **10**, 5153-5160.
223. Z. Y. Jia, S. L. Li, J. Y. Xiang, F. S. Wen, X. Bao, S. H. Feng, R. L. Yang, Z. Y. Liu, *Nanoscale*, 2017, **9**, 1916-1924.
224. M.-J. Lee, J.-H. Ahn, J. H. Sung, H. Heo, S. G. Jeon, W. Lee, J. Y. Song, K.-H. Hong, B. Choi, S.-H. Lee, M.-H. Jo, *Nat. Commun.*, 2016, **7**, 12011.
225. X. Chia, A. Y. S. Eng, A. Ambrosi, S. M. Tan, M. Pumera, *Chem. Rev.*, 2015, **115**, 11941-11966.
226. C. G. Morales-Guio, X. Hu, *Acc. Chem. Res.*, 2014, **47**, 2671-2681.
227. J. Xie, Y. Xie, *ChemCatChem*, 2015, **7**, 2568-2580.
228. M. Asadi, K. Kim, C. Liu, A. V. Addepalli, P. Abbasi, P. Yasaei, P. Phillips, A.

- Behranginia, J. M. Cerrato, R. Haasch, P. Zapol, B. Kumar, R. F. Klie, J. Abiade, L. A. Curtiss, A. Salehi-Khojin, *Science*, 2016, **353**, 467-470.
229. Q. Lu, Y. Yu, Q. Ma, B. Chen, H. Zhang, *Adv. Mater.*, 2016, **28**, 1917-1933.
230. J. Chen, X.-J. Wu, Y. Gong, Y. Zhu, Z. Yang, B. Li, Q. Lu, Y. Yu, S. Han, Z. Zhang, Y. Zong, Y. Han, L. Gu, H. Zhang, *J. Am. Chem. Soc.*, 2017, **139**, 8653-8660.
231. L. Yang, Q. Fu, W. H. Wang, J. Huang, J. L. Huang, J. Y. Zhang, B. Xiang, *Nanoscale*, 2015, **7**, 10490-10497.
232. Y. P. Huang, Y. E. Miao, J. Fu, S. Y. Mo, C. Wei, T. X. Liu, *J. Mater. Chem. A*, 2015, **3**, 16263-16271.
233. L. B. Ma, Y. Hu, G. Y. Zhu, R. P. Chen, T. Chen, H. L. Lu, Y. R. Wang, J. Liang, H. X. Liu, C. Z. Yan, Z. X. Tie, Z. Jin, J. Liu, *Chem. Mater.*, 2016, **28**, 5733-5742.
234. X. Y. Yu, M. S. Prevot, N. Guijarro, K. Sivula, *Nat. Commun.*, 2015, **6**, 7596.
235. P. S. Zhou, Q. Xu, H. X. Li, Y. Wang, B. Yan, Y. C. Zhou, J. F. Chen, J. N. Zhang, K. X. Wang, *Angew. Chem. Int. Ed.*, 2015, **54**, 15226-15230.
236. M. Q. Yang, Y. J. Xu, W. H. Lu, K. Y. Zeng, H. Zhu, Q. H. Xu, G. W. Ho, *Nat. Commun.*, 2017, **8**, 14224.
237. X. Hu, W. Shao, X. D. Hang, X. D. Zhang, W. G. Zhu, Y. Xie, *Angew. Chem. Int. Ed.*, 2016, **55**, 5733-5738.
238. X. M. Geng, Y. L. Zhang, Y. Han, J. X. Li, L. Yang, M. Benamara, L. Chen, H. L. Zhu, *Nano Lett.*, 2017, **17**, 1825-1832.
239. M. Liu, Z. J. Wang, J. X. Liu, G. J. Wei, J. Du, Y. P. Li, C. H. An, J. Zhang, *J.*

- Mater. Chem. A*, 2017, **5**, 1035-1042.
240. G. Babu, N. Masurkar, H. Al Salem, L. M. R. Arave, *J. Am. Chem. Soc.*, 2017, **139**, 171-178.
241. W. P. Sun, X. H. Rui, D. Yang, Z. Q. Sun, B. Li, W. Y. Zhang, Y. Zong, S. Madhavi, S. X. Dou, Q. Y. Yan, *ACS Nano*, 2015, **9**, 11371-11381.
242. H. Zhu, Z. Lai, Y. Fang, X. Zhen, C. Tan, X. Qi, D. Ding, P. Chen, H. Zhang, K. Pu, *Small*, 2017, **13**, 1604139
243. C. Tan, L. Zhao, P. Yu, Y. Huang, B. Chen, Z. Lai, X. Qi, M. H. Goh, X. Zhang, S. Han, X.-J. Wu, Z. Liu, Y. Zhao, H. Zhang, *Angew. Chem. Int. Ed.*, 2017, **56**, 7842-7846.
244. M. Acerce, E. K. Akdoğan, M. Chhowalla, *Nature*, 2017, **549**, 370-373.
245. C. Tan, Z. Zeng, X. Huang, X. Rui, X.-J. Wu, B. Li, Z. Luo, J. Chen, B. Chen, Q. Yan, H. Zhang, *Angew. Chem. Int. Ed.*, 2015, **54**, 1841-1845.
246. L. Qi, O. Fangping, Y. Zhixiong, P. Shenglin, Z. Wenzhe, Z. Hui, L. Mengqiu, P. Jiangling, *Nanotechnology*, 2017, **28**, 075702.
247. Y. Cai, Z. Bai, H. Pan, Y. P. Feng, B. I. Yakobson, Y.-W. Zhang, *Nanoscale*, 2014, **6**, 1691-1697.
248. Y. Nie, C. Liang, P.-R. Cha, L. Colombo, R. M. Wallace, K. Cho, *Sci. Rep.*, 2017, **7**, 2977.

## Table of Content

This review summarizes the recent advances on the preparation, characterization and application of new-structured ultrathin transition metal dichalcogenide (TMD) nanosheets.



## Biographies



Xiao Zhang received his BE and ME degrees in Harbin Engineering University (China) in 2010 and 2013, respectively. Then, he moved to the Interdisciplinary Graduate School of Nanyang Technological University in Singapore as a PhD student under the supervision of Prof. Hua Zhang in 2013. He completed his PhD at 2017 and currently is a research fellow in Prof. Hua Zhang's group. His research interest focuses on the synthesis and applications of novel two-dimensional nanomaterials.



Zhuangchai Lai received his BS degree in Material Chemistry from Sun Yat-sen University (China) in 2009. After he got his ME degree in the Industrial Catalysis from South China University of Technology (China) in 2012, he worked as a research assistant in Prof. Feng Peng's group. He moved to the School of Materials Science and Engineering in Nanyang Technological University in Singapore in 2014 to pursue his PhD degree under the supervision of Prof. Hua Zhang. His current research interests include the synthesis and applications of two-dimensional nanomaterials and their composites.



Qinglang Ma completed his B.S. degree (first-class honor) in Engineering (Materials Engineering) from Nanyang Technological University (Singapore) in 2013. Then, he received his Ph.D. degree from Interdisciplinary Graduated School at Nanyang Technological University under the supervision of Prof. Hua Zhang. He is currently a research fellow in Prof. Hua Zhang's group. His current research focuses on the synthesis and application of novel functional materials for environmental remediation.



Prof. Hua Zhang obtained his BS and MS degrees at Nanjing University in 1992 and 1995, respectively, and completed his PhD with Prof. Zhongfan Liu at Peking University in 1998. As a Postdoctoral Fellow, he joined Prof. Frans C. De Schryver's group at Katholieke Universiteit Leuven (Belgium) in 1999, and then moved to Prof. Chad A. Mirkin's group at Northwestern University in 2001. After he worked at NanoInk Inc. (USA) and Institute of Bioengineering and Nanotechnology (Singapore), he joined Nanyang Technological University in July 2006. His current research interests focus on the crystal phase engineering of nanomaterials and controlled epitaxial growth of heterostructures, including the synthesis of ultrathin two-dimensional nanomaterials (e.g. metal nanosheets, graphene, metal dichalcogenides, metal-organic frameworks, covalent organic frameworks, etc.), novel metallic and semiconducting nanomaterials and their

hybrid composites, for applications in catalysis, (opto-)electronic devices, nano- and biosensors, clean energy, and water remediation, *etc.*